A new look at local ultraluminous infrared galaxies

Efstathiou, A.; Farrah, D.; Afonso, J.; Clements, D. L.; González-Alfonso, E.; Lacy, M.; Oliver, S.; Papadopoulou Lesta, V.; Pearson, C.; Rigopoulou, D.

Published in:
Monthly Notices of the Royal Astronomical Society

DOI:
10.1093/mnras/stab3642

Publication date:
2022

Monthly Notices of the ROYAL ASTRONOMICAL SOCIETY

MNRAS **512,** 5183–5213 (2022) https://doi.org/10.1093/mnras/stab3642
Advance Access publication 2021 December 22

A new look at local ultraluminous infrared galaxies: the atlas and radiative transfer models of their complex physics

A. Efstathiou [1]★ D. Farrah,[2,3] J. Afonso [4,5] D. L. Clements [6] E. González-Alfonso,[7] M. Lacy,[8] S. Oliver,[9] V. Papadopoulou Lesta,[1] C. Pearson [10,11,12] D. Rigopoulou,[12] M. Rowan-Robinson,[6] H. W. W. Spoon,[13] A. Verma[12] and L. Wang[14,15]

[1]*School of Sciences, European University Cyprus, Diogenes Street, Engomi, 1516 Nicosia, Cyprus*
[2]*Department of Physics and Astronomy, University of Hawaii, 2505 Correa Road, Honolulu, HI 96822, USA*
[3]*Institute for Astronomy, University of Hawaii, 2680 Woodlawn Drive, Honolulu, HI 96822, USA*
[4]*Instituto de Astrofísica e Ciências do Espaco, Universidade de Lisboa, OAL, Tapada da Ajuda, P-1349-018 Lisboa, Portugal*
[5]*Departamento de Física, Faculdade de Ciências, Universidade de Lisboa, Edifício C8, Campo Grande, P-1749-016 Lisbon, Portugal*
[6]*Astrophysics Group, Imperial College London, Blackett Laboratory, Prince Consort Road, London SW7 2AZ, UK*
[7]*Departamento de Física y Matemáticas, Universidad de Alcalá, Campus Universitario, E-28871 Alcalá de Henares, Madrid, Spain*
[8]*National Radio Astronomy Observatory, 520 Edgemont Road, Charlottesville, VA 22903, USA*
[9]*Astronomy Centre, Department of Physics and Astronomy, University of Sussex, Falmer, Brighton BN1 9QH, UK*
[10]*RAL Space, CCLRC, Rutherford Appleton Laboratory, Chilton, Didcot, Oxfordshire OX11 0QX, UK*
[11]*School of Physical Sciences, The Open University, Milton Keynes MK7 6AA, UK*
[12]*Oxford Astrophysics, Denys Wilkinson Building, University of Oxford, Keble Road, Oxford OX1 3RH, UK*
[13]*Cornell Center for Astrophysics and Planetary Science, Ithaca, NY 14853, USA*
[14]*SRON Netherlands Institute for Space Research, Landleven 12, NL-9747 AD Groningen, the Netherlands*
[15]*Kapteyn Astronomical Institute, University of Groningen, Postbus 800, NL-9700 AV Groningen, the Netherlands*

Accepted 2021 November 29. Received 2021 November 29; in original form 2021 April 6

ABSTRACT

We present the ultraviolet to submillimetre spectral energy distributions (SEDs) of the HERschel Ultra Luminous Infrared Galaxy Survey (HERUS) sample of 42 local ultraluminous infrared galaxies (ULIRGs) and fit them with a Markov chain Monte Carlo code using the CYprus models for Galaxies and their NUclear Spectra (CYGNUS) radiative transfer models for starbursts, active galactic nucleus (AGN) tori, and host galaxy. The *Spitzer* IRS spectroscopy data are included in the fitting. Our Bayesian SED fitting method takes comparable time to popular energy balance methods but it is more physically motivated and versatile. All HERUS galaxies harbour high rates of star formation but we also find bolometrically significant AGN in all of the galaxies of the sample. We estimate the correction of the luminosities of the AGN in the ULIRGs due to the anisotropic emission of the torus and find that it could be up to a factor of ∼10 for nearly edge-on tori. We present a comparison of our results with the smooth torus model of Fritz et al. and the two-phase models of Siebenmorgen et al. and SKIRTOR. We find that the CYGNUS AGN torus models fit significantly better the SEDs of our sample compared to all other models. We find no evidence that strong AGN appear either at the beginning or end of a starburst episode or that starbursts and AGN affect each other. IRAS 01003−2238 and Mrk 1014 show evidence of dual AGNs in their SED fits, suggesting a minimum dual AGN fraction in the sample of 5 per cent.

Key words: radiative transfer – galaxies: active – galaxies: interactions – quasars: general – infrared: galaxies – submillimetre: galaxies.

1 INTRODUCTION

Local ultraluminous infrared galaxies (ULIRGs), with infrared luminosities exceeding 10^{12} $L_{\odot}$, are an important population in their own right as they are the most luminous galaxies in the local Universe. ULIRGs also allow us to study in detail the role of mergers in triggering extreme star formation and active galactic nucleus (AGN) activity that is deeply obscured by dust. They are therefore important laboratories for understanding these processes in order to aid the interpretation of observations of similar events that took place in the most luminous galaxies in the history of the Universe such as hyperluminous infrared galaxies (Rowan-Robinson et al. 1993; Rowan-Robinson 2000; Farrah et al. 2002; Verma et al. 2002; Efstathiou 2006), submillimetre galaxies (Barger et al. 1998; Hughes et al. 1998; Efstathiou & Rowan-Robinson 2003; Casey, Narayanan & Cooray 2014; Rowan-Robinson et al. 2018), quasars, and hot dust obscured galaxies (Eisenhardt et al. 2012; Bridge et al. 2013; Efstathiou et al. 2021; Farrah et al., in preparation). For these and other reasons, ULIRGs have received a lot of attention since their discovery by the *Infrared Astronomical Satellite* (*IRAS*) in the 1980s (Houck et al. 1985; Soifer et al. 1986). Excellent reviews of observational and theoretical work are given in Sanders & Mirabel (1996), Lonsdale, Farrah & Smith (2006a), and more recently Pérez-Torres et al. (2021).

★ E-mail: a.efstathiou@euc.ac.cy

Table 1. The sample, their basic data, and the log-likelihood (ML) of the best fit resulting from fitting the CYGNUS, FR06, S15 and SKIRTOR combinations of models. The sample selection criteria are given in Section 2.

ID	IRAS Name	Other Names	RA	Dec.	z	Opt. Class	Maximum likelihoods CYGNUS	F06	S15	SKIRTOR
1	00188−0856	–	5.360 507	− 8.657 217	0.128	LINER	− 459.7	− 467.7	− 519.9	− 567.3
2	00397−1312	–	10.564 704	− 12.934 122	0.262	H II	− 485.5	− 342.5	− 1093.6	− 848.9
3	01003−2238	–	15.708 365	− 22.365 895	0.118	H II	− 137.6	− 1227.6	− 125.7	− 1074.0
4	03158+4227	–	49.801 667	42.641 111	0.134	Sy2	− 262.8	− 702.0	− 291.9	− 973.9
5	03521+0028	–	58.675 800	0.617 611	0.152	LINER	− 196.5	− 373.3	− 199.8	− 402.8
6	05189−2524	–	80.255 800	− 25.362 600	0.043	Sy2	− 97.2	− 260.8	− 63.3	− 339.8
7	06035−7102	–	90.725 042	− 71.052 833	0.079	H II	− 126.9	− 158.4	− 223.1	− 188.2
8	06206−6315	–	95.255 042	− 63.289 861	0.092	Sy2	− 213.6	− 302.4	− 229.8	− 379.7
9	07598+6508	–	121.137 833	64.996 833	0.148	Sy1	− 33.9	− 26.5	− 181.4	− 33.4
10	08311−2459	–	128.335 833	− 25.159 361	0.100	Sy1	− 111.8	− 275.3	− 82.7	− 300.5
11	08572+3915	–	135.105 792	39.065 111	0.058	Sy2	− 218.6	− 618.5	− 1365.0	− 1353.1
12	09022−3615	–	136.052 961	− 36.450 274	0.060	H II	− 138.5	− 189.8	− 145.6	− 164.4
13	10378+1109	–	160.121 539	10.888 415	0.136	LINER	− 182.8	− 237.4	− 164.2	− 370.6
14	10565+2448	–	164.825 493	24.542 905	0.043	H II	− 322.9	− 512.7	− 363.5	− 493.1
15	11095−0238	–	168.014 071	− 2.906 219	0.107	LINER	− 187.1	− 773.2	− 547.7	− 983.2
16	12071−0444	–	182.438 049	− 5.020 490	0.128	Sy2	− 177.8	− 643.3	− 168.6	− 662.0
17	13120−5453	–	198.776 494	− 55.156 452	0.031	Sy2	− 349.0	− 503.4	− 343.4	− 508.9
18	13451+1232	4C 12.50	206.889 007	12.290 067	0.122	Sy2	− 107.3	− 524.5	− 87.6	− 671.4
19	14348−1447	–	219.410 000	− 15.005 556	0.083	LINER	− 119.7	− 233.0	− 153.6	− 299.9
20	14378−3651	–	220.245 867	− 37.075 538	0.068	Sy2	− 279.1	− 581.0	− 255.2	− 602.9
21	15250+3609	–	231.747 517	35.977 092	0.055	H II	− 370.5	− 854.7	− 595.7	− 1198.3
22	15462−0450	–	237.236 721	− 4.992 669	0.100	Sy1	− 174.7	− 104.4	− 54.6	− 193.5
23	16090−0139	–	242.918 469	− 1.785 156	0.134	LINER	− 185.5	− 284.5	− 230.7	− 290.2
24	17208−0014	–	260.841 481	− 0.283 594	0.043	H II	− 452.6	− 620.9	− 461.0	− 601.8
25	19254−7245	SuperAntena	292.839 167	− 72.655 000	0.062	Sy2	− 165.3	− 134.5	− 125.8	− 195.2
26	19297−0406	–	293.088 544	− 3.998 962	0.086	H II	− 179.3	− 265.9	− 186.9	− 340.0
27	20087−0308	–	302.849 458	− 2.997 417	0.106	LINER	− 333.2	− 343.5	− 386.3	− 352.2
28	20100−4156	–	303.373 083	− 41.793 028	0.130	H II	− 511.7	− 542.4	− 605.0	− 721.8
29	20414−1651	–	311.075 888	− 16.671 172	0.087	H II	− 199.7	− 367.5	− 195.0	− 292.7
30	20551−4250	ESO 286−19	314.611 589	− 42.650 056	0.043	H II	− 198.3	− 581.2	− 433.6	− 922.9
31	22491−1808	–	342.955 267	− 17.873 183	0.078	H II	− 188.8	− 534.9	− 208.1	− 607.2
32	23128−5919	ESO 148−2	348.944 790	− 59.054 320	0.045	H II	− 208.2	− 573.4	− 205.3	− 517.3
33	23230−6926	–	351.515 083	− 69.171 889	0.107	LINER	− 298.4	− 662.7	− 389.8	− 836.7
34	23253−5415	AM 2325−541	352.025 417	− 53.975 278	0.130	LINER	− 190.9	− 612.1	− 141.5	− 688.8
35	23365+3604	–	354.755 305	36.352 308	0.064	LINER	− 274.9	− 898.9	− 276.3	− 936.6
36	09320+6134	UGC 5101	143.964 981	61.353 182	0.039	LINER	− 475.7	− 548.2	− 520.2	− 558.4
37	12540+5708	Mrk 231	194.059 308	56.873 677	0.042	Sy1	− 49.7	− 67.8	− 46.8	− 186.7
38	13428+5608	Mrk 273	206.175 463	55.886 847	0.037	Sy2	− 218.0	− 288.8	− 262.2	− 411.6
39	13536+1836	Mrk 463	209.011 963	18.372 078	0.049	Sy2	− 141.2	− 150.0	− 161.1	− 122.4
40	15327+2340	Arp 220	233.738 563	23.503 139	0.018	Sy2	− 1099.8	− 1938.0	− 868.3	− 2143.5
41	16504+0228	NGC 6240	253.245 295	2.400 926	0.024	LINER	− 257.1	− 380.8	− 280.0	− 484.1
42	01572+0009	Mrk 1014	29.959 214	0.394 615	0.163	Sy1	− 483.5	− 425.6	− 96.3	− 536.9

The HERschel Ultra Luminous Infrared Galaxy Survey (HERUS) consisted of observations with the *Herschel Space Observatory* (Pilbratt et al. 2010) of the 42 most luminous ULIRGs in the local Universe in spectroscopy and photometry mode. Farrah et al. (2013) and Spoon et al. (2013) discussed the diagnostics provided by PACS spectroscopy and Pearson et al. (2016) discussed the corresponding diagnostics from SPIRE spectroscopy. Efstathiou et al. (2014) presented a detailed study of IRAS 08572+3915 that exhibits one of the deepest silicate absorption features observed in a galaxy. Clements et al. (2018) presented the SPIRE photometry of the HERUS galaxies.

As ULIRGs are deeply obscured by dust, radiative transfer models for both the starburst and AGN activity are needed for interpreting their spectral energy distributions (SEDs). Rowan-Robinson & Efstathiou (1993) presented the first such models for the local ULIRG population and fitted the SED of the prototypical ULIRG Arp 220. They showed that the SED of Arp 220 could be explained by a starburst model that was a factor of 4 more optically thick than the model for the starbursts in M 82 and NGC 1068 presented in the same paper. They also argued on the basis of fitting the *IRAS* colours that all ULIRGs in the *IRAS* Bright Galaxy sample (Sanders et al. 2003) required a similar higher optical depth starburst model to explain the far-infrared emission. Rigopoulou, Lawrence & Rowan-Robinson (1996) fitted the SEDs of the first ULIRGs to be detected in the submillimetre with the Rowan-Robinson & Efstathiou (1993) models and arrived at similar conclusions. Farrah et al. (2003) carried out for the first time starburst/AGN de-composition of the near- to far-infrared SEDs of a sample of 41 local ULIRGs using the starburst library of Efstathiou, Rowan-Robinson & Siebenmorgen (2000) and the AGN torus models of Efstathiou & Rowan-Robinson (1995). They concluded from this study that whereas most of the luminosity in local ULIRGs is due to starburst activity in about half of the sample there was significant emission from an AGN. Vega et al. (2008) fitted a sample of ULIRGs and luminous infrared galaxies (LIRGs; 10^{12} $L_{\odot}$

Table 2. Parameters of the models used in this paper, symbols used, their assumed ranges, and summary of other information about the models. The Fritz, Franceschini & Hatziminaoglou (2006) model assumes two additional parameters that define the density distribution in the radial direction (β) and azimuthal direction (γ). In this paper, we assume $\beta = 0$ and $\gamma = 4$. The SKIRTOR model (Stalevski et al. 2016) assumes two additional parameters that define the density distribution in the radial direction (p) and azimuthal direction (q). In this paper, we assume $p = 1$ and $q = 1$. In addition, the SKIRTOR library we used assumes that the fraction of mass inside clumps is 97 per cent. There are four additional scaling parameters for the starburst, spheroidal, AGN, and polar dust models, $f_{\rm SB}, f_{\rm s}, f_{\rm AGN}$, and $f_{\rm p}$, respectively.

Parameter	Symbol	Range	Comments
CYGNUS starburst			
Initial optical depth of GMCs	τ_V	50–250	Efstathiou et al. (2000), Efstathiou & Siebenmorgen (2009)
Starburst SFR e-folding time	τ_*	10–30 Myr	Incorporates Bruzual & Charlot (1993, 2003)
Starburst age	t_*	5–35 Myr	Metallicity = solar, Salpeter IMF
			Standard galactic dust mixture with PAHs
CYGNUS spheroidal host			
Spheroidal SFR e-folding time	τ^s	0.125–8 Gyr	Efstathiou & Rowan-Robinson (2003), Efstathiou et al. (2021)
Starlight intensity	ψ^s	1–17	Incorporates Bruzual & Charlot (1993, 2003)
Optical depth	τ_v^s	0.1–15	Metallicity = 40 per cent of solar, Salpeter IMF
			Standard galactic dust mixture with PAHs
CYGNUS AGN torus			
Torus equatorial UV optical depth	$\tau_{\rm uv}$	250–1450	Smooth tapered discs
Torus ratio of outer to inner radius	r_2/r_1	20–100	Efstathiou & Rowan-Robinson (1995), Efstathiou et al. (2013)
Torus half-opening angle	$\theta_{\rm o}$	30–75°	Standard galactic dust mixture without PAHs
Torus inclination	$\theta_{\rm i}$	0–90°	–
Fritz AGN torus			
Torus equatorial optical depth at 9.7 μm	–	0.1–10	Smooth flared discs
Torus ratio of outer to inner radius	–	10–150	FR06
Torus half-opening angle	–	20–70°	Standard galactic dust mixture without PAHs
Torus inclination	–	0–90°	–
SKIRTOR AGN torus			
Torus equatorial optical depth at 9.7 μm	–	3–11	Two-phase flared discs
Torus ratio of outer to inner radius	–	10–30	Stalevski et al. (2012, 2016)
Torus half-opening angle	–	20–70°	Standard galactic dust mixture without PAHs
Torus inclination	–	0–90°	–
Siebenmorgen15 AGN torus			
Cloud volume filling factor (per cent)		1.5–77.7	Two-phase anisotropic spheres
Optical depth of the individual clouds	–	0–45	Siebenmorgen, Heymann & Efstathiou (2015)
Optical depth of the disc mid-plane	–	0–1000	Fluffy dust mixture without PAHs
Inclination	–	0–90°	–

$> L_{\rm IR} > 10^{11}$ L$_\odot$) with the GRASIL models (Silva et al. 1998), reaching a similar conclusion. Efstathiou et al. (2014) de-composed the SED of the deep-silicate ULIRG IRAS 08572+3915, concluding that its emission is dominated by an obscured AGN with its torus viewed almost edge-on.

This is the first of two papers that present a new look at local ULIRGs that is based on detailed models of their SEDs from the ultraviolet to the submillimetre. In this paper (Paper A), we assemble the SEDs of the 42 local ULIRGs that constitute the HERUS sample and fit them with multicomponent radiative transfer models. In paper B (Farrah et al., in preparation), we present a detailed analysis of the results.

Our approach has three novel features compared to previous studies. The first novelty of this work is that we fit the ultraviolet to submillimetre SEDs of ULIRGs exclusively with radiative transfer models. The models constitute three libraries that describe the starburst, AGN, and host galaxy components. These three libraries are part of the collection of radiative transfer models named CYprus models for Galaxies and their NUclear Spectra (CYGNUS).[1] We have used extensively the starburst and AGN libraries for almost three decades to fit the SEDs of a broad range of galaxies (Rowan-Robinson & Efstathiou 1993; Rowan-Robinson et al. 1993, 1997; Efstathiou & Rowan-Robinson 1995; Hughes et al. 1998; Alexander et al. 1999; Rowan-Robinson 2000; Alonso-Herrero et al. 2001, 2003; Ruiz et al. 2001; Farrah et al. 2002, 2003, 2012; Verma et al. 2002; Efstathiou & Siebenmorgen 2005; Efstathiou 2006; Mattila et al. 2012, 2018; Efstathiou et al. 2013, 2021; Lonsdale et al. 2015; Herrero-Illana et al. 2017; Pitchford et al. 2019). To these two well-tested libraries, we added a third library of 'spheroidal' models that represent the host galaxy in which the starburst and AGN reside (Efstathiou et al. 2021). This library that is an evolution of the 'cirrus' models of Efstathiou & Rowan-Robinson (2003) self-consistently takes into account the absorption of starlight and reemission by interstellar dust in a spheroidal geometry. As we discuss below, our approach to use a library for the spheroidal component instead of running the model 'on the fly' during the fitting (e.g. as with GRASIL; see also discussion by Johnson et al. 2013) speeds up considerably the fitting.

The second novelty of our approach is that we feed the three libraries into the Markov chain Monte Carlo (MCMC) code SATMC (Johnson et al. 2013) to get the best fit. The output of SATMC is then

[1]The models are publicly available at https://arc.euc.ac.cy/cygnus/.

Table 3. Derived physical quantities and the symbol used in both papers A and B. The luminosities are integrated over 1–1000 μm except where indicated in the symbol that they are bolometric.

Physical quantity	Symbol
Observed AGN torus luminosity	$L^{\rm o}_{\rm AGN}$
Corrected AGN torus luminosity	$L^{\rm c}_{\rm AGN}$
Polar dust AGN luminosity	$L_{\rm p}$
Starburst luminosity	$L_{\rm Sb}$
Spheroidal host luminosity	$L_{\rm host}$
Total observed luminosity	$L^{\rm o}_{\rm Tot}$
Total corrected luminosity	$L^{\rm c}_{\rm Tot}$
Starburst SFR (averaged over 50 Myr)	$\dot{M}^{50}_{*}$
Starburst SFR (averaged over SB age)	$\dot{M}^{\rm age}_{*}$
Spheroidal SFR	$\dot{M}^{\rm Sph}_{*}$
Total SFR	$\dot{M}_{\rm tot}$
Starburst stellar mass	$M^{*}_{\rm sb}$
Spheroidal stellar mass	$M^{*}_{\rm sph}$
Total stellar mass	$M^{*}_{\rm tot}$
AGN fraction	$F_{\rm AGN}$
Anisotropy correction factor	A

post-processed by our own routines to get the luminosities of all components, star formation rates (SFRs) and stellar masses for the starburst and spheroid separately, AGN fraction, core-collapse supernova rate, and their errors. The fit of a single galaxy takes about 10–15 min. This is comparable to the time needed by popular energy balance methods such as MAGPHYS (da Cunha, Charlot & Elbaz 2008) and CIGALE (Noll et al. 2009; Boquien et al. 2019). The advantage of our method is that the model is more physically motivated and versatile as additional components (e.g. polar dust, a second AGN, or a second starburst) can very easily be added to the model. We give examples of this in the paper. We therefore foresee numerous applications of this method for the analysis of the rich data sets of ULIRGs and LIRGs at all redshifts that have been accumulated by multiwavelength surveys such as H-ATLAS (Eales et al. 2010) and HerMES (Oliver et al. 2012), projects such as the Herschel Extragalactic Legacy Project (Shirley et al. 2019, 2021), and projects that will be made possible in the near future with facilities such as ALMA, *JWST*, and *Euclid*.

The third novelty of the method used in this paper is that we include in the SED de-composition the *Spitzer* IRS spectroscopy at a resolution that is matched to the resolution of the radiative transfer models. Polycyclic Aromatic Hydrocarbon (PAH) features give an indication of star formation activity (Peeters et al. 2002), whereas silicate absorption features constrain the degree of obscuration in

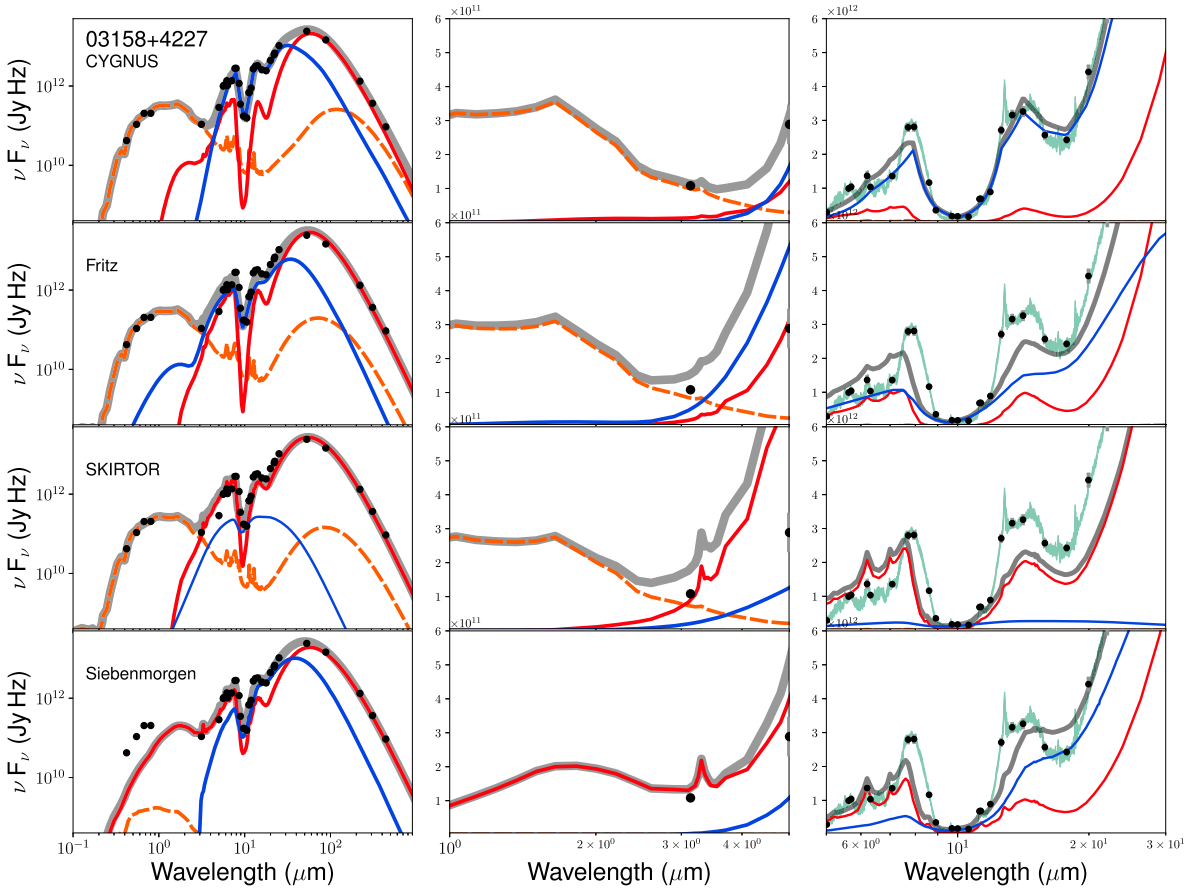

Figure 1. Comparison SED fit plots for IRAS 03158+4227. The top row shows fits with the CYGNUS combination of models: spheroidal host (orange), starburst (red), AGN torus (blue), and total (grey). The left-hand panel shows the fit over the 0.1–1000 μm range, the middle panel the near-infrared range, and the right-hand panel the 5–30 μm range. The second row shows fits with the CYGNUS AGN model replaced by the FR06 model, the third row replaces the CYGNUS AGN model with the SKIRTOR model, and the bottom row replaces the CYGNUS AGN model with the Siebenmorgen15 model. The full IRS data are plotted with green.

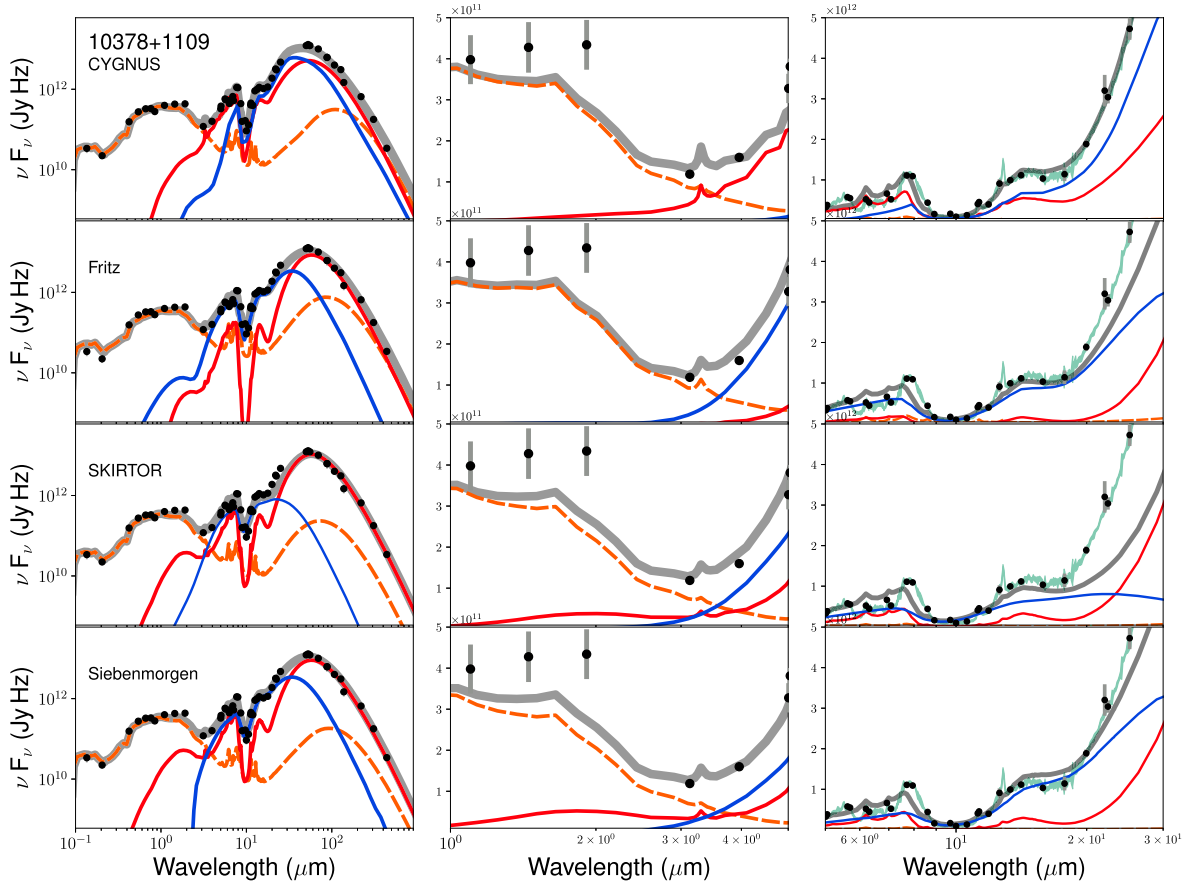

Figure 2. Comparison SED fit plots for IRAS 10378+1109. Other details are as in Fig. 1.

either the starburst or AGN torus (Spoon et al. 2007). According to most torus models, silicate emission and absorption also constrain the inclination of the torus that as we show in the paper is one of the main factors that determine the intrinsic luminosity of the AGN. Including the spectroscopy in the SED fitting is therefore particularly important for breaking the degeneracy in the fits and constraining the starburst, host, and AGN properties.

This paper is organized as follows: In Section 2, we describe the sample and in Section 3 the data we assembled. In Section 4, we describe the models and the SED de-composition method. In Section 5, we present our results with the CYGNUS models and compare results for six representative ULIRGs from four different torus models, CYGNUS, the models from Fritz et al. (2006), SKIRTOR (Stalevski et al. 2016), and Siebenmorgen et al. (2015). In Sections 6, 7, and 8, we discuss further our results and finally in Section 9 we present our conclusions.

Throughout this work, we assume $H_0 = 70\,\mathrm{km\,s^{-1}\,Mpc^{-1}}$, $\Omega = 1$, and $\Omega_\Lambda = 0.7$.

2 SAMPLE SELECTION

We start with the sample of ULIRGs observed by the HERUS carried out by the *Herschel Space Observatory*. This sample comprises all 40 ULIRGs from the *IRAS* PSC-z survey (Saunders et al. 2000) with 60 μm fluxes greater than 2 Jy, together with three randomly selected ULIRGs with lower 60 μm fluxes: IRAS 00397−1312 (1.8 Jy), IRAS 07598+6508 (1.7 Jy), and IRAS 13451+1232 (1.9 Jy). We then exclude 3C 273 as it is a blazar, to give a sample of 42 objects (Table 1). Strictly speaking, this sample is not complete, but it includes nearly all known ULIRGs at $z < 0.27$, and so should give an almost unbiased benchmark of local ULIRGs. All 42 objects were observed by the Infrared Spectrograph (IRS; Houck et al. 2004) onboard *Spitzer* and by *Herschel* as part of both HERUS and the SHINING survey (Fischer et al. 2010; Sturm et al. 2011; Hailey-Dunsheath et al. 2012; González-Alfonso et al. 2013).

3 DATA

To assemble the SEDs of the galaxies fitted in this paper, we combined data available from the literature and various archives. For all the HERUS galaxies, there are *Spitzer*/IRS data that we downloaded from CASSIS (Lebouteiller et al. 2011). We do not use the IRS data in their full resolution but we reduce their spectral resolution so that they are matched to the spectral resolution of the radiative transfer models. In particular, the IRS data included in the fit with SATMC have a wavelength grid that is separated in steps of 0.05 in the log of the rest wavelength. We also add additional points around the 9.7 μm silicate feature and the PAH features to the equally spaced wavelength grid. We find that with this approach we maintain the constraining power of the data but make the fitting of the multiwavelength SED feasible with current methods.

To extend the wavelength coverage of the SEDs from the ultraviolet to the submillimetre, we added to the IRS data the HERUS SPIRE photometry (Pearson et al. 2016; Clements et al. 2018) and *IRAS* data for all the galaxies and where available, GALEX, Pan-STARRS, 2MASS, *Spitzer*/IRAC, and SCUBA or other infrared and

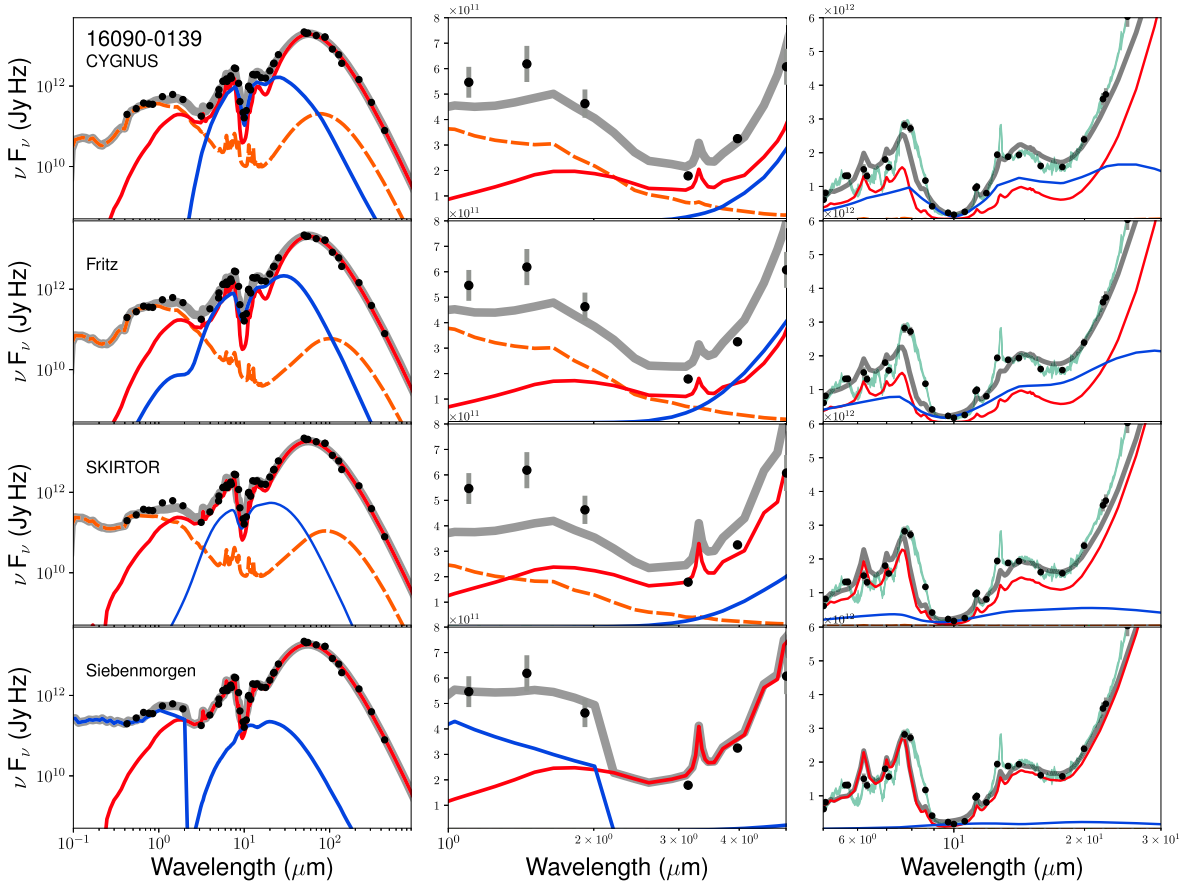

Figure 3. Comparison SED fit plots for IRAS 16090−0139. Other details are as in Fig. 1.

submillimetre data. Apart from the Pan-STARRS data (Flewelling et al. 2020), all of these data were extracted from the NASA Extragalactic Database (NED) or directly from the 2MASS archive. For IRAS 03158+4227, we used optical data from Sloan Digital Sky Survey (SDSS). Where available, we added to the SEDs the PACS continuum data from Farrah et al. (2013).

For seven of the ULIRGs that are included in the GOALS (Armus et al. 2009) sample (IRAS 05189−2524, IRAS 14348−1447, IRAS 15250+3608, IRAS 22491−1808, Arp 220, Mrk 231, Mrk 273, UGC 5101), we also added the optical photometry from U et al. (2012). For Arp 220, IRAS 08572+3915, and IRAS 10565+2448, we find that the optical photometry is more homogeneous if we use the SDSS data.

4 MODELLING

4.1 The CYGNUS models

The available photometry and spectroscopy have been fitted with the MCMC code SATMC (Johnson et al. 2013) using libraries of radiative transfer models for star formation, AGN activity, and host galaxy emission. These are part of the CYGNUS project. CYGNUS includes models for starbursts as described in Efstathiou et al. (2000) and Efstathiou & Siebenmorgen (2009). Models for massive star formation and starbursts were also presented and discussed in Rowan-Robinson & Crawford (1989), Rowan-Robinson & Efstathiou (1993), Efstathiou & Rowan-Robinson (1994), Krügel & Siebenmorgen (1994), Silva et al. (1998), Takagi, Arimoto & Hanami (2003), Dopita et al. (2005), and Siebenmorgen & Krügel (2007). The starburst model parameters and their assumed ranges are: the age of the starburst ($t_* = 5$–35 Myr), the giant molecular clouds' (GMCs') initial optical depth $\tau_V = 50$–250, and the time constant of the exponentially decaying SFR $\tau_* = 15$–35 Myr.

The method employed for computing the libraries of spheroidal host galaxy models of CYGNUS is an evolution of the 'cirrus' model of Efstathiou & Rowan-Robinson (2003) and is described in more detail in Efstathiou et al. (2021) and Efstathiou (in preparation). The models of Bruzual & Charlot (1993, 2003) are used in combination with an assumed star formation history (SFH) to compute the spectrum of starlight that is illuminating the dust throughout the model galaxy. The spectrum of starlight is assumed to be constant throughout the galaxy but its intensity varies throughout the galaxy according to a Sérsic profile with $n = 4$ that is equivalent to de Vaucouleurs's law. Efstathiou & Rowan-Robinson (2003) assumed an exponentially decaying SFH, whereas here we assume a delayed exponential ($\dot{M}_* \propto t \times \mathrm{e}^{-t/\tau^s}$), where τ^s is the e-folding time of the exponential.

The parameters assumed by the spheroidal model and their assumed ranges are: the e-folding time of the delayed exponential $\tau^s = 0.125$–8 Gyr, the optical depth of the spherical cloud from its centre to its surface $\tau_v^s = 0.1$–15, and $\psi^s = 1$–17 that controls the bolometric intensity of stellar emission relative to that of the bolometric intensity of starlight in the solar neighbourhood. The library used in this paper was computed assuming all the galaxies have an age equal to the age of the Universe at a redshift of $z = 0.1$. We assumed that all the stars in the galaxy formed with a Salpeter

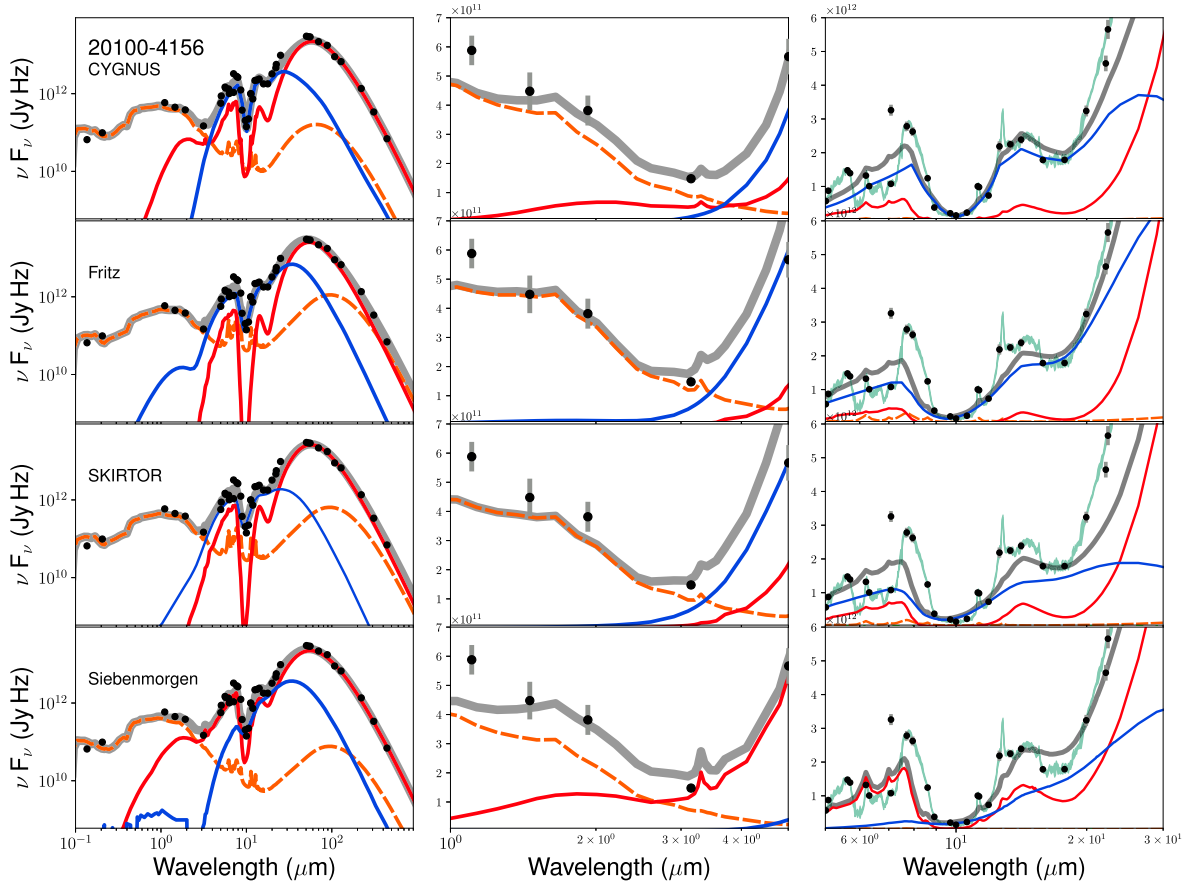

Figure 4. Comparison SED fit plots for IRAS 20100−4156. Other details are as in Fig. 1.

initial mass function (IMF) out of gas with a metallicity of 40 per cent of solar.

There exist a wide variety of AGN obscurer models in the literature with different assumptions about the obscurer geometry (Pier & Krolik 1993; Rowan-Robinson et al. 1993; Granato & Danese 1994; Efstathiou & Rowan-Robinson 1995; Nenkova et al. 2002; Dullemond & van Bemmel 2005; Fritz et al. 2006; Hönig et al. 2006; Nenkova et al. 2008; Schartmann et al. 2008; Heymann & Siebenmorgen 2012; Stalevski et al. 2012, 2016; Efstathiou et al. 2013; Siebenmorgen et al. 2015; Hönig & Kishimoto 2017). We therefore explored the impact of four different AGN models:

(i) The CYGNUS AGN torus model. More details of the implementation of this combination of models within SATMC are given in Efstathiou et al. (2021). A number of results with this combination of models in the MCMC code SATMC have previously been presented (Herrero-Illana et al. 2017; Kool et al. 2018; Mattila et al. 2018; Pitchford et al. 2019; Efstathiou et al. 2021; Kankare et al. 2021).

(ii) The AGN torus model of Fritz et al. (2006), hereafter FR06.

(iii) The two-phase AGN torus model SKIRTOR of Stalevski et al. (2016).

(iv) The two-phase AGN torus model of Siebenmorgen et al. (2015).

The CYGNUS AGN model parameters and their assumed ranges are the half-opening angle of the torus ($\theta_o = 30°$–$75°$), the inclination of the torus ($\theta_i = 0°$–$90°$), the ratio of outer to inner disc radius ($r_2/r_1 = 20$–100), and the equatorial optical depth at 1000 Å [$\tau_{uv} = 250$–1450; for the dust model used in Efstathiou & Rowan-Robinson (1995), this translates to an $A_V \approx \tau_{uv}/5$ and $\tau_{9.7\,\mu m} \approx \tau_{uv}/61$]. All the models assume that the density distribution in the tapered disc falls off with distance from the supermassive black hole r as r^{-1}. In addition, we explore for some objects the impact of adding a component of polar dust in the fits. This is discussed further in Section 5.5.

For the CYGNUS combination, we therefore have a total of 14 free parameters in the fits: τ^s, τ^s_v, ψ^s, θ_o, θ_i, r_2/r_1, τ_{uv}, t_*, τ_V, τ_*, f_{SB}, f_{AGN}, f_s, and f_p. The last four are scaling factors that determine the luminosities of the starburst, AGN, and spheroidal and polar dust components, respectively. The parameters of all models used in this work are also listed in Table 2 together with a summary of other useful information.

4.2 The Fritz et al. and SKIRTOR AGN torus models

The FR06 model assumes a smooth torus as in Efstathiou & Rowan-Robinson (1995). The models are available in a public library.[2] The FR06 model has two more parameters than the CYGNUS model. We use the subset of the library that results by fixing the two parameters that determine the density distribution within the torus in the radial direction ($\beta = 0$) and polar direction ($\gamma = 4$). This gives the same number of free parameters as the CYGNUS AGN torus model. The four parameters are the equatorial optical depth at 9.7 μm, the ratio of outer to inner radius, the half-opening angle of the torus, and the inclination plus the scaling factor. For these parameters, we use the

[2]https://www.irya.unam.mx/gente/j.fritz/JFhp/AGN_models.html

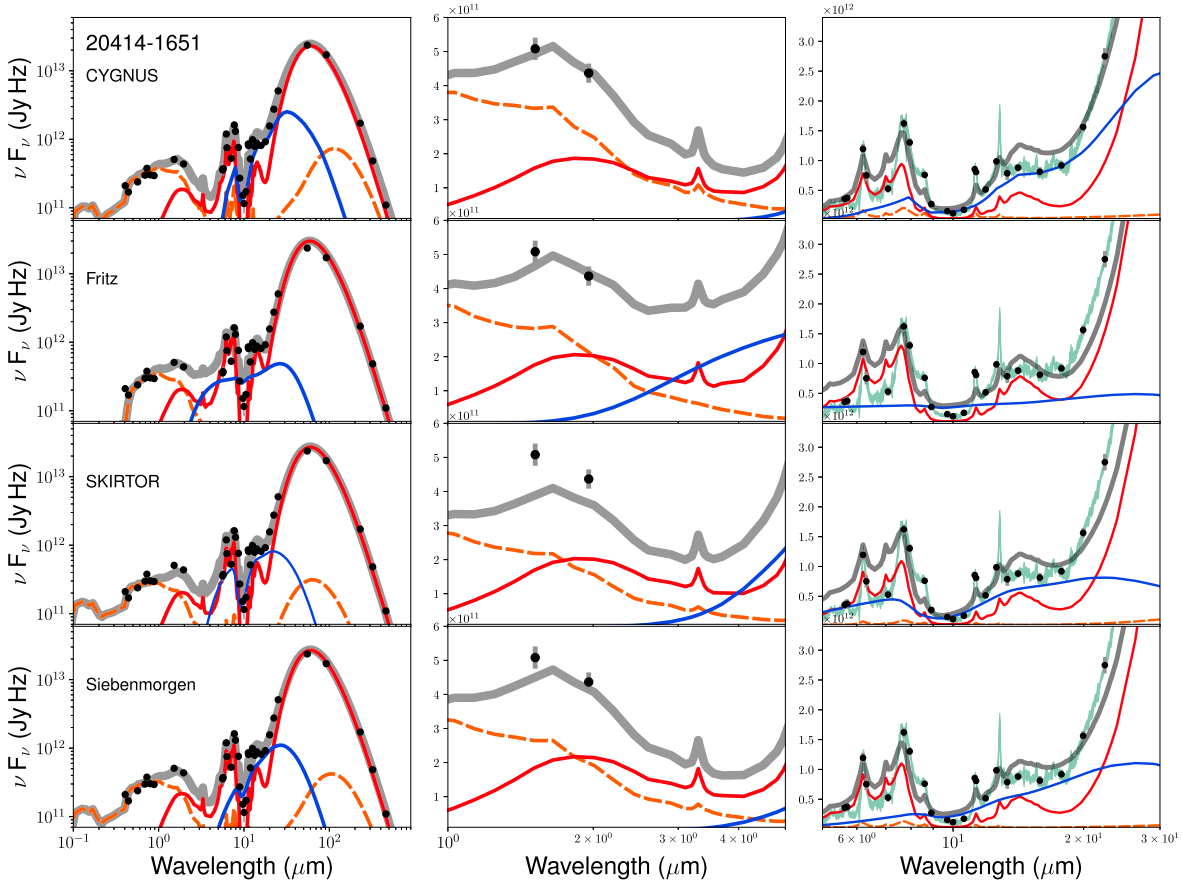

Figure 5. Comparison SED fit plots for IRAS 20414−1651. Other details are as in Fig. 1.

full range available in the library. For the FR06 combination, we also have a total of 14 free parameters in the fits. It is important to note that the FR06 models have a lower resolution in inclination compared to the CYGNUS model, with 10 angles covering the range of 0–90 deg. We linearly interpolate the models between these values to obtain the same resolution we have in CYGNUS.

The SKIRTOR model assumes a two-phase geometry; i.e. it assumes that the torus dust lies in discrete clouds that are embedded in a smooth distribution. The SKIRTOR models are also available in a public library.[3] As in the case of the FR06 models, we selected the subset of the library by fixing the parameters that describe the density distribution in the torus in the radial direction ($p = 1$) and polar direction ($q = 1$). The parameter p takes four discrete values in the library (0, 0.5, 1, and 1.5). As we discuss later in the paper, the main problem with these models is that they do not produce deep enough silicate absorption features to fit the SEDs of the ULIRGs in this sample. Assuming a value for $p < 1$ leads to AGN torus spectra with shallower silicate absorption features and therefore worse fits with these models. We have four remaining free parameters in the SKIRTOR model that are the same as those in the FR06 model. For these parameters, we also use the full range available in the library. For the SKIRTOR combination, we also have a total of 14 free parameters in the fits. The SKIRTOR models also have 10 inclinations that cover the range of 0–90°, so again we linearly interpolate the templates to have the same resolution as in the CYGNUS fits.

4.3 The Siebenmorgen et al. models

As in the case of the SKIRTOR models, the Siebenmorgen et al. (2015) models also assume a two-phase geometry and they are computed with a Monte Carlo radiative transfer code. The models are available in a public library.[4] A particular feature of the Siebenmorgen models is that the opening angle of the torus is not a parameter of the model. This model is in that respect similar to the smooth 'anisotropic sphere' model of Efstathiou & Rowan-Robinson (1995) that was used to fit the SED of IRASF 10214+4724 (Rowan-Robinson et al. 1993). Another feature of the model is that it assumes that the dust grains are fluffy and have higher emissivity in the far-infrared and submillimetre compared to normal interstellar grains. The model assumes the following parameters: the cloud volume filling factor, the optical depth (in the V band) of the individual clouds, the optical depth (in the V band) of the disc mid-plane, and the inclination that takes 9 values corresponding to bins at 86, 80, 73, 67, 60, 52, 43, 33, and 19 deg measured from the pole. As in the case of the SKIRTOR and Fritz models, we interpolate the models to have the same resolution in inclination as the CYGNUS model. The model also has as a parameter the inner radius of the dusty torus. We select the value of 1000×10^{15} cm that for an AGN luminosity of

[3] https://sites.google.com/site/skirtorus/

[4] http://www.eso.org/~rsiebenm/agn_models/index.html

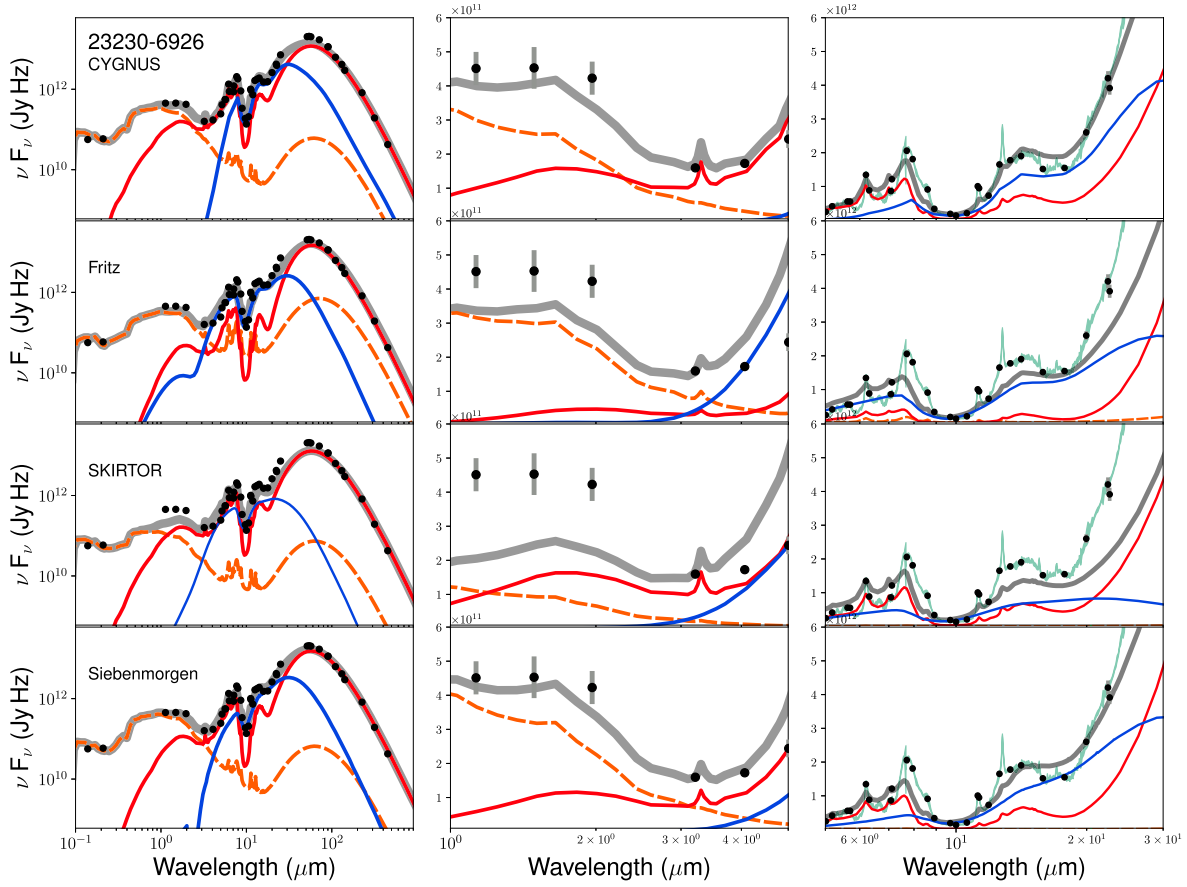

Figure 6. Comparison SED fit plots for IRAS 23230−6926. Other details are as in Fig. 1.

10^{11} $L_\odot$ gives a temperature at the inner torus radius of about 1000 K. Our fits with the Siebenmorgen models also have a total of 14 free parameters.

5 RESULTS

A description of all the derived physical quantities discussed in this paper is given in Table 3. The infrared luminosities and derived parameters and physical quantities from the SED fits are presented in Tables 4 and 5. We also give additional derived physical quantities in Tables B1, B2, B3, and B4. To give an impression of the results, we selected six representative objects from the sample, IRAS 03158+4227, IRAS 10378+1109, IRAS 16090−0139, IRAS 20100−4156, IRAS 20414−1651, and IRAS 23230−6926. We plot the SEDs of these six galaxies in Figs 1–6. The full suite of SED fits with the CYGNUS models is presented in Figs A1–A7.

It is clear from the SED fits shown in Figs 1–6, and also from the log-likelihood values listed in Table 1, that the CYGNUS combination of models provides good fits to the data including the IRS spectroscopy. The fits with the combination that includes the SKIRTOR and Fritz models are usually worse especially in the range covered by the IRS data. The SKIRTOR models generally do not produce deep enough silicate absorption features to fit the mid-infrared spectroscopy. The Siebenmorgen15 models give better fits than SKIRTOR and Fritz but usually worse than CYGNUS.

An important feature of the results from the SED fitting is that due to the anisotropy of the emission from the AGN torus, which is usually optically thick to its own radiation (Pier & Krolik 1993; Efstathiou & Rowan-Robinson 1995; Efstathiou et al. 2014), the AGN luminosity needs to be corrected by the anisotropy correction factor $A(\theta_i)$ defined in Efstathiou (2006),

$$A(\theta_i) = \frac{\int_0^{\pi/2} S(\theta_i')\ \sin\ \theta_i'\ \mathrm{d}\theta_i'}{S(\theta_i)}, \quad (1)$$

where $S(\theta_i)$ is the bolometric emission over the relevant wavelength range. $A(\theta_i)$ is generally different for the infrared and bolometric luminosities and is necessary and significant for all the AGN torus models considered in this paper. In Table 4, we give both the 'observed' or uncorrected AGN luminosities and their 'corrected' counterparts.

5.1 Star formation

In this work, we discuss two estimates of the SFR of the starburst episodes in the ULIRGs: the SFR averaged over the age of the starburst as determined from the fits $\dot{M}_{\rm Sb}^{\rm age}$ and the SFR averaged over a flat time-scale of 50 Myr $\dot{M}_{\rm Sb}^{50}$. We find that all objects harbour high rates of star formation, between 22 and 644 $M_\odot$ yr^{-1} when the SFR is averaged over 50 Myr and between 59 and 2203 $M_\odot$ yr^{-1} when averaged over the age of the starburst. The starburst component always dominates the total SFR. Host SFRs are in most cases at least an order of magnitude lower.

We plot SFR against $L_{\rm Sb}$ and $L_{\rm Tot}^{\rm o}$ in Fig. 7. There is a strong correlation between $L_{\rm Sb}$ and $\dot{M}_{\rm Sb}^{\rm age}$ (Kendall's $\tau = 0.88$), of which an

Table 4. The AGN, starburst, spheroidal, and total infrared luminosities (integrated over 1–1000 μm), derived from the CYGNUS model fits. For the AGN and total luminosities, both the observed and anisotropy corrected luminosities are given, as well as the anisotropy factor $A(\theta_i)$ (see equation 1) used to perform the correction. The equivalent bolometric luminosities are given in Table B1. The equivalent luminosities from the FR06, SKIRTOR, and Siebenmorgen15 model fits are given in Tables B2, B3, and B4.

ID	L^{o}_{AGN}	L^{c}_{AGN}	L_{Sb}	L_{host}	L^{o}_{Tot}	L^{c}_{Tot}	$A(\theta_i)$
	10^{12} L$_\odot$			10^{11} L$_\odot$	10^{12} L$_\odot$		
1	$0.28^{+0.03}_{-0.05}$	$0.83^{+0.14}_{-0.18}$	$1.86^{+0.03}_{-0.02}$	$1.06^{+0.12}_{-0.23}$	$2.25^{+0.04}_{-0.05}$	$2.80^{+0.14}_{-0.18}$	$2.95^{+0.17}_{-0.27}$
2	$2.10^{+0.55}_{-0.31}$	$15.62^{+7.27}_{-3.51}$	$7.14^{+0.18}_{-0.35}$	$1.55^{+0.49}_{-0.49}$	$9.40^{+0.34}_{-0.24}$	$22.91^{+6.95}_{-3.37}$	$7.43^{+1.41}_{-0.95}$
3	$0.81^{+0.22}_{-0.09}$	$1.47^{+0.17}_{-0.21}$	$0.77^{+0.02}_{-0.12}$	$0.23^{+0.05}_{-0.03}$	$1.60^{+0.12}_{-0.08}$	$2.26^{+0.12}_{-0.22}$	$1.81^{+0.03}_{-0.27}$
4	$1.39^{+0.18}_{-0.23}$	$6.07^{+0.81}_{-1.27}$	$2.63^{+0.10}_{-0.06}$	$0.78^{+0.09}_{-0.10}$	$4.09^{+0.13}_{-0.15}$	$8.78^{+0.75}_{-1.17}$	$4.38^{+0.15}_{-0.27}$
5	$0.26^{+0.04}_{-0.03}$	$0.95^{+0.20}_{-0.19}$	$2.16^{+0.03}_{-0.02}$	$0.11^{+0.02}_{-0.01}$	$2.42^{+0.03}_{-0.03}$	$3.12^{+0.18}_{-0.18}$	$3.70^{+0.52}_{-0.69}$
6	$0.55^{+0.08}_{-0.06}$	$2.49^{+0.32}_{-0.30}$	$0.77^{+0.07}_{-0.08}$	$0.68^{+0.32}_{-0.20}$	$1.39^{+0.07}_{-0.05}$	$3.33^{+0.29}_{-0.25}$	$4.52^{+0.03}_{-0.27}$
7	$0.21^{+0.09}_{-0.03}$	$0.38^{+0.86}_{-0.07}$	$1.21^{+0.03}_{-0.09}$	$1.82^{+0.16}_{-1.16}$	$1.60^{+0.03}_{-0.11}$	$1.78^{+0.71}_{-0.08}$	$1.82^{+2.40}_{-0.11}$
8	$0.17^{+0.02}_{-0.02}$	$0.41^{+0.09}_{-0.06}$	$1.18^{+0.01}_{-0.03}$	$1.19^{+0.28}_{-0.12}$	$1.47^{+0.02}_{-0.03}$	$1.71^{+0.08}_{-0.07}$	$2.38^{+0.24}_{-0.15}$
9	$1.98^{+0.17}_{-0.19}$	$1.17^{+0.10}_{-0.12}$	$2.18^{+0.01}_{-0.05}$	$0.04^{+0.03}_{-0.01}$	$4.16^{+0.16}_{-0.19}$	$3.35^{+0.09}_{-0.13}$	$0.59^{+0.00}_{-0.01}$
10	$0.56^{+0.07}_{-0.08}$	$1.61^{+0.20}_{-0.21}$	$2.26^{+0.03}_{-0.05}$	$1.06^{+0.17}_{-0.09}$	$2.93^{+0.05}_{-0.08}$	$3.97^{+0.18}_{-0.19}$	$2.86^{+0.08}_{-0.02}$
11	$0.78^{+0.15}_{-0.11}$	$8.77^{+3.02}_{-1.36}$	$0.66^{+0.05}_{-0.09}$	$0.19^{+0.09}_{-0.02}$	$1.47^{+0.08}_{-0.05}$	$9.45^{+2.95}_{-1.30}$	$11.19^{+2.57}_{-1.07}$
12	$0.26^{+0.03}_{-0.02}$	$1.43^{+0.29}_{-0.19}$	$1.41^{+0.01}_{-0.02}$	$0.36^{+0.06}_{-0.05}$	$1.71^{+0.02}_{-0.02}$	$2.88^{+0.28}_{-0.19}$	$5.57^{+0.53}_{-0.26}$
13	$0.83^{+0.12}_{-0.14}$	$10.72^{+5.02}_{-3.46}$	$0.81^{+0.12}_{-0.13}$	$0.90^{+0.43}_{-0.35}$	$1.73^{+0.04}_{-0.06}$	$11.63^{+4.93}_{-3.37}$	$12.91^{+4.01}_{-3.04}$
14	$0.09^{+0.02}_{-0.01}$	$0.17^{+0.03}_{-0.01}$	$0.93^{+0.02}_{-0.01}$	$0.93^{+0.12}_{-0.13}$	$1.11^{+0.02}_{-0.00}$	$1.19^{+0.04}_{-0.01}$	$1.86^{+0.15}_{-0.06}$
15	$0.94^{+0.12}_{-0.10}$	$12.66^{+4.71}_{-2.44}$	$0.59^{+0.08}_{-0.10}$	$0.19^{+0.04}_{-0.02}$	$1.55^{+0.03}_{-0.04}$	$13.27^{+4.62}_{-2.36}$	$13.41^{+3.52}_{-1.52}$
16	$0.84^{+0.18}_{-0.10}$	$2.59^{+1.08}_{-0.28}$	$1.19^{+0.06}_{-0.17}$	$1.61^{+0.47}_{-0.35}$	$2.20^{+0.06}_{-0.09}$	$3.94^{+0.92}_{-0.25}$	$3.07^{+0.78}_{-0.21}$
17	$0.10^{+0.02}_{-0.01}$	$0.22^{+0.12}_{-0.04}$	$1.52^{+0.02}_{-0.02}$	$1.39^{+0.18}_{-0.27}$	$1.76^{+0.01}_{-0.02}$	$1.88^{+0.11}_{-0.04}$	$2.23^{+0.68}_{-0.15}$
18	$1.33^{+0.25}_{-0.22}$	$8.39^{+1.47}_{-1.42}$	$0.35^{+0.10}_{-0.12}$	$2.39^{+0.60}_{-0.56}$	$1.92^{+0.19}_{-0.17}$	$8.98^{+1.41}_{-1.36}$	$6.30^{+0.33}_{-0.15}$
19	$0.39^{+0.04}_{-0.14}$	$2.59^{+0.25}_{-1.21}$	$1.33^{+0.12}_{-0.01}$	$2.68^{+0.11}_{-0.67}$	$1.99^{+0.02}_{-0.09}$	$4.19^{+0.23}_{-1.16}$	$6.61^{+0.02}_{-1.17}$
20	$0.14^{+0.01}_{-0.01}$	$0.53^{+0.08}_{-0.07}$	$0.95^{+0.01}_{-0.01}$	$0.43^{+0.13}_{-0.11}$	$1.13^{+0.01}_{-0.01}$	$1.52^{+0.08}_{-0.07}$	$3.73^{+0.27}_{-0.30}$
21	$0.37^{+0.04}_{-0.05}$	$2.59^{+0.46}_{-0.42}$	$0.66^{+0.03}_{-0.02}$	$0.25^{+0.02}_{-0.03}$	$1.06^{+0.03}_{-0.03}$	$3.28^{+0.45}_{-0.40}$	$6.98^{+0.62}_{-0.39}$
22	$0.25^{+0.05}_{-0.04}$	$0.22^{+0.04}_{-0.03}$	$0.96^{+0.09}_{-0.04}$	$0.41^{+0.73}_{-0.14}$	$1.26^{+0.13}_{-0.06}$	$1.22^{+0.12}_{-0.06}$	$0.88^{+0.05}_{-0.03}$
23	$0.26^{+0.07}_{-0.05}$	$0.68^{+0.24}_{-0.13}$	$2.69^{+0.09}_{-0.11}$	$0.64^{+0.24}_{-0.15}$	$3.02^{+0.06}_{-0.07}$	$3.44^{+0.16}_{-0.10}$	$2.58^{+0.25}_{-0.16}$
24	$0.06^{+0.02}_{-0.01}$	$0.13^{+0.07}_{-0.02}$	$2.10^{+0.01}_{-0.02}$	$0.67^{+0.31}_{-0.11}$	$2.22^{+0.03}_{-0.01}$	$2.29^{+0.07}_{-0.03}$	$2.15^{+0.41}_{-0.06}$
25	$0.28^{+0.20}_{-0.04}$	$1.00^{+0.50}_{-0.15}$	$0.71^{+0.04}_{-0.14}$	$3.24^{+0.83}_{-0.56}$	$1.32^{+0.14}_{-0.04}$	$2.04^{+0.43}_{-0.15}$	$3.61^{+0.06}_{-0.62}$
26	$0.34^{+0.17}_{-0.05}$	$2.31^{+5.11}_{-0.53}$	$1.96^{+0.07}_{-0.13}$	$1.96^{+0.74}_{-0.51}$	$2.50^{+0.08}_{-0.04}$	$4.47^{+4.98}_{-0.51}$	$6.78^{+8.54}_{-1.48}$
27	$0.10^{+0.03}_{-0.03}$	$0.25^{+0.13}_{-0.10}$	$2.52^{+0.07}_{-0.02}$	$0.97^{+0.25}_{-0.68}$	$2.71^{+0.07}_{-0.05}$	$2.86^{+0.11}_{-0.10}$	$2.55^{+0.68}_{-0.58}$
28	$0.52^{+0.08}_{-0.10}$	$1.82^{+0.37}_{-0.57}$	$2.62^{+0.06}_{-0.09}$	$0.60^{+0.26}_{-0.11}$	$3.20^{+0.09}_{-0.13}$	$4.50^{+0.39}_{-0.59}$	$3.52^{+0.35}_{-0.53}$
29	$0.15^{+0.03}_{-0.04}$	$0.88^{+0.21}_{-0.41}$	$1.25^{+0.02}_{-0.02}$	$0.65^{+0.37}_{-0.15}$	$1.46^{+0.03}_{-0.03}$	$2.20^{+0.21}_{-0.39}$	$6.03^{+1.38}_{-1.72}$
30	$0.31^{+0.06}_{-0.03}$	$1.20^{+0.27}_{-0.13}$	$0.62^{+0.02}_{-0.03}$	$0.85^{+0.24}_{-0.25}$	$1.02^{+0.05}_{-0.03}$	$1.91^{+0.26}_{-0.13}$	$3.86^{+0.15}_{-0.07}$
31	$0.36^{+0.03}_{-0.06}$	$3.34^{+0.62}_{-0.76}$	$0.73^{+0.04}_{-0.02}$	$0.81^{+0.17}_{-0.24}$	$1.17^{+0.02}_{-0.03}$	$4.16^{+0.61}_{-0.75}$	$9.42^{+2.13}_{-2.03}$
32	$0.13^{+0.01}_{-0.02}$	$0.29^{+0.03}_{-0.05}$	$0.56^{+0.01}_{-0.01}$	$0.44^{+0.06}_{-0.09}$	$0.74^{+0.02}_{-0.03}$	$0.89^{+0.03}_{-0.05}$	$2.19^{+0.08}_{-0.13}$
33	$0.34^{+0.05}_{-0.04}$	$1.25^{+0.30}_{-0.12}$	$1.08^{+0.01}_{-0.03}$	$0.23^{+0.05}_{-0.04}$	$1.44^{+0.03}_{-0.04}$	$2.35^{+0.28}_{-0.12}$	$3.72^{+0.42}_{-0.01}$
34	$0.57^{+0.12}_{-0.17}$	$4.08^{+1.76}_{-1.94}$	$1.12^{+0.14}_{-0.08}$	$3.43^{+0.74}_{-0.86}$	$2.04^{+0.10}_{-0.11}$	$5.54^{+1.74}_{-1.88}$	$7.11^{+1.80}_{-1.88}$
35	$0.26^{+0.07}_{-0.03}$	$1.17^{+0.73}_{-0.28}$	$1.14^{+0.01}_{-0.04}$	$0.38^{+0.05}_{-0.03}$	$1.44^{+0.04}_{-0.03}$	$2.35^{+0.70}_{-0.27}$	$4.42^{+1.50}_{-0.65}$
36	$0.09^{+0.02}_{-0.01}$	$0.24^{+0.07}_{-0.05}$	$0.85^{+0.03}_{-0.01}$	$0.94^{+0.13}_{-0.09}$	$1.03^{+0.03}_{-0.01}$	$1.18^{+0.08}_{-0.05}$	$2.68^{+0.51}_{-0.47}$
37	$1.46^{+0.17}_{-0.13}$	$3.49^{+0.46}_{-0.35}$	$1.89^{+0.14}_{-0.12}$	$1.04^{+0.14}_{-0.10}$	$3.46^{+0.21}_{-0.14}$	$5.48^{+0.46}_{-0.29}$	$2.38^{+0.08}_{-0.07}$
38	$0.17^{+0.04}_{-0.03}$	$0.56^{+0.36}_{-0.19}$	$1.09^{+0.03}_{-0.02}$	$0.36^{+0.12}_{-0.04}$	$1.30^{+0.04}_{-0.03}$	$1.69^{+0.37}_{-0.19}$	$3.23^{+1.11}_{-0.71}$
39	$0.50^{+0.06}_{-0.04}$	$0.41^{+0.07}_{-0.03}$	$0.23^{+0.02}_{-0.02}$	$0.39^{+0.10}_{-0.14}$	$0.76^{+0.06}_{-0.05}$	$0.68^{+0.07}_{-0.04}$	$0.82^{+0.05}_{-0.02}$
40	$0.12^{+0.08}_{-0.01}$	$0.68^{+0.89}_{-0.09}$	$0.90^{+0.01}_{-0.03}$	$0.62^{+0.13}_{-0.04}$	$1.08^{+0.07}_{-0.01}$	$1.64^{+0.88}_{-0.09}$	$5.85^{+2.32}_{-0.43}$
41	$0.12^{+0.02}_{-0.03}$	$0.36^{+0.04}_{-0.13}$	$0.42^{+0.04}_{-0.03}$	$1.39^{+0.44}_{-0.56}$	$0.68^{+0.03}_{-0.03}$	$0.91^{+0.05}_{-0.14}$	$2.90^{+0.01}_{-0.61}$
42	$0.80^{+0.11}_{-0.09}$	$0.42^{+0.07}_{-0.06}$	$2.44^{+0.08}_{-0.05}$	$1.85^{+0.36}_{-0.59}$	$3.42^{+0.11}_{-0.09}$	$3.04^{+0.07}_{-0.06}$	$0.53^{+0.03}_{-0.03}$

acceptable linear parametrization is

$$\frac{\dot{M}^{age}_{Sb}}{M_\odot\,yr^{-1}} = (3.14 \pm 0.08) \times 10^{-10} \frac{L_{Sb}}{L_\odot} - 5 \pm 16 \quad (2)$$

or

$$\frac{\dot{M}^{age}_{Sb}}{M_\odot\,yr^{-1}} = (3.11 \pm 0.05) \times 10^{-10} \frac{L_{Sb}}{L_\odot} \quad (3)$$

Table 5. Fitted parameters and derived physical properties from the CYGNUS models. θ_o is the half-opening angle of the torus, θ_i is the inclination of the torus, r_2/r_1 is the ratio of outer to inner disc radius, and τ_{uv} is the torus equatorial optical depth at 1000 Å. M_* is the total stellar mass, $\dot{M}_*^{50}$ is the SFR averaged over 50 Myr, $\dot{M}_*^{age}$ is the SFR averaged over the age of the starburst episode, $\dot{M}_*^{Sph}$ is the SFR of the spheroidal component, and t_* and τ_V are the age of the starburst episode and the initial optical depth of the GMCs that constitute it, respectively.

ID	θ_i °	θ_o	τ_{uv}	r_2/r_1	M_* 10^{11} $M_\odot$	$\dot{M}_*^{50}$	$\dot{M}_*^{age}$ $M_\odot$ yr^{-1}	$\dot{M}_*^{Sph}$	Age 10^7 yr	τ_V
1	$79.1^{+2.3}_{-0.4}$	$47.0^{+1.4}_{-1.3}$	$389.5^{+18.8}_{-39.3}$	$67.4^{+12.8}_{-8.0}$	$2.2^{+0.3}_{-0.5}$	352^{+30}_{-69}	598^{+58}_{-126}	2^{+1}_{-0}	$2.9^{+0.1}_{-0.2}$	$188.9^{+7.1}_{-8.8}$
2	$86.4^{+0.6}_{-1.2}$	$73.5^{+0.0}_{-0.4}$	$300.4^{+44.5}_{-26.5}$	$94.7^{+4.3}_{-12.8}$	$1.2^{+0.3}_{-0.3}$	228^{+71}_{-11}	2192^{+1132}_{-120}	11^{+3}_{-3}	$0.5^{+0.2}_{-0.0}$	$93.8^{+6.9}_{-3.4}$
3	$57.1^{+1.9}_{-0.4}$	$36.6^{+1.4}_{-0.6}$	$1489.9^{+0.1}_{-71.1}$	$26.4^{+71.6}_{-3.3}$	$0.3^{+0.1}_{-0.0}$	75^{+16}_{-18}	195^{+75}_{-60}	2^{+0}_{-0}	$1.9^{+0.6}_{-0.4}$	$51.5^{+9.0}_{-0.5}$
4	$78.9^{+1.0}_{-0.0}$	$37.9^{+1.2}_{-1.9}$	$1070.5^{+70.2}_{-72.5}$	$78.8^{+2.9}_{-3.5}$	$2.6^{+0.2}_{-0.4}$	330^{+77}_{-43}	660^{+172}_{-118}	0^{+0}_{-0}	$2.5^{+0.3}_{-0.3}$	$244.9^{+4.0}_{-15.5}$
5	$67.0^{+0.2}_{-0.1}$	$44.3^{+3.4}_{-6.0}$	$1488.1^{+1.9}_{-32.5}$	$23.1^{+5.6}_{-2.1}$	$0.7^{+0.2}_{-0.1}$	556^{+3}_{-27}	798^{+5}_{-40}	0^{+0}_{-0}	$3.5^{+0.0}_{-0.0}$	$233.6^{+15.4}_{-19.8}$
6	$68.4^{+0.6}_{-1.8}$	$60.0^{+0.4}_{-1.6}$	$1487.3^{+2.4}_{-177.2}$	$60.3^{+8.3}_{-10.0}$	$1.5^{+0.3}_{-0.2}$	68^{+21}_{-9}	170^{+57}_{-30}	0^{+1}_{-0}	$2.0^{+0.3}_{-0.2}$	$119.8^{+28.1}_{-19.1}$
7	$72.3^{+1.6}_{-0.8}$	$37.5^{+25.5}_{-1.5}$	$405.5^{+61.7}_{-41.1}$	$95.4^{+3.5}_{-68.5}$	$0.9^{+0.1}_{-0.3}$	45^{+177}_{-7}	315^{+1733}_{-104}	11^{+0}_{-4}	$0.7^{+2.8}_{-0.2}$	$143.7^{+55.0}_{-4.2}$
8	$71.5^{+0.0}_{-2.4}$	$41.4^{+1.4}_{-3.8}$	$756.7^{+120.1}_{-24.2}$	$70.8^{+1.4}_{-5.1}$	$1.6^{+0.5}_{-0.4}$	228^{+57}_{-5}	378^{+112}_{-8}	3^{+2}_{-1}	$3.0^{+0.5}_{-0.0}$	$231.3^{+17.7}_{-0.1}$
9	$24.7^{+0.3}_{-1.2}$	$56.4^{+2.0}_{-1.5}$	$321.6^{+41.7}_{-18.9}$	$90.3^{+2.0}_{-2.4}$	$0.3^{+0.1}_{-0.0}$	356^{+27}_{-17}	520^{+40}_{-27}	0^{+0}_{-0}	$3.4^{+0.0}_{-0.1}$	$52.1^{+5.6}_{-1.1}$
10	$61.7^{+1.8}_{-0.1}$	$51.0^{+1.8}_{-0.7}$	$1292.9^{+6.4}_{-27.6}$	$26.7^{+0.4}_{-3.5}$	$1.2^{+0.1}_{-0.1}$	422^{+3}_{-69}	683^{+7}_{-122}	11^{+1}_{-0}	$3.1^{+0.0}_{-0.2}$	$57.8^{+6.0}_{-0.7}$
11	$85.5^{+1.4}_{-2.6}$	$69.3^{+2.4}_{-1.1}$	$519.1^{+37.7}_{-20.5}$	$92.0^{+2.2}_{-5.5}$	$0.2^{+0.0}_{-0.0}$	22^{+5}_{-3}	206^{+76}_{-33}	1^{+0}_{-0}	$0.5^{+0.2}_{-0.0}$	$84.3^{+13.7}_{-10.8}$
12	$75.0^{+0.2}_{-0.3}$	$73.3^{+0.2}_{-0.4}$	$1111.8^{+0.6}_{-1.5}$	$25.8^{+1.1}_{-1.3}$	$1.4^{+0.2}_{-0.2}$	333^{+14}_{-9}	482^{+20}_{-13}	0^{+0}_{-0}	$3.5^{+0.0}_{-0.0}$	$111.6^{+3.0}_{-0.6}$
13	$78.2^{+0.8}_{-1.7}$	$60.1^{+2.5}_{-6.1}$	$1488.0^{+2.0}_{-23.3}$	$42.4^{+1.9}_{-3.1}$	$0.9^{+0.4}_{-0.1}$	122^{+62}_{-55}	245^{+134}_{-132}	5^{+2}_{-3}	$2.5^{+0.5}_{-0.7}$	$90.4^{+12.5}_{-9.0}$
14	$64.1^{+0.0}_{-0.3}$	$39.0^{+2.6}_{-0.6}$	$806.5^{+149.3}_{-125.2}$	$36.8^{+3.6}_{-2.2}$	$0.6^{+0.1}_{-0.0}$	220^{+12}_{-14}	322^{+18}_{-23}	5^{+0}_{-1}	$3.4^{+0.0}_{-0.1}$	$169.8^{+2.7}_{-5.2}$
15	$77.3^{+1.6}_{-0.8}$	$65.4^{+3.0}_{-1.6}$	$989.2^{+52.5}_{-33.5}$	$44.5^{+2.2}_{-4.4}$	$0.2^{+0.0}_{-0.0}$	104^{+9}_{-21}	151^{+14}_{-33}	1^{+0}_{-0}	$3.4^{+0.1}_{-0.3}$	$135.0^{+2.9}_{-5.6}$
16	$69.0^{+0.9}_{-0.2}$	$38.9^{+3.4}_{-1.7}$	$1480.5^{+8.3}_{-74.2}$	$25.4^{+11.6}_{-3.0}$	$1.0^{+0.2}_{-0.2}$	189^{+38}_{-121}	298^{+66}_{-260}	10^{+3}_{-1}	$3.2^{+0.3}_{-1.9}$	$56.8^{+4.9}_{-1.4}$
17	$70.1^{+0.3}_{-0.2}$	$38.5^{+6.6}_{-2.4}$	$786.0^{+309.0}_{-57.5}$	$76.5^{+22.4}_{-12.2}$	$0.8^{+0.1}_{-0.1}$	383^{+6}_{-8}	549^{+9}_{-12}	8^{+1}_{-1}	$3.5^{+0.0}_{-0.0}$	$243.5^{+0.9}_{-0.9}$
18	$71.2^{+0.3}_{-1.7}$	$60.0^{+0.5}_{-1.9}$	$1488.3^{+1.7}_{-45.3}$	$40.3^{+5.4}_{-4.9}$	$2.5^{+1.8}_{-0.6}$	50^{+17}_{-25}	87^{+34}_{-54}	12^{+3}_{-6}	$2.9^{+0.6}_{-1.1}$	$241.2^{+7.8}_{-74.4}$
19	$76.8^{+0.0}_{-2.0}$	$45.8^{+0.1}_{-0.9}$	$1455.9^{+14.8}_{-42.2}$	$47.4^{+0.2}_{-1.3}$	$1.4^{+0.0}_{-0.3}$	240^{+25}_{-4}	378^{+40}_{-7}	16^{+0}_{-3}	$3.2^{+0.1}_{-0.0}$	$225.9^{+3.5}_{-4.1}$
20	$71.2^{+0.3}_{-2.0}$	$48.9^{+2.4}_{-3.1}$	$1160.1^{+98.3}_{-44.2}$	$80.9^{+4.4}_{-3.6}$	$0.4^{+0.1}_{-0.1}$	242^{+4}_{-26}	347^{+6}_{-38}	2^{+0}_{-0}	$3.5^{+0.0}_{-0.0}$	$238.3^{+10.7}_{-6.7}$
21	$76.6^{+1.6}_{-0.2}$	$56.5^{+1.3}_{-0.6}$	$920.3^{+54.6}_{-42.9}$	$31.0^{+2.6}_{-4.9}$	$0.3^{+0.0}_{-0.0}$	90^{+13}_{-9}	160^{+23}_{-19}	2^{+0}_{-0}	$2.8^{+0.1}_{-0.2}$	$161.5^{+12.5}_{-14.9}$
22	$50.3^{+1.5}_{-1.0}$	$45.0^{+1.4}_{-1.5}$	$577.1^{+51.8}_{-301.8}$	$29.3^{+18.8}_{-8.3}$	$0.4^{+0.3}_{-0.1}$	128^{+42}_{-18}	255^{+92}_{-49}	3^{+3}_{-0}	$2.5^{+0.3}_{-0.3}$	$75.1^{+18.1}_{-24.1}$
23	$80.4^{+1.3}_{-0.6}$	$38.8^{+0.3}_{-1.0}$	$517.7^{+39.0}_{-33.0}$	$37.4^{+14.6}_{-4.1}$	$0.9^{+0.1}_{-0.1}$	595^{+35}_{-62}	855^{+50}_{-91}	4^{+1}_{-0}	$3.5^{+0.0}_{-0.1}$	$143.7^{+21.2}_{-13.5}$
24	$74.0^{+0.1}_{-1.0}$	$36.1^{+5.2}_{-0.1}$	$640.6^{+88.7}_{-54.9}$	$78.5^{+8.2}_{-13.3}$	$0.6^{+0.2}_{-0.1}$	536^{+6}_{-90}	768^{+9}_{-129}	3^{+1}_{-0}	$3.5^{+0.0}_{-0.0}$	$248.9^{+0.1}_{-8.5}$
25	$68.9^{+2.2}_{-1.3}$	$48.4^{+1.6}_{-0.9}$	$1448.0^{+37.3}_{-805.2}$	$77.4^{+0.3}_{-51.2}$	$6.3^{+2.5}_{-1.3}$	22^{+34}_{-1}	218^{+625}_{-16}	2^{+0}_{-0}	$0.5^{+1.2}_{-0.0}$	$51.3^{+34.2}_{-0.3}$
26	$73.7^{+2.8}_{-2.1}$	$57.0^{+10.5}_{-5.2}$	$1343.2^{+146.0}_{-156.2}$	$80.1^{+18.8}_{-16.2}$	$1.2^{+0.3}_{-0.2}$	435^{+82}_{-75}	625^{+118}_{-108}	12^{+4}_{-3}	$3.5^{+0.0}_{-0.1}$	$234.0^{+15.0}_{-39.1}$
27	$78.9^{+1.0}_{-0.2}$	$48.1^{+5.9}_{-9.2}$	$352.9^{+59.0}_{-101.8}$	$94.5^{+4.4}_{-37.2}$	$1.8^{+0.4}_{-0.6}$	644^{+22}_{-104}	925^{+32}_{-149}	2^{+2}_{-2}	$3.5^{+0.0}_{-0.0}$	$197.5^{+17.6}_{-25.8}$
28	$81.2^{+0.2}_{-0.6}$	$44.9^{+1.0}_{-8.9}$	$623.6^{+105.0}_{-55.9}$	$49.9^{+31.9}_{-7.3}$	$0.9^{+0.5}_{-0.1}$	464^{+75}_{-178}	772^{+137}_{-379}	5^{+1}_{-1}	$3.0^{+0.2}_{-0.9}$	$233.0^{+15.8}_{-34.2}$
29	$73.9^{+0.0}_{-0.4}$	$54.0^{+5.3}_{-7.6}$	$1196.7^{+285.8}_{-159.2}$	$42.2^{+17.3}_{-15.6}$	$0.5^{+0.1}_{-0.1}$	321^{+2}_{-47}	460^{+3}_{-69}	4^{+1}_{-0}	$3.5^{+0.0}_{-0.1}$	$248.7^{+0.3}_{-8.1}$
30	$80.3^{+1.0}_{-1.4}$	$41.1^{+1.9}_{-0.3}$	$766.1^{+11.5}_{-23.2}$	$75.1^{+5.1}_{-1.6}$	$0.5^{+0.1}_{-0.1}$	55^{+26}_{-9}	150^{+89}_{-34}	6^{+1}_{-1}	$1.8^{+0.6}_{-0.3}$	$231.7^{+12.9}_{-17.2}$
31	$76.4^{+0.1}_{-0.3}$	$55.8^{+3.8}_{-4.3}$	$1489.3^{+0.7}_{-64.0}$	$25.7^{+2.6}_{-4.7}$	$0.6^{+0.1}_{-0.1}$	164^{+8}_{-12}	235^{+12}_{-18}	6^{+0}_{-1}	$3.5^{+0.0}_{-0.1}$	$226.8^{+12.1}_{-15.4}$
32	$61.0^{+0.7}_{-1.8}$	$38.6^{+2.1}_{-1.0}$	$1489.1^{+0.9}_{-174.4}$	$21.0^{+6.3}_{-0.0}$	$0.5^{+0.0}_{-0.1}$	114^{+12}_{-18}	165^{+17}_{-29}	4^{+0}_{-1}	$3.5^{+0.0}_{-0.3}$	$117.6^{+10.7}_{-6.0}$
33	$74.0^{+1.3}_{-0.0}$	$36.8^{+2.1}_{-0.4}$	$1362.1^{+91.4}_{-92.7}$	$34.8^{+5.5}_{-5.9}$	$0.5^{+0.1}_{-0.1}$	254^{+8}_{-30}	364^{+11}_{-44}	1^{+0}_{-0}	$3.5^{+0.0}_{-0.1}$	$125.4^{+6.4}_{-4.7}$
34	$75.8^{+0.7}_{-1.8}$	$50.1^{+6.5}_{-5.9}$	$1436.6^{+43.0}_{-76.1}$	$40.3^{+7.4}_{-1.8}$	$1.8^{+0.4}_{-0.4}$	137^{+60}_{-42}	275^{+154}_{-105}	20^{+4}_{-6}	$2.5^{+0.9}_{-0.6}$	$243.6^{+5.4}_{-37.6}$
35	$74.9^{+1.5}_{-0.7}$	$41.7^{+5.7}_{-3.8}$	$1486.1^{+3.9}_{-65.2}$	$23.3^{+9.2}_{-2.3}$	$1.4^{+0.2}_{-0.1}$	223^{+13}_{-41}	375^{+27}_{-78}	0^{+0}_{-0}	$3.0^{+0.1}_{-0.3}$	$244.1^{+4.9}_{-12.5}$
36	$79.3^{+5.2}_{-2.9}$	$48.7^{+7.6}_{-8.1}$	$328.3^{+42.8}_{-37.3}$	$41.1^{+9.5}_{-12.0}$	$1.9^{+0.3}_{-0.2}$	176^{+12}_{-18}	254^{+18}_{-27}	1^{+0}_{-0}	$3.5^{+0.0}_{-0.1}$	$245.3^{+3.7}_{-51.9}$
37	$64.6^{+2.0}_{-0.5}$	$55.2^{+1.5}_{-1.4}$	$791.0^{+94.2}_{-77.1}$	$89.4^{+6.7}_{-8.5}$	$1.6^{+1.2}_{-0.4}$	309^{+53}_{-65}	518^{+111}_{-131}	7^{+3}_{-4}	$3.0^{+0.4}_{-0.4}$	$161.6^{+52.1}_{-33.7}$
38	$73.8^{+0.2}_{-1.9}$	$44.5^{+7.9}_{-8.5}$	$844.4^{+279.9}_{-91.4}$	$46.9^{+5.7}_{-12.0}$	$1.3^{+0.1}_{-0.1}$	259^{+19}_{-49}	373^{+28}_{-72}	0^{+0}_{-0}	$3.5^{+0.0}_{-0.1}$	$188.4^{+15.0}_{-16.2}$
39	$51.7^{+0.1}_{-1.3}$	$47.2^{+0.3}_{-1.4}$	$514.8^{+212.0}_{-92.3}$	$27.3^{+2.5}_{-6.2}$	$0.4^{+0.4}_{-0.1}$	30^{+10}_{-3}	54^{+23}_{-6}	4^{+1}_{-3}	$2.8^{+0.7}_{-0.0}$	$52.9^{+19.0}_{-1.9}$
40	$80.2^{+1.2}_{-0.3}$	$45.9^{+5.5}_{-2.0}$	$1449.6^{+40.4}_{-39.7}$	$22.2^{+4.6}_{-1.2}$	$1.3^{+0.3}_{-0.1}$	140^{+38}_{-14}	274^{+88}_{-29}	0^{+0}_{-0}	$2.6^{+0.4}_{-0.1}$	$248.9^{+0.1}_{-2.6}$
41	$73.9^{+0.1}_{-3.1}$	$40.5^{+1.1}_{-4.4}$	$895.4^{+144.1}_{-153.9}$	$38.1^{+16.2}_{-13.9}$	$0.9^{+0.2}_{-0.2}$	71^{+43}_{-24}	107^{+65}_{-44}	7^{+2}_{-3}	$3.3^{+0.2}_{-0.7}$	$165.7^{+15.6}_{-13.9}$
42	$6.2^{+3.9}_{-1.2}$	$45.0^{+3.6}_{-8.8}$	$299.4^{+113.8}_{-48.3}$	$61.8^{+37.1}_{-7.4}$	$1.9^{+0.4}_{-0.5}$	348^{+31}_{-66}	711^{+77}_{-177}	23^{+5}_{-7}	$2.5^{+0.1}_{-0.4}$	$51.1^{+4.5}_{-0.1}$

with a zero intercept, with a scatter of about 0.1 dex.[5] A power law is not an appreciably better fit. The relation does not appear to depend on t_* but there is a dependence on τ_V, with a flatter slope for more extincted starbursts. There is no correlation between L_{Sb} and $\dot{M}_{sph}$.

Since a more commonly measured value for ULIRGs and LIRGs is their observed (that is, uncorrected for anisotropic emission) total infrared luminosities, we also compare $\dot{M}_{Sb}^{age}$ to L_{Tot}^{o}. We see a

[5]The starburst models assume a Salpeter IMF. With a Chabrier IMF, the SFRs would be about a factor of 0.6 lower.

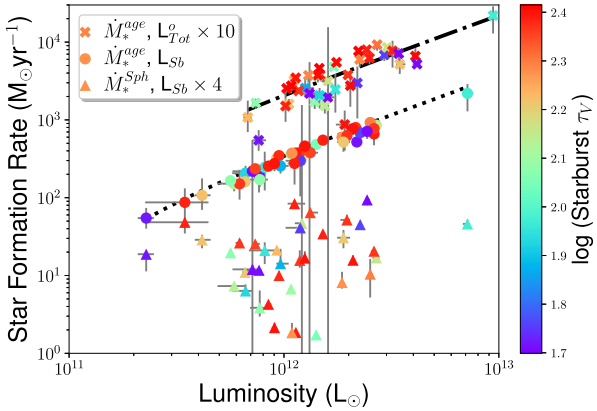

Figure 7. SFRs versus infrared luminosities (starburst or total). The dotted and dot–dashed lines show the fits that give rise to the relationships given in Section 5.1 (equations 2 and 4, respectively).

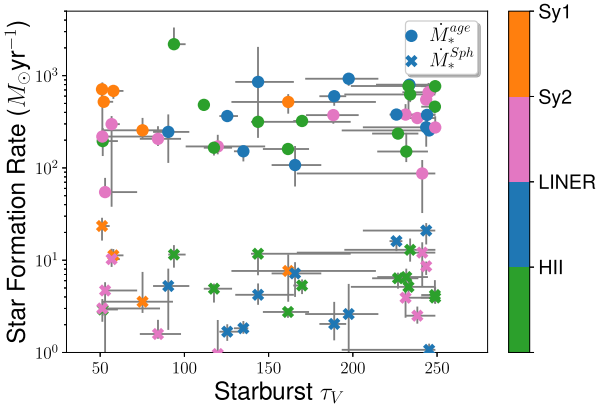

Figure 8. SFRs versus starburst obscuration that is parametrized with the initial optical depth of the molecular clouds τ_V.

correlation, albeit with a wider dispersion:

$$\frac{\dot{M}_{\rm Sb}^{\rm age}}{\rm M_\odot\ yr^{-1}} = (2.24 \pm 0.17) \times 10^{-10} \frac{L_{\rm Tot}^{\rm o}}{\rm L_\odot} - 13 \pm 42 \quad (4)$$

or

$$\frac{\dot{M}_{\rm Sb}^{\rm age}}{\rm M_\odot\ yr^{-1}} = (2.22 \pm 0.10) \times 10^{-10} \frac{L_{\rm Tot}^{\rm o}}{\rm L_\odot} \quad (5)$$

with a zero intercept. More extincted starbursts are more likely to scatter below this relation.

Previous calibrations of the conversion between infrared luminosity and SFR generally derive

$$\frac{\rm SFR}{\rm M_\odot\ yr^{-1}} = (0.6 - 3.2) \times 10^{-10} \frac{L_{\rm IR}}{\rm L_\odot} \quad (6)$$

for 0.1–100 $M_\odot$, a Kroupa IMF, and SFR time-scales of 10 Gyr to 2 Myr (Calzetti et al. 2007; Kennicutt & Evans 2012). Our calibration for ULIRGs is consistent with this range, with a slope consistent with star formation time-scales of $\lesssim$100 Myr. This agrees with the ages we derive for the starburst episode. Previous values are closer to our $L_{\rm Tot}^{\rm o}$ as that is what is typically measured in other studies. We plot SFR against τ_V in Fig. 8. There is a weak positive correlation between τ_V and $\dot{M}_{\rm Sb}^{\rm age}$ (Kendall's $\tau = 0.11$), consistent with more luminous starbursts being systematically more extincted. The correlation does not appear to depend on starburst age. This is reasonable as τ_V is a measure of the obscuration of the starburst episode over its whole duration. There is no dependence between τ_V and $\dot{M}_{\rm sph}$, suggesting that more extincted starbursts do not straightforwardly imply more extincted host galaxies.

5.2 AGN activity

We find AGN in all objects, with anisotropy-corrected infrared luminosities spanning (1×10^{11})–(1.5×10^{13}) $L_\odot$. There is a correlation between $L_{\rm AGN}^{\rm c}$ and $\theta_{\rm o}$, with more luminous AGN having larger values of $\theta_{\rm o}$ (Fig. 9). Conversely, there is no relation between $L_{\rm AGN}^{\rm c}$ and $\theta_{\rm i}$. Instead plotting the obscurer parameters against $L_{\rm AGN}^{\rm o}$ gives conceptually identical results. This is unlikely to be a selection effect unless there exists a population of low-redshift ULIRGs with luminous AGN that have both high covering fractions and very cold SEDs. Thus, more infrared-luminous AGNs in ULIRGs seem to be associated with smaller covering fractions. This is also consistent with the general class of 'receding torus' models (Lawrence 1991) according to which the covering factor of the torus decreases with increasing luminosity due to dust sublimation.

Conversely, there is no relation between corrected AGN luminosity and either r_2/r_1 or $\tau_{\rm uv}$ (Fig. 9). There is also no dependence between r_2/r_1 and $\theta_{\rm o}$. It is notable that more than half of the objects have a relatively compact obscurer, with $r_2/r_1 \sim$20–40, but there does not appear to be anything unusual in the other properties of the systems with compact obscurers.

The obscurer geometry affects the observed AGN luminosity $L_{\rm AGN}^{\rm o}$, obtained by integrating the observed SED over 4π sr. The correction of the AGN luminosity depends on the intrinsic AGN luminosity, with more intrinsically luminous AGN having a larger correction (Fig. 10). The mean $L_{\rm AGN}^{\rm o}/L_{\rm AGN}^{\rm c}$ ratio of the sample is 0.40, but more luminous AGNs have a greater difference between $L_{\rm AGN}^{\rm o}$ and $L_{\rm AGN}^{\rm c}$, with $L_{\rm AGN}^{\rm o}/L_{\rm AGN}^{\rm c} = 0.51$ at $L_{\rm AGN}^{\rm c} < 2 \times 10^{12}$ $L_\odot$ and $L_{\rm AGN}^{\rm o}/L_{\rm AGN}^{\rm c} = 0.17$ at $L_{\rm AGN}^{\rm c} > 2 \times 10^{12}$ $L_\odot$. Moreover, the relation appears to depend on $\theta_{\rm i}$, with a clearer relation for objects viewed closer to edge-on, consistent with a higher optical depth in the equatorial plane. The observed-to-corrected luminosity ratio does not, however, seem to depend as strongly on the other torus parameters (Fig. 11). Whether or not the viewing angle intersects the torus is the primary driver of the size of the anisotropy correction.

Finally, we examine the bolometric AGN luminosity correction as a function of obscurer geometry (Fig. 12). The bolometric corrections range from factors of 1.25 to 3.10. As expected, there is a strong dependence on torus half-opening angle, especially when the line of sight intersects the torus. There is, however, no significant dependence on the other AGN parameters. The magnitude of the bolometric correction also does not seem to depend on AGN luminosity.

5.3 The starburst–AGN connection

Both star formation and AGN contribute significantly in most ULIRGs. The starburst usually contributes the majority of infrared emission except at $L_{\rm tot}^{\rm c} \gtrsim 3 \times 10^{12}$ $L_\odot$ when AGN starts to dominate. There is no observable relation between $L_{\rm Sb}$ and $L_{\rm AGN}^{\rm c}$ or $L_{\rm AGN}^{\rm o}$ (Fig. 13). Objects with high $L_{\rm AGN}^{\rm c}$ do not have low $L_{\rm Sb}$ in absolute terms. Moreover, there is no observed relation between any of $L_{\rm tot}^{\rm c}$, $L_{\rm Sb}$, $L_{\rm AGN}^{\rm c}$, or starburst fraction with starburst age. We also see no trends in any of $L_{\rm tot}^{\rm c}$, $L_{\rm Sb}$, and $L_{\rm AGN}^{\rm c}$ with optical spectral classification. A conceptually similar disconnect between starburst and AGN luminosity has also recently been found in other classes of object, including SDSS quasars (Ma & Yan 2015; Pitchford et al. 2016), though see also Harris et al. (2016). Neither do we find

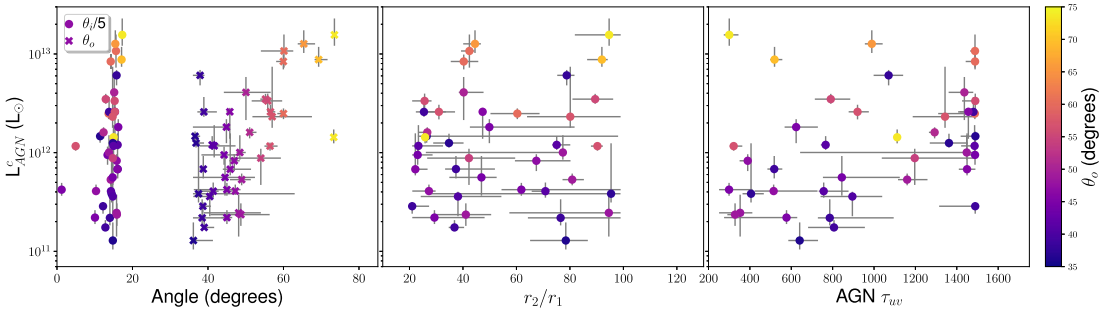

Figure 9. Anisotropy-corrected infrared AGN luminosity as a function of three obscurer parameters: left: inclination and half-opening angles, middle: outer to inner torus radius, and right: torus obscuration.

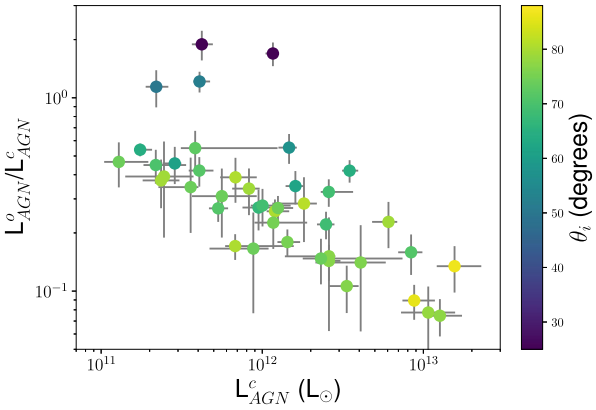

Figure 10. Observed-to-corrected luminosity ratio versus anisotropy-corrected infrared AGN luminosity. The scatter in this relation appears smaller for larger values of $\theta_i - \theta_o$, suggesting that the relation is tighter when the viewing angle is 'well into' the torus.

evidence that τ_V, τ_{uv}, θ_o, or r_2/r_1 depend on luminosity (Fig. 14), or evidence of a relation between τ_V and τ_{uv} (Fig. 15).

The overall impression is an at best weak *direct* connection between starburst and AGN activity. The lack of trends between starburst and AGN luminosities suggests that they do not strongly affect each other. The lack of trends with optical spectral class is also expected if optical spectral class is primarily a function of orientation. Moreover, there is no evidence that this (lack of) connection evolves over the lifetime of the starburst.

5.4 Dual AGNs

Two ULIRGs in the sample – IRAS 01003−2238 and Mrk 1014 – show evidence of dual AGNs in their SED fits (Fig. 16 and Table 6). At face value, this implies a dual AGN fraction of about 5 per cent in local ULIRGs, but this value is unlikely to be correct. There is independent corroborating evidence of at least two other objects; see below. Tadhunter et al. (2017) discovered a tidal disruption event (TDE) in IRAS 01003−2238 and conclude that TDEs are much more common in ULIRGs compared to the general galaxy population probably because of the presence of dual AGNs in the process of merging. However, the fits are likely biased. The fits are only sensitive to dual AGNs where the second AGN is sufficiently different in one or more physical parameters. We thus cannot rule out the possibility that there may be other dual AGNs with both AGNs being broadly similar except, potentially, in luminosity. There is, for example, evidence of a triple AGN in NGC 6240 (Kollatschny et al. 2020) and a dual AGN in Mrk 231 (Yan et al. 2015). However, we do not see any evidence of more than one AGN from the SEDs of NGC 6240 and Mrk 231. So we interpret the 5 per cent of ULIRGs harbouring a dual AGN as a lower limit.

5.5 Polar dust

For a few objects, the emission from AGN polar dust is suggested from the SEDs. To model the emission of polar dust, we use a library of spherical optically thick polar dust clouds for which we carry out a full radiative transfer calculation with the exception that we do not solve for the temperature of the dust but we assume a constant temperature for all grain species. We also assume that the clouds have a uniform density. There is therefore only one parameter in this model, the temperature of the polar dust clouds that we assume to be 900 K. In addition, we have the scaling factor f_p.

In a number of AGNs, there is clear evidence by high-resolution imaging in the near- and mid-infrared that some of the nuclear emission is not coming from the torus but from the ionization cones. This has been observed in NGC 1068 since the early 1990s by Braatz et al. (1993) and Cameron et al. (1993), in Circinus by Tristram et al. (2007), and other AGNs by Hönig et al. (2013) and more recently in Asmus (2019). The model of Efstathiou, Hough & Young (1995) for NGC 1068 explored the presence of polar dust in the nucleus. Efstathiou (2006) and Efstathiou et al. (2013) also discussed the idea that the mid-infrared emission of IRASF 10214+4724 is due to polar dust. Mattila et al. (2018) also interpreted the near-infrared emission arising from the dust-enshrouded TDE in Arp 299 as arising from polar dust that was illuminated by the TDE. A similar phenomenon was also observed in the LIRG IRAS 23436+5257 by Kool et al. (2020).

It is not clear how widespread polar dust is in ULIRGs. In the HERUS sample, we do not find much evidence for it (three ULIRGs or about 8 per cent of the sample) but this may be due to the large optical depths to the nuclear region or because the covering factor is too low to detect with SED fitting. We see evidence of polar dust in the following ULIRGs: IRAS 05189−2524, IRAS 07598+6508, and IRAS 13451+1232. IRAS 07598+6508 is the only unobscured quasar in the sample, whereas IRAS 05189−2524 shows broad lines in polarized flux (Young et al. 1996) that also requires a relatively unobscured view to the nucleus. The fraction of AGN luminosity due to polar dust ranges from ∼1 to 10 per cent, which is also to a good approximation the covering factor of polar dust.

6 COMPARISON WITH OTHER LUMINOSITIES

In order to assess the robustness of our SED decomposition results and our estimate of the correction of the AGN luminosity

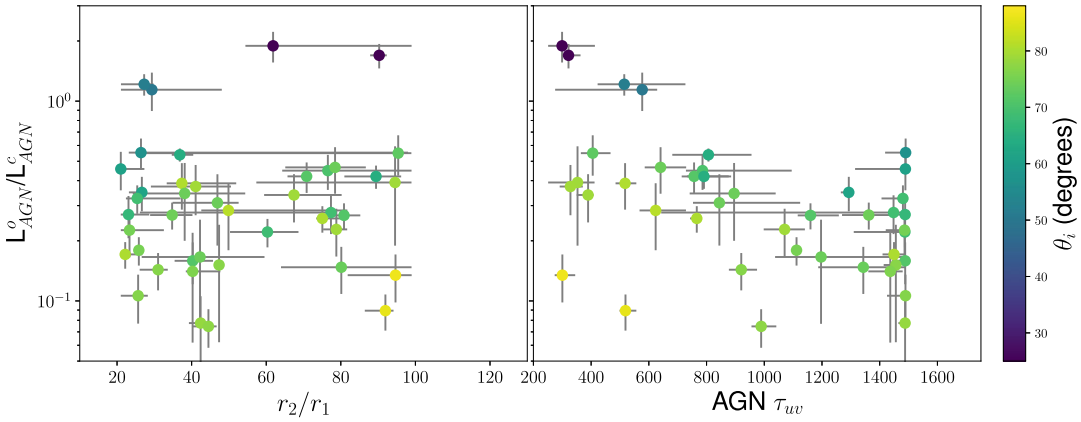

Figure 11. Observed-to-corrected AGN luminosity ratio versus AGN obscurer parameters.

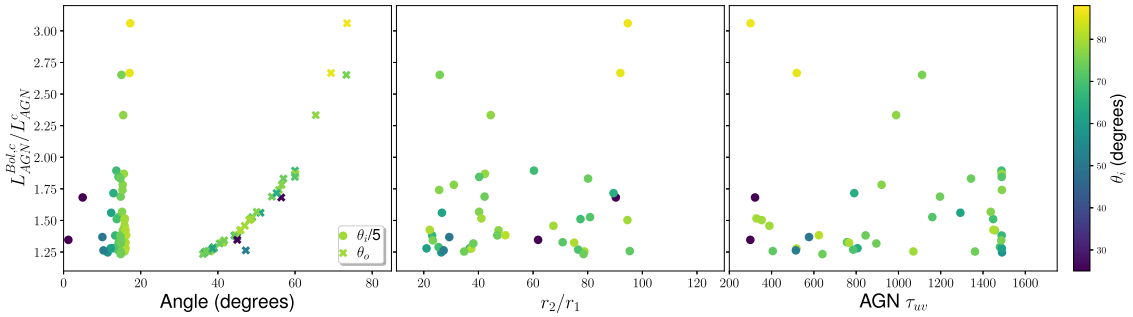

Figure 12. Anisotropy-corrected bolometric-to-infrared AGN luminosity ratio versus obscurer parameters.

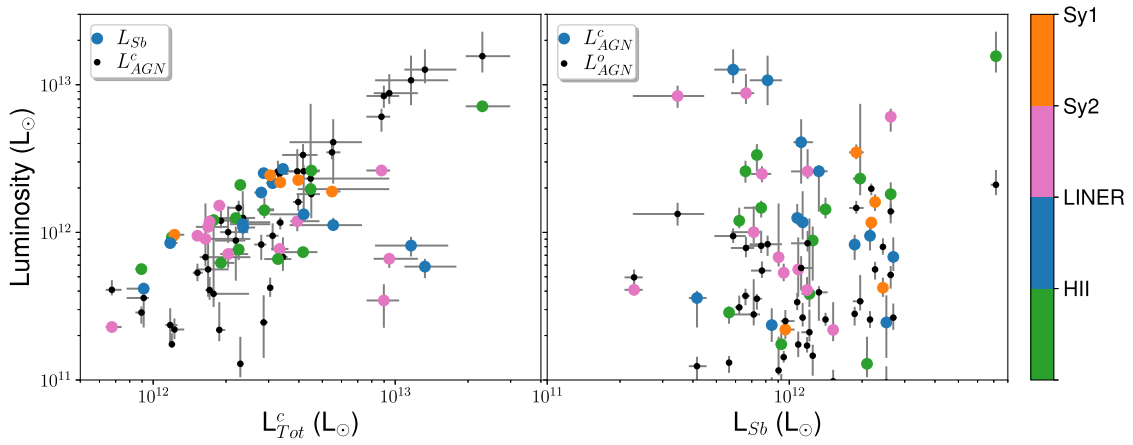

Figure 13. Left: Starburst and anisotropy-corrected AGN luminosity versus total corrected infrared luminosity. The starburst usually contributes the majority of infrared emission except at $L^c_{\rm tot} \gtrsim 3 \times 10^{12}\,{\rm L}_\odot$ when AGN starts to dominate. Right: Observed and anisotropy-corrected AGN luminosity versus Starburst luminosity. There is no observable relation between $L_{\rm Sb}$ and $L_{\rm AGN}$. In both cases, we see no dependence on optical spectral type.

due to anisotropic torus emission, we compare our results to the following:

(i) Total infrared luminosities derived from the *IRAS* fluxes (Sanders & Mirabel 1996), and those presented by Klaas et al. (2001) from fitting a modified blackbody dust model.

(ii) AGN infrared luminosities from FR06, SKIRTOR, and Siebenmorgen15.

(iii) AGN bolometric luminosities from FR06, SKIRTOR, and Siebenmorgen15, as well as Nardini et al. (2009) and Veilleux et al. (2009).

A comparison of the likelihoods from the fits with all four combinations of models is given in Fig. 17, and of the luminosities in Fig. 18. It is clear that the CYGNUS models nearly always give better fits than the FR06 and SKIRTOR models, and usually better fits than the Siebenmorgen15 models. We discuss possible reasons for this and their effect on the predicted AGN luminosities in Section 8.

The uncorrected total infrared luminosities from CYGNUS are consistent with prior estimates (Sanders & Mirabel 1996) though slightly higher that those based on pure modified blackbody dust models, likely due to lack of PAH emission in these models (Klaas et al. 2001).

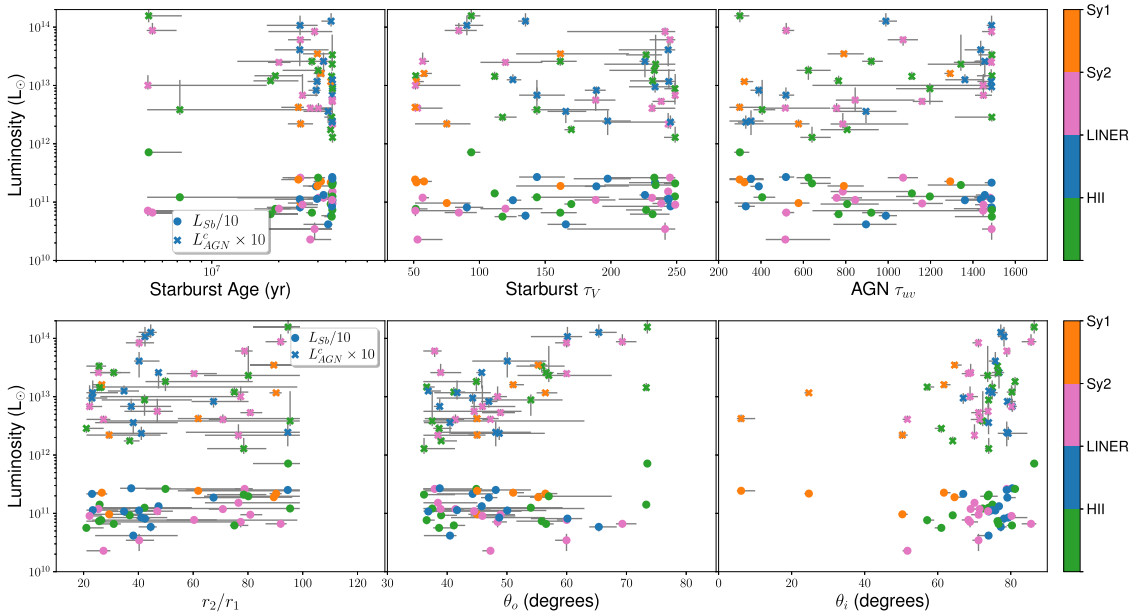

Figure 14. Starburst and AGN luminosity versus starburst and AGN properties.

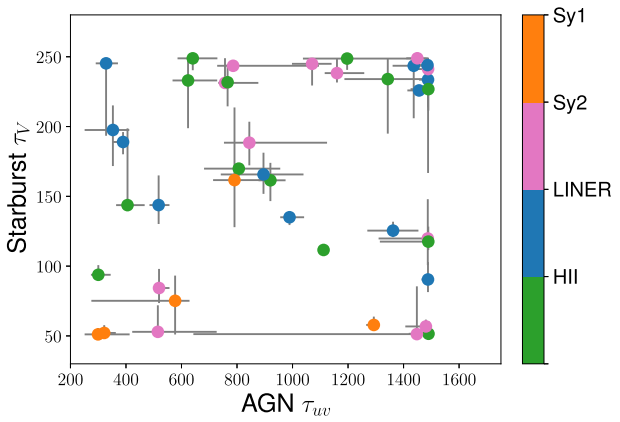

Figure 15. τ_V against τ_{uv}. There is no evidence of a relation, even after accounting for e.g. optical spectral type.

The infrared AGN luminosities from CYGNUS and FR06 are in general consistent, though with significant dispersion. The infrared AGN luminosities from SKIRTOR and Siebenmorgen15 are, however, systematically lower than those from either FR06 or CYGNUS. As we also discuss in Section 8, this may be related to the fact that the SKIRTOR fits are generally poorer than those with CYGNUS. As the same effect is also observed with the Siebenmorgen15 models, this is most probably also related to the two-phase geometry that is the common characteristic of SKIRTOR and Siebenmorgen15.

With all combinations of models, a significant correction of the AGN luminosities due to anisotropic AGN emission is needed. In the most extreme objects, IRAS 00397−1312 and IRAS 08572+3915, the corrected luminosities predicted by the CYGNUS, FR06, and SKIRTOR combinations agree very well. This is not the case for the Siebenmorgen15 models but the fits with this combination are not very good. The CYGNUS corrections are usually but not always the highest. The SKIRTOR and Siebenmorgen15 corrections do not bring their luminosities in line with either CYGNUS or FR06.

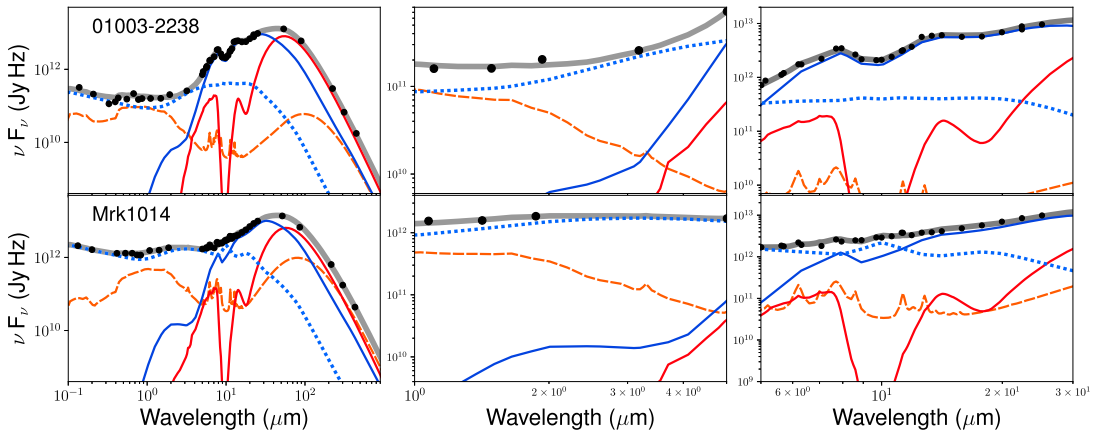

Figure 16. SED fit plots of the ULIRGs with dual AGNs: spheroidal host (orange), starburst (red), edge-on AGN torus (solid blue), face-on AGN torus (dotted blue), and total (grey).

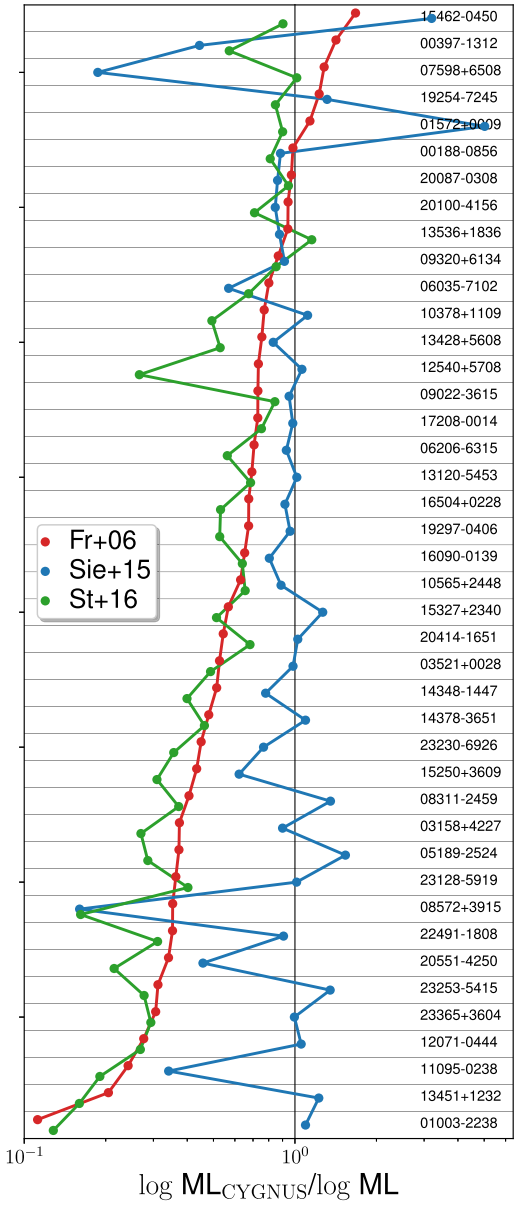

Figure 17. Comparison of the likelihood ratios of all objects fitted with the CYGNUS, FR06, SKIRTOR, and Siebenmorgen15 models. The plot shows the ratio of the FR06, SKIRTOR, and Siebenmorgen15 likelihood ratios, relative to the CYGNUS values. The CYGNUS and Siebenmorgen15 models give systematically better fits than FR06 and SKIRTOR. CYGNUS is usually better overall.

The bolometric AGN luminosities from CYGNUS and FR06 are also in general consistent, and usually higher than those from SKIRTOR and Siebenmorgen15. All are higher than the bolometric AGN luminosities from Nardini et al. (2009) though their bolometric luminosities are in reality infrared luminosities, so this is expected. The comparison with the Veilleux et al. (2009) bolometric luminosities is more interesting. The Veilleux et al. (2009) luminosities are not based on SED fits, but instead are averages of five different approaches. The CYGNUS uncorrected luminosities are systematically lower than those from Veilleux et al. (2009) but the corrected ones are often consistent. We conclude that empirical calibrations such as those in Veilleux et al. (2009) do capture some of the anisotropy correction.

7 COMPARISON WITH OTHER INCLINATION ANGLES

The inclination angle of the AGN obscurer relative to the line of sight plays an important role in determining AGN luminosities. We therefore compare the inclination angles inferred from the CYGNUS models to those derived from other approaches.

It is possible to observationally infer inclination angles of several galactic components – the molecular or atomic gas disc, the X-ray obscurer, the infrared obscurer, and the stellar disc. These estimates are challenging and usually carry large uncertainties. Few such measures are available; nevertheless, such comparisons can be illuminating, so we plot the values derived by all combinations of models with all available literature values in Fig. 19.

There is no a priori reason to expect alignment of different components, but it is reasonable to expect some level of systematic consistency. In general, however, there is consistency between the CYGNUS-derived inclination angles and those obtained from other methods. The CYGNUS values may be slightly biased towards edge-on compared to the stellar disc derived values, but in most cases there is consistency well within 2σ. Moreover, as discussed by Dasyra et al. (2006), stellar disc inclination angles carry substantial uncertainty, so it is plausible that the bias is in these measures rather than the CYGNUS values. Compared to the molecular disc values, there is consistency, except in one case: the molecular gas disc in the appropriate nucleus of Arp 220 (Scoville et al. 2017). It is inclined at 30°, while the CYGNUS value is 80.2° (both from pole-on). Scoville et al. (2017) note, however (their section 5.2), that their inclination angle is inconsistent with the supernova remnant distribution in Lonsdale et al. (2006b). Moreover, the inclination angle inferred by Lonsdale et al. (2006b) is consistent with the CYGNUS value. Resolving this contradiction is beyond the scope of this paper, though it does suggest that the CYGNUS value is plausible. Finally, compared to the X-ray derived values there is consistency in one case but not in another. It is (perhaps) unreasonable to expect consistency here, though consistency between CYGNUS and X-ray-derived inclination angles has been noted previously (Farrah et al. 2016). We here simply note the result as a starting point for further work.

8 DISCUSSION

As we can see in Fig. 17, the fits with SKIRTOR and FR06 are consistently worse than with CYGNUS or Siebenmorgen15. SKIRTOR is a two-phase torus model, whereas CYGNUS and FR06 are both smooth models. There are also differences in the assumed 'shape' of the torus. Both SKIRTOR and FR06 assume a flared disc geometry, whereas in CYGNUS the torus has the tapered disc geometry suggested by Efstathiou & Rowan-Robinson (1995). This may be the reason why CYGNUS is giving overall better fits than FR06. So overall the conclusion we can draw from our analysis is that a smooth tapered disc is the best approximation for the distribution of dust in the torus among the four distributions considered by the models.

The fundamental difference between a smooth and clumpy or two-phase geometry for the torus is that in the latter case we can see through gaps in the cloud distribution to the inner torus. This has the effect of making the emission from a clumpy torus be generally more isotropic and appear less obscured. A clumpy or two-phase torus also cannot produce deep enough silicate absorption features in order to fit well most of the galaxies in our sample. In cases where the SKIRTOR fit is poor, such as in IRAS 11095−0238 or IRAS 03158+4227, this

Table 6. Fitted parameters and derived physical quantities for the dual AGN ULIRGs.

ID	L^{o}_{AGN} 10^{12} $L_{\odot}$	L^{c}_{AGN} 10^{12} $L_{\odot}$	θ_{o} °	θ_{i} °	τ_{uv}	r_2/r_1	L_{Sb} 10^{12} $L_{\odot}$	τ_V	t_* 10^7 yr	M_* 10^{10} $M_{\odot}$
3	$1.12^{+0.20}_{-0.21}$	$2.47^{+0.44}_{-0.46}$	$39.6^{+1.9}_{-3.5}$	$61.8^{+2.2}_{-0.1}$	1408^{+82}_{-172}	54^{+5}_{-11}	$0.73^{+0.05}_{-0.07}$	204^{+45}_{-10}	$0.76^{+0.39}_{-0.25}$	$1.18^{+5.72}_{-0.13}$
	$0.09^{+0.06}_{-0.01}$	$0.04^{+0.02}_{-0.005}$	$40.7^{+6.2}_{-4.7}$	$\sim$10.0	$\geq$693	37^{+34}_{-16}				
42	$2.21^{+0.47}_{-0.28}$	$12.8^{+2.8}_{-1.6}$	$52.5^{+3.3}_{-2.0}$	$71.0^{+0.5}_{-1.1}$	1489^{+1}_{-66}	37^{+6}_{-9}	$1.17^{+0.20}_{-0.27}$	236^{+13}_{-44}	$2.19^{+0.66}_{-1.69}$	$16.1^{+7.9}_{-5.8}$
	$0.78^{+0.15}_{-0.11}$	$0.46^{+0.09}_{-0.04}$	$59.9^{+3.8}_{-3.8}$	$\sim$10.0	327^{+88}_{-76}	91^{+8}_{-8}				

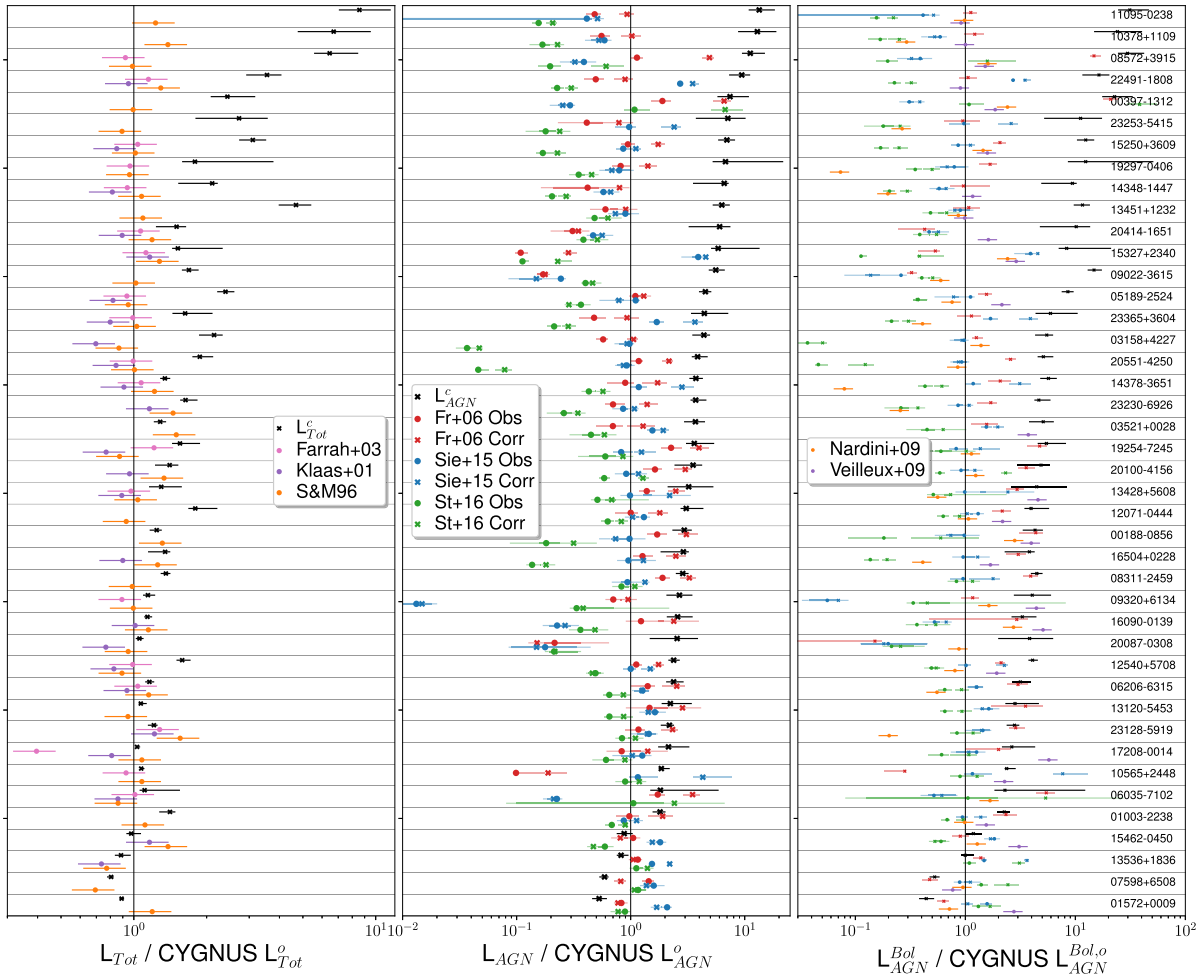

Figure 18. Comparison of luminosities. Left: The total infrared luminosities (observed and corrected) from the CYGNUS fits, compared against those derived by Sanders & Mirabel (1996), Klaas et al. (2001), and Farrah et al. (2003). The values are presented as the ratios to the observed CYGNUS luminosities. Middle: The AGN infrared luminosities (observed and corrected) from the CYGNUS fits, compared against those from the FR06, SKIRTOR, and Siebenmorgen15 model fits. The values are presented as the ratios to the observed CYGNUS luminosities. Right: The corrected AGN bolometric luminosities from the CYGNUS fits, compared to those from the FR06 and SKIRTOR fits, and to those derived by Nardini et al. (2009) and Veilleux et al. (2009).

will usually manifest itself with a lower AGN luminosity as the model underpredicts the emission at 20–30 μm where the torus emission peaks.

The conclusion that a smooth tapered disc is a better approximation than the SKIRTOR and Siebenmorgen15 geometry is not necessarily at odds with the detections of compact tori in nearby Seyferts like NGC 1068 with ALMA (García-Burillo et al. 2016; Alonso-Herrero et al. 2018; Combes et al. 2019). It is important to note that even in NGC 1068 the compact torus of a few parsec diameter is surrounded by a circumnuclear disc of diameter of the order of 100 parsec that dominates the far-infrared and submillimetre emission. Lyu & Rieke (2021) also recently presented results from reverberation mapping of the nucleus of NGC 4151 at 1–40 μm that shows lack of variability at 20–40 μm. This implies that the 20–40 μm emitting region is more extended than that predicted by clumpy torus models and more consistent with smooth models. Because of the limited spatial resolution of the infrared data in this sample what we are modelling with the AGN torus models are structures similar to the circumnuclear disc in NGC 1068 or the extended structure in NGC 4151 inferred by Lyu & Rieke (2021). This may explain why the smooth torus models provide better fits to the SEDs of the ULIRGs in our sample.

It is also interesting to consider if the results presented here are consistent regarding the ratio of predicted type 1 and type 2 AGNs.

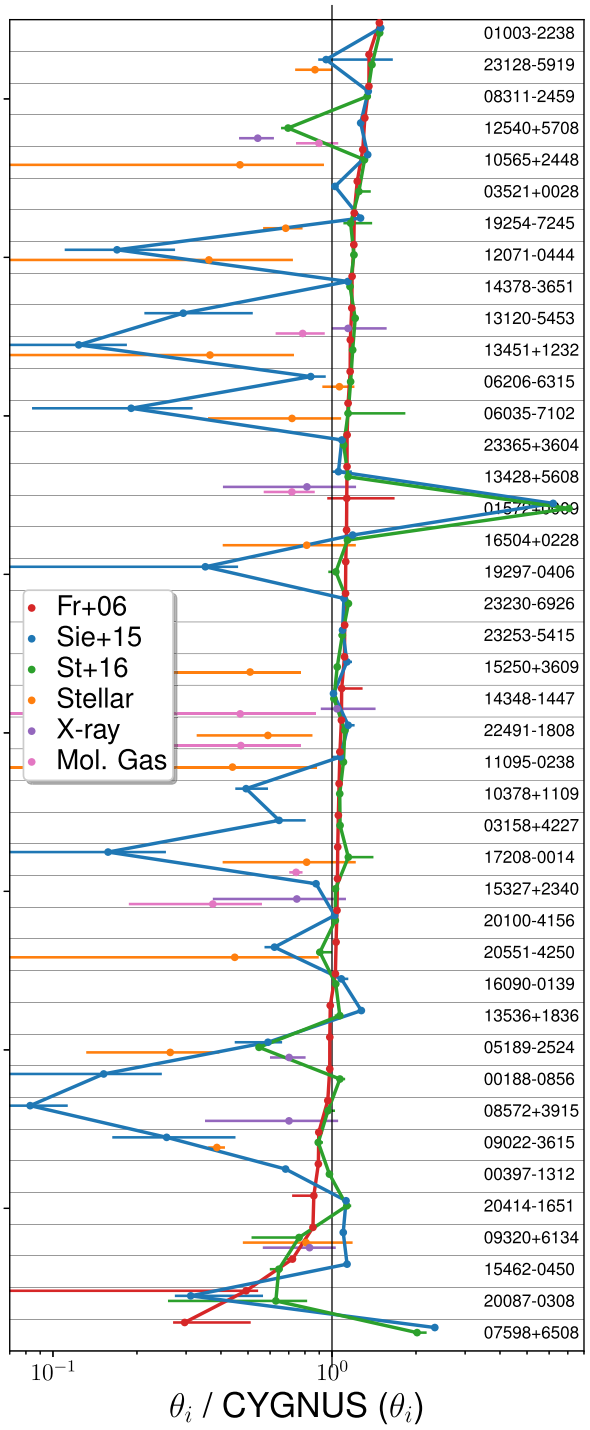

Figure 19. Comparison of inclination angles derived with various methods. The values are given as the ratio to the CYGNUS inclination angle. Inclination angles for the X-ray obscurer are taken from Feruglio et al. (2015), Oda et al. (2017), Xu et al. (2017), and Yamada et al. (2021). Stellar disc inclination angles are from Dasyra et al. (2006), Reunanen, Tacconi-Garman & Ivanov (2007), Bellocchi et al. (2013), and Medling et al. (2014). Molecular or atomic gas disc inclination angles are taken from Carilli, Wrobel & Ulvestad (1998), Carilli & Taylor (2000), Scoville et al. (2017), Privon et al. (2017), and Pereira-Santaella et al. (2018).

We have a total of 45 AGNs in this sample (including the 2 type 1 AGNs in the dual cases and 3C 273). Out of these, five are type 1 (IRAS 07598+6508, Mrk 231, 3C 273, and the two dual AGNs). So we have a minimum type 1 fraction of 5/45 = 11.1 per cent. Assuming that all the tori in these AGNs have $\theta_o = 30^\circ$, then we should expect a type 1 fraction of ∼13 per cent. So we conclude that our results are consistent.

With the more detailed analysis presented in this paper, which includes the addition of the emission of the host galaxy, we confirm the result obtained by Efstathiou et al. (2014) for IRAS 08572+3915 namely that it is intrinsically a hyperluminous infrared galaxy. The predicted higher luminosity is due to the anisotropic emission of the torus. The only way to avoid this conclusion is if the AGN torus was more 'spherical' than predicted in our model, but more spherical models approaching a torus covering factor of 90 per cent are included in our AGN torus libraries. There is also clear evidence of large outflows in this ULIRG that suggest a non-spherical geometry (Rupke & Veilleux 2013; Spoon et al. 2013; González-Alfonso et al. 2017). Attempts to fit the SED of IRAS 08572+3915 with a foreground screen model have also not been successful (Levenson et al. 2007). IRAS 08572+3915 is one of the first ULIRGs that will be targets of *JWST*, so we will be able to elucidate further the nature of this interesting system in the near future. We also find that there are three other ULIRGs that are predicted to be hyperluminous. These are IRAS 00397−1312, IRAS 10378+1109, and IRAS 11095−0238, which show very similar SEDs to IRAS 08572+3915. IRAS 00397−1312 belongs to class 3A of Spoon et al. (2007), which is associated with a deep silicate absorption feature and weak PAH emission. Another galaxy that belongs to class 3A of Spoon et al. (2007) is IRAS 00188−0856. This ULIRG is also fitted with a similar model as the other objects in this class but is not predicted to be hyperluminous.

In Arp 220, we find evidence of an AGN that may be consistent with the prediction of González-Alfonso & Sakamoto (2019) for the presence of a luminous AGN with an infrared luminosity of (0.76–1.2) × 10^{12} $L_\odot$ in the western nucleus. Scoville et al. (2017) also identified a compact Keplerian component in the western nucleus of Arp 220. We also note that three ULIRGs have significant contribution in the submillimetre from cold dust in the host galaxy component. In two of the cases, IRAS 19254−7245 (SuperAntena) and IRAS 23253−5415, cold dust dominates the submillimetre emission. These two galaxies are known to have prominent tidal tails extending for tens of kpc. IRAS 13451+123 is a radio galaxy, so there may be contribution from synchrotron emission in the submillimetre, which is not included in our models. These three galaxies would be interesting to study with ALMA, NOEMA, or SMA.

9 CONCLUSIONS

We have presented a detailed analysis of the SEDs of the HERUS local ULIRGs using radiative transfer models and an MCMC SED fitting code.

(i) We fit the SEDs of the ULIRGs in our sample with four combinations of radiative transfer models. Two of the combinations assume a smooth torus geometry (Efstathiou & Rowan-Robinson 1995; FR06) and two combinations a two-phase geometry (Siebenmorgen et al. 2015; Stalevski et al. 2016). We find that the smooth CYGNUS models (Efstathiou & Rowan-Robinson 1995) provide better fits than the other combinations of models.

(ii) All objects harbour high rates of star formation. There is a strong correlation between $L_{\rm Sb}$ and $\dot{M}_{\rm Sb}^{\rm age}$ and more luminous

starbursts are unlikely to be systematically different in either age or extinction to less luminous starbursts.

(iii) We find bolometrically significant AGN in all objects. The obscurer geometry can substantially affect the observed AGN luminosity, by factors of up to ∼10 in tori viewed nearly edge-on. This is due to the anisotropic nature of the emission of the torus that is to a large extent independent of the torus model. The correction may depend on luminosity; more infrared-luminous AGNs in ULIRGs seem to be associated with both smaller covering fractions and viewing angles closer to equatorial. It is also consistent with the general class of 'receding torus' models.

(iv) We see no relation between AGN luminosity and either r_2/r_1 or τ_{uv}. Moreover, neither r_2/r_1 nor τ_{uv} appears to depend on θ_o. This is consistent with only the covering fraction having a relation with L^c_{AGN}, but other properties of the obscurer being independent of luminosity and covering fraction.

(v) We find an observed dual AGN fraction of about 5 per cent. Due to observational biases, this is likely a lower limit.

(vi) We find evidence of significant amounts of polar dust in three ULIRGs or about 8 per cent of the sample. This may be considered as a lower limit as in other objects polar dust emission may be obscured due to the large optical depths of ULIRGs.

ACKNOWLEDGEMENTS

We would like to thank the referee Ralf Siebenmorgen for his comments and suggestions that led to an improvement of the paper. The work leading to this paper has received funding from the European Union Seventh Framework Programme FP7/2007-2013/ under grant agreement no. 607254. This publication reflects only the authors' view and the European Union is not responsible for any use that may be made of the information contained therein. AE, DF, and VPL acknowledge support from the project EXCELLENCE/1216/0207/GRATOS funded by the Cyprus Research & Innovation Foundation. AE and VPL acknowledge support from the project CYGNUS funded by the European Space Agency. DR acknowledges support from STFC through grant ST/S000488/1. EGA is a Research Associate at the Harvard–Smithsonian Center for Astrophysics and thanks the Spanish Ministerio de Economía y Competitividad for support under projects ESP2017-86582-C4-1-R and PID2019-105552RB-C41. The NASA/IPAC Extragalactic Database (NED) is funded by the National Aeronautics and Space Administration and operated by the California Institute of Technology.

DATA AVAILABILITY

The data underlying this article are available in the article or are publicly available in data bases like The Cornell Atlas of *Spitzer*/Infrared Spectrograph Sources (CASSIS) and the NASA Extragalactic Database (NED).

REFERENCES

Alexander D. M., Hough J. H., Young S., Bailey J. A., Heisler C. A., Lumsden S. L., Robinson A., 1999, MNRAS, 303, L17
Alonso-Herrero A., Quillen A. C., Simpson C., Efstathiou A., Ward M. J., 2001, AJ, 121, 1369
Alonso-Herrero A., Quillen A. C., Rieke G. H., Ivanov V. D., Efstathiou A., 2003, AJ, 126, 81
Alonso-Herrero A. et al., 2018, ApJ, 859, 144
Armus L. et al., 2009, PASP, 121, 559
Asmus D., 2019, MNRAS, 489, 2177
Barger A. J., Cowie L. L., Sanders D. B., Fulton E., Taniguchi Y., Sato Y., Kawara K., Okuda H., 1998, Nature, 394, 248
Bellocchi E., Arribas S., Colina L., Miralles-Caballero D., 2013, A&A, 557, A59
Boquien M., Burgarella D., Roehlly Y., Buat V., Ciesla L., Corre D., Inoue A. K., Salas H., 2019, A&A, 622, A103
Braatz J. A., Wilson A. S., Gezari D. Y., Varosi F., Beichman C. A., 1993, ApJ, 409, L5
Bridge C. R. et al., 2013, ApJ, 769, 91
Bruzual G., Charlot S., 1993, ApJ, 405, 538
Bruzual G., Charlot S., 2003, MNRAS, 344, 1000
Calzetti D. et al., 2007, ApJ, 666, 870
Cameron M., Storey J. W. V., Rotaciuc V., Genzel R., Verstraete L., Drapatz S., Siebenmorgen R., Lee T. J., 1993, ApJ, 419, 136
Carilli C. L., Taylor G. B., 2000, ApJ, 532, L95
Carilli C. L., Wrobel J. M., Ulvestad J. S., 1998, AJ, 115, 928
Casey C. M., Narayanan D., Cooray A., 2014, Phys. Rep., 541, 45
Clements D. L. et al., 2018, MNRAS, 475, 2097
Combes F. et al., 2019, A&A, 623, A79
da Cunha E., Charlot S., Elbaz D., 2008, MNRAS, 388, 1595
Dasyra K. M. et al., 2006, ApJ, 651, 835
Dopita M. A. et al., 2005, ApJ, 619, 755
Dullemond C. P., van Bemmel I. M., 2005, A&A, 436, 47
Eales S. et al., 2010, PASP, 122, 499
Efstathiou A., 2006, MNRAS, 371, L70
Efstathiou A., Rowan-Robinson M., 1994, MNRAS, 266, 212
Efstathiou A., Rowan-Robinson M., 1995, MNRAS, 273, 649
Efstathiou A., Rowan-Robinson M., 2003, MNRAS, 343, 322
Efstathiou A., Siebenmorgen R., 2005, A&A, 439, 85
Efstathiou A., Siebenmorgen R., 2009, A&A, 502, 541
Efstathiou A., Hough J. H., Young S., 1995, MNRAS, 277, 1134
Efstathiou A., Rowan-Robinson M., Siebenmorgen R., 2000, MNRAS, 313, 734
Efstathiou A., Christopher N., Verma A., Siebenmorgen R., 2013, MNRAS, 436, 1873
Efstathiou A. et al., 2014, MNRAS, 437, L16
Efstathiou A. et al., 2021, MNRAS, 503, L11
Eisenhardt P. R. M. et al., 2012, ApJ, 755, 173
Farrah D., Serjeant S., Efstathiou A., Rowan-Robinson M., Verma A., 2002, MNRAS, 335, 1163
Farrah D., Afonso J., Efstathiou A., Rowan-Robinson M., Fox M., Clements D., 2003, MNRAS, 343, 585
Farrah D. et al., 2012, ApJ, 745, 178
Farrah D. et al., 2013, ApJ, 776, 38
Farrah D. et al., 2016, ApJ, 831, 76
Feruglio C. et al., 2015, A&A, 583, A99
Fischer J. et al., 2010, A&A, 518, L41
Flewelling H. A. et al., 2020, ApJS, 251, 7
Fritz J., Franceschini A., Hatziminaoglou E., 2006, MNRAS, 366, 767
García-Burillo S. et al., 2016, ApJ, 823, L12
González-Alfonso E., Sakamoto K., 2019, ApJ, 882, 153
González-Alfonso E. et al., 2013, A&A, 550, A25
González-Alfonso E. et al., 2017, ApJ, 836, 11
Granato G. L., Danese L., 1994, MNRAS, 268, 235
Hailey-Dunsheath S. et al., 2012, ApJ, 755, 57
Harris K. et al., 2016, MNRAS, 457, 4179
Herrero-Illana R. et al., 2017, MNRAS, 471, 1634
Heymann F., Siebenmorgen R., 2012, ApJ, 751, 27
Hönig S. F., Kishimoto M., 2017, ApJ, 838, L20
Hönig S. F., Beckert T., Ohnaka K., Weigelt G., 2006, A&A, 452, 459
Hönig S. F. et al., 2013, ApJ, 771, 87
Houck J. R., Schneider D. P., Danielson G. E., Beichman C. A., Lonsdale C. J., Neugebauer G., Soifer B. T., 1985, ApJ, 290, L5
Houck J. R. et al., 2004, ApJS, 154, 18
Hughes D. H. et al., 1998, Nature, 394, 241
Johnson S. P., Wilson G. W., Tang Y., Scott K. S., 2013, MNRAS, 436, 2535

Kankare E. et al., 2021, A&A, 649, A134
Kennicutt R. C., Evans N. J., 2012, ARA&A, 50, 531
Klaas U. et al., 2001, A&A, 379, 823
Kollatschny W., Weilbacher P. M., Ochmann M. W., Chelouche D., Monreal-Ibero A., Bacon R., Contini T., 2020, A&A, 633, A79
Kool E. C. et al., 2018, MNRAS, 473, 5641
Kool E. C. et al., 2020, MNRAS, 498, 2167
Krügel E., Siebenmorgen R., 1994, A&A, 282, 407
Lawrence A., 1991, MNRAS, 252, 586
Lebouteiller V., Barry D. J., Spoon H. W. W., Bernard-Salas J., Sloan G. C., Houck J. R., Weedman D. W., 2011, ApJS, 196, 8
Levenson N. A., Sirocky M. M., Hao L., Spoon H. W. W., Marshall J. A., Elitzur M., Houck J. R., 2007, ApJ, 654, L45
Lonsdale C. J., Farrah D., Smith H. E., 2006a, Astrophys. Update, 2, 285
Lonsdale C. J., Diamond P. J., Thrall H., Smith H. E., Lonsdale C. J., 2006b, ApJ, 647, 185
Lonsdale C. J. et al., 2015, ApJ, 813, 45
Lyu J., Rieke G. H., 2021, ApJ, 912, 126
Ma Z., Yan H., 2015, ApJ, 811, 58
Mattila S. et al., 2012, ApJ, 756, 111
Mattila S. et al., 2018, Science, 361, 482
Medling A. M. et al., 2014, ApJ, 784, 70
Nardini E., Risaliti G., Salvati M., Sani E., Watabe Y., Marconi A., Maiolino R., 2009, MNRAS, 399, 1373
Nenkova M., Ivezić Ž., Elitzur M., 2002, ApJ, 570, L9
Nenkova M., Sirocky M. M., Ivezić Ž., Elitzur M., 2008, ApJ, 685, 147
Noll S., Burgarella D., Giovannoli E., Buat V., Marcillac D., Muñoz-Mateos J. C., 2009, A&A, 507, 1793
Oda S., Tanimoto A., Ueda Y., Imanishi M., Terashima Y., Ricci C., 2017, ApJ, 835, 179
Oliver S. J. et al., 2012, MNRAS, 424, 1614
Pearson C. et al., 2016, ApJS, 227, 9
Peeters E., Hony S., Van Kerckhoven C., Tielens A. G. G. M., Allamandola L. J., Hudgins D. M., Bauschlicher C. W., 2002, A&A, 390, 1089
Pereira-Santaella M. et al., 2018, A&A, 616, A171
Pérez-Torres M., Mattila S., Alonso-Herrero A., Aalto S., Efstathiou A., 2021, A&AR, 29, 2
Pier E. A., Krolik J. H., 1993, ApJ, 418, 673
Pilbratt G. L. et al., 2010, A&A, 518, L1
Pitchford L. K. et al., 2016, MNRAS, 462, 4067
Pitchford L. K. et al., 2019, MNRAS, 487, 3130
Privon G. C. et al., 2017, ApJ, 835, 213
Reunanen J., Tacconi-Garman L. E., Ivanov V. D., 2007, MNRAS, 382, 951
Rigopoulou D., Lawrence A., Rowan-Robinson M., 1996, MNRAS, 278, 1049
Rowan-Robinson M., 2000, MNRAS, 316, 885
Rowan-Robinson M., Crawford J., 1989, MNRAS, 238, 523
Rowan-Robinson M., Efstathiou A., 1993, MNRAS, 263, 675
Rowan-Robinson M. et al., 1993, MNRAS, 261, 513
Rowan-Robinson M. et al., 1997, MNRAS, 289, 490
Rowan-Robinson M. et al., 2018, A&A, 619, A169
Ruiz M., Efstathiou A., Alexander D. M., Hough J., 2001, MNRAS, 325, 995
Rupke D. S. N., Veilleux S., 2013, ApJ, 775, L15
Sanders D. B., Mirabel I. F., 1996, ARA&A, 34, 749
Sanders D. B., Mazzarella J. M., Kim D.-C., Surace J. A., Soifer B. T., 2003, AJ, 126, 1607
Saunders W. et al., 2000, MNRAS, 317, 55
Schartmann M., Meisenheimer K., Camenzind M., Wolf S., Tristram K. R. W., Henning T., 2008, A&A, 482, 67
Scoville N. et al., 2017, ApJ, 836, 66
Shirley R. et al., 2019, MNRAS, 490, 634
Shirley R. et al., 2021, MNRAS, 507, 129
Siebenmorgen R., Krügel E., 2007, A&A, 461, 445
Siebenmorgen R., Heymann F., Efstathiou A., 2015, A&A, 583, A120
Silva L., Granato G. L., Bressan A., Danese L., 1998, ApJ, 509, 103
Soifer B. T., Sanders D. B., Neugebauer G., Danielson G. E., Lonsdale C. J., Madore B. F., Persson S. E., 1986, ApJ, 303, L41
Spoon H. W. W., Marshall J. A., Houck J. R., Elitzur M., Hao L., Armus L., Brandl B. R., Charmandaris V., 2007, ApJ, 654, L49
Spoon H. W. W. et al., 2013, ApJ, 775, 127
Stalevski M., Fritz J., Baes M., Nakos T., Popović L. Č., 2012, MNRAS, 420, 2756
Stalevski M., Ricci C., Ueda Y., Lira P., Fritz J., Baes M., 2016, MNRAS, 458, 2288
Sturm E. et al., 2011, ApJ, 733, L16
Tadhunter C., Spence R., Rose M., Mullaney J., Crowther P., 2017, Nat. Astron., 1, 0061
Takagi T., Arimoto N., Hanami H., 2003, MNRAS, 340, 813
Tristram K. R. W. et al., 2007, A&A, 474, 837
U V. et al., 2012, ApJS, 203, 9
Vega O., Clemens M. S., Bressan A., Granato G. L., Silva L., Panuzzo P., 2008, A&A, 484, 631
Veilleux S. et al., 2009, ApJS, 182, 628
Verma A., Rowan-Robinson M., McMahon R., Efstathiou A., 2002, MNRAS, 335, 574
Xu Y., Baloković M., Walton D. J., Harrison F. A., García J. A., Koss M. J., 2017, ApJ, 837, 21
Yamada, S., Ueda Y., Tanimoto A., Imanishi M., Toba Y., Ricci C., Privon G. C., 2021, ApJS, 257, 61
Yan C.-S., Lu Y., Dai X., Yu Q., 2015, ApJ, 809, 117
Young S., Hough J. H., Efstathiou A., Wills B. J., Bailey J. A., Ward M. J., Axon D. J., 1996, MNRAS, 281, 1206

APPENDIX A: INDIVIDUAL SED FITS WITH THE CYGNUS MODELS

The following figures present SED fits using the CYGNUS AGN torus models for all the objects in the sample.

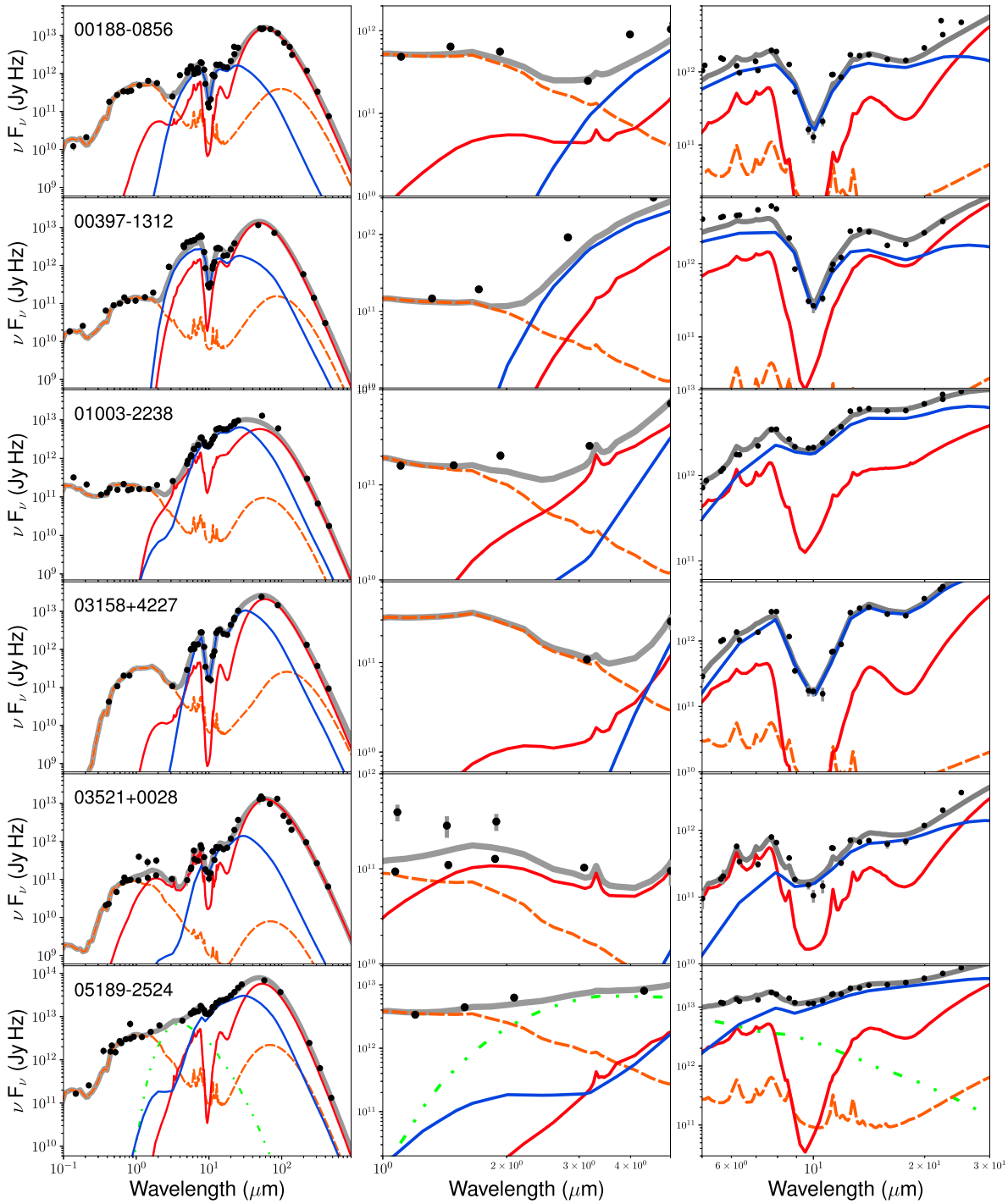

Figure A1. SED fit plots of all objects, using the CYGNUS models: spheroidal host (orange), starburst (red), AGN torus (blue), polar dust (green), and total (grey). These fits assume a single AGN.

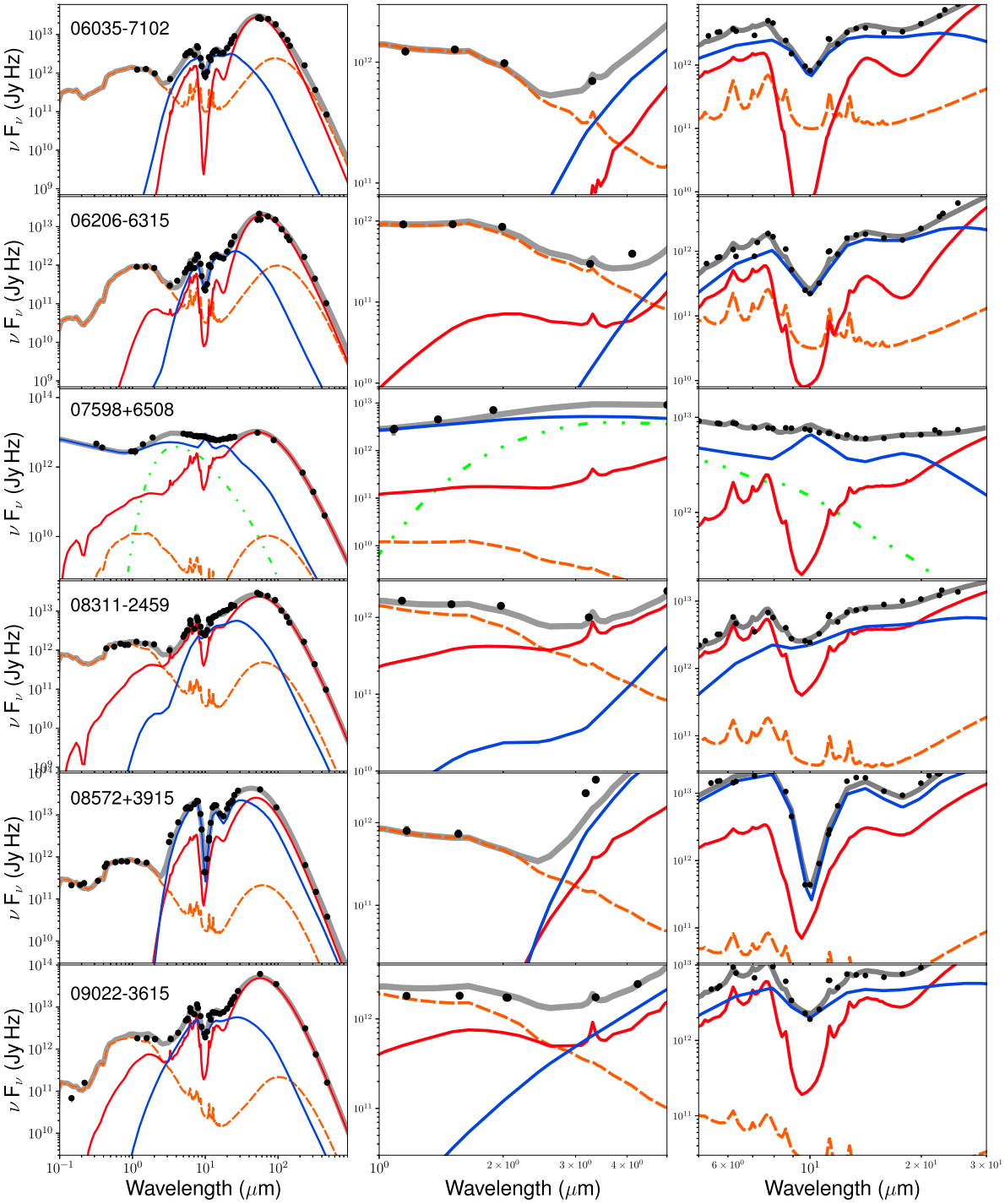

Figure A2. SED fit plots of all objects, using the CYGNUS models.

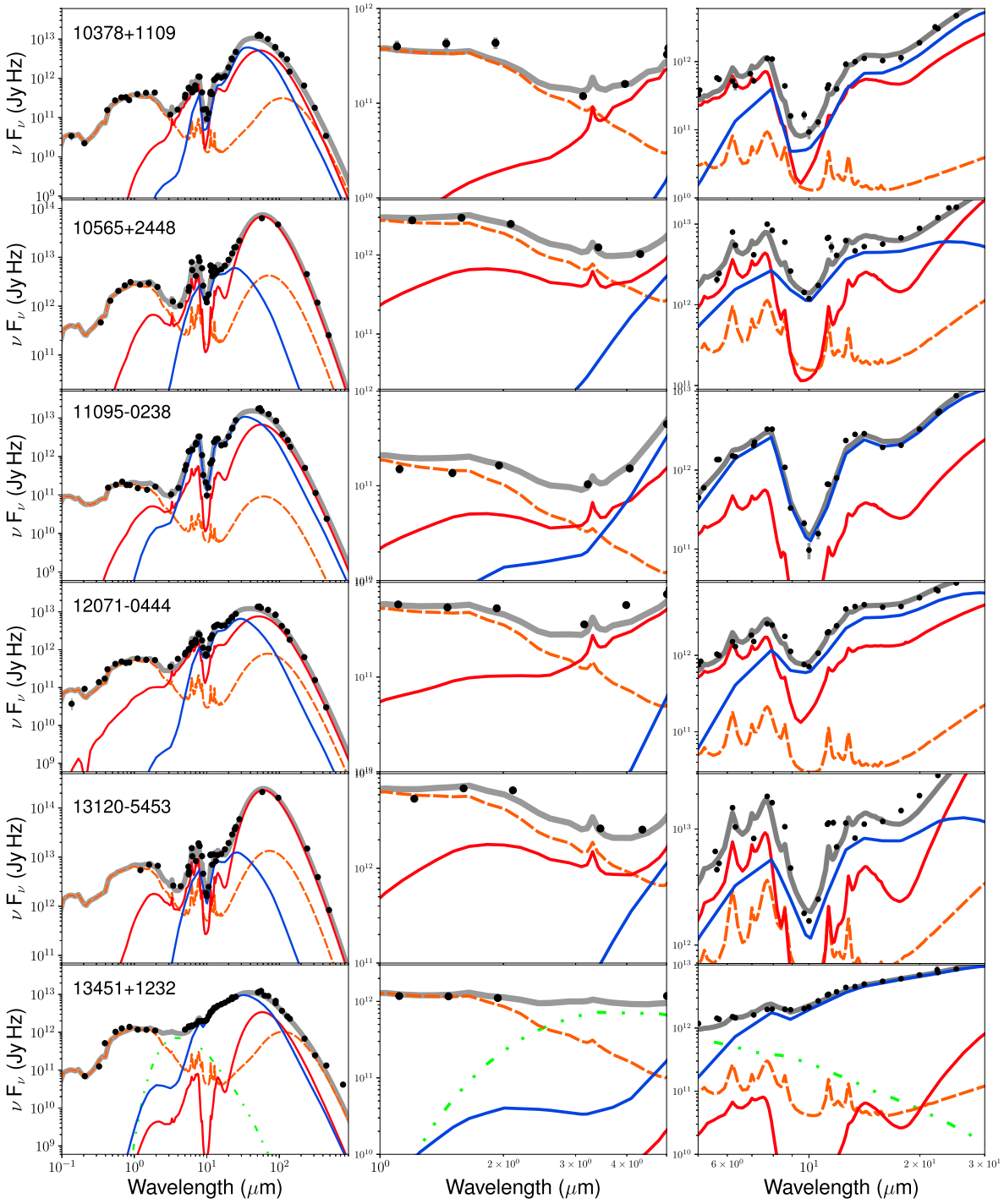

Figure A3. SED fit plots of all objects, using the CYGNUS models.

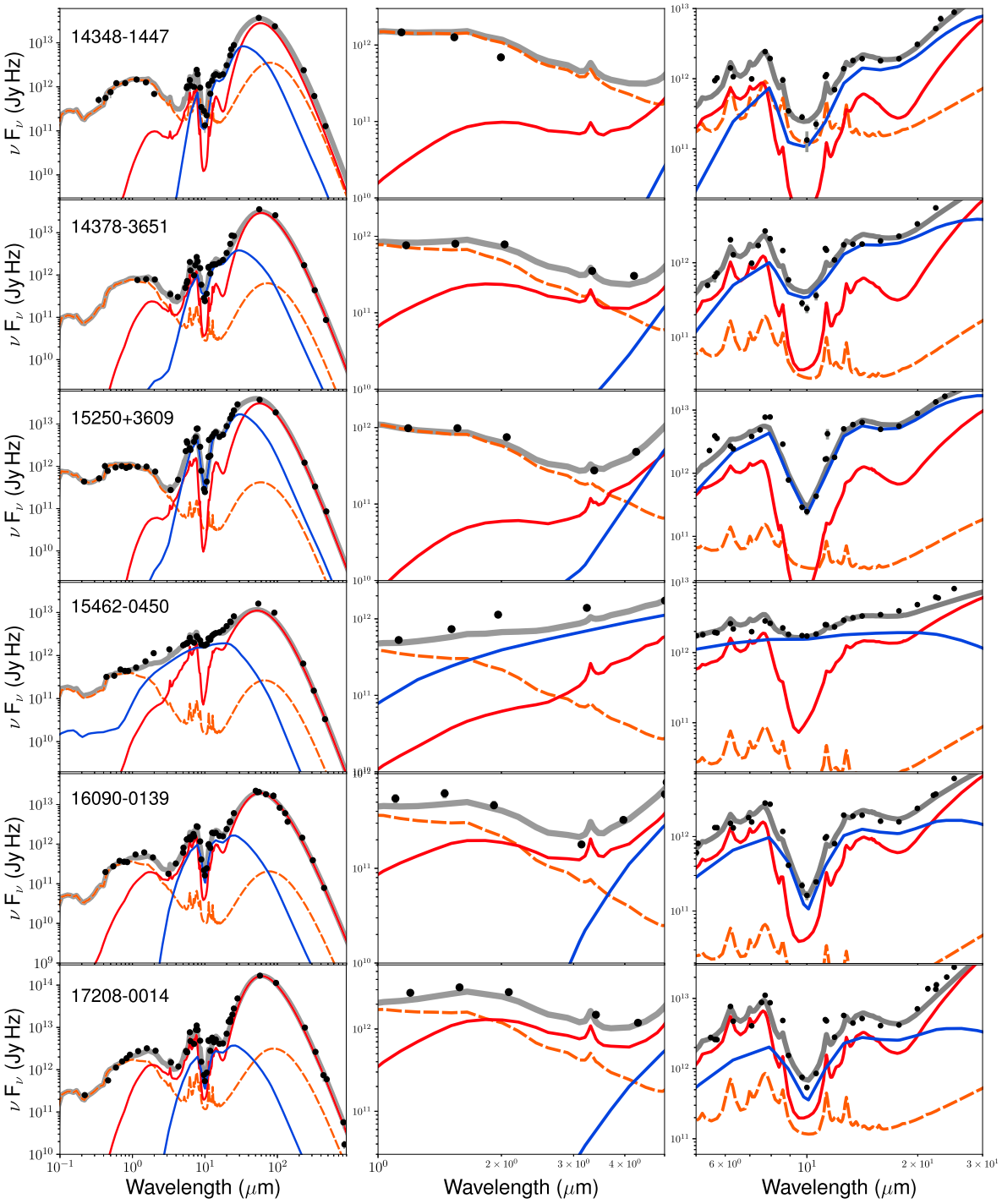

Figure A4. SED fit plots of all objects, using the CYGNUS models.

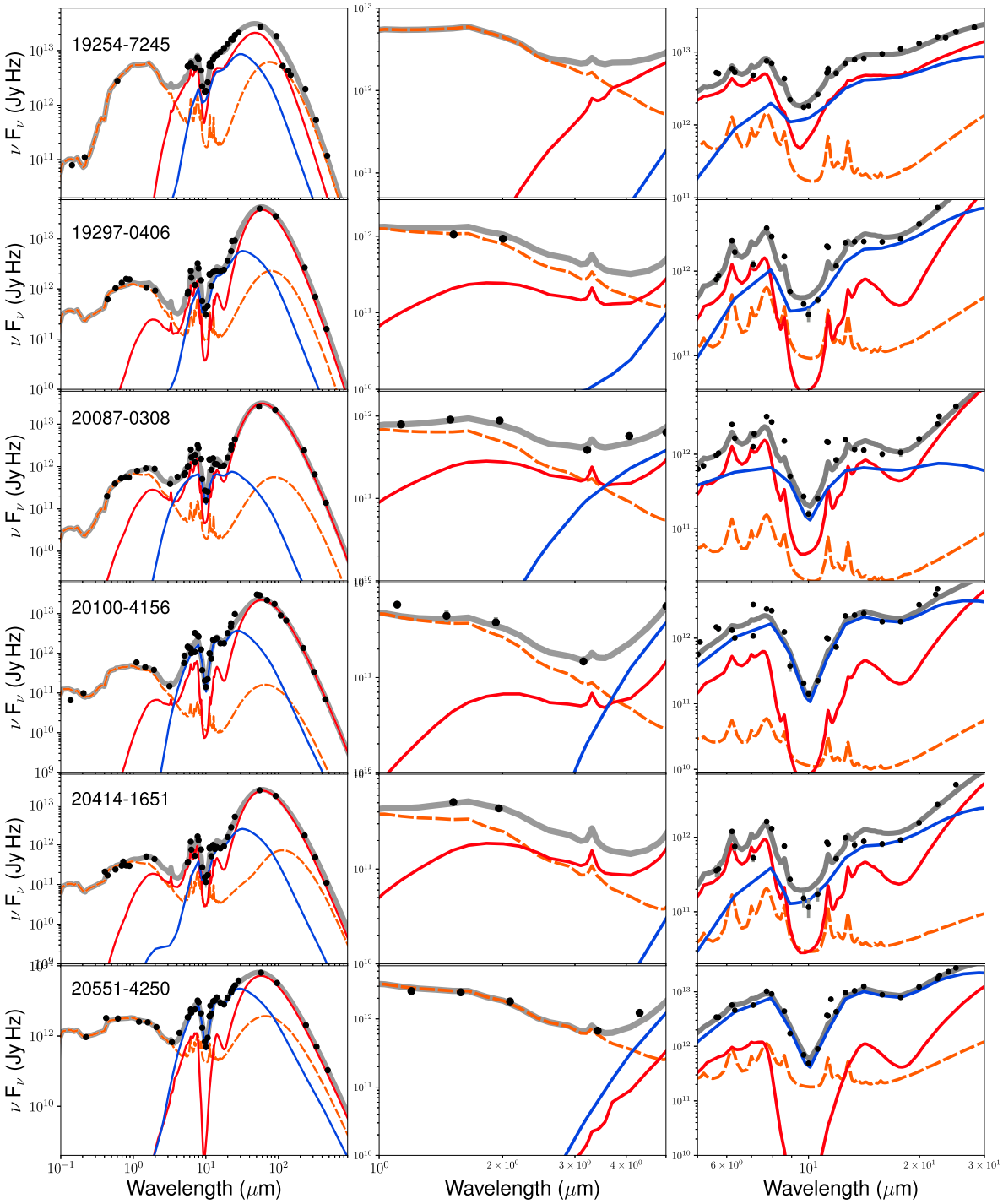

Figure A5. SED fit plots of all objects, using the CYGNUS models.

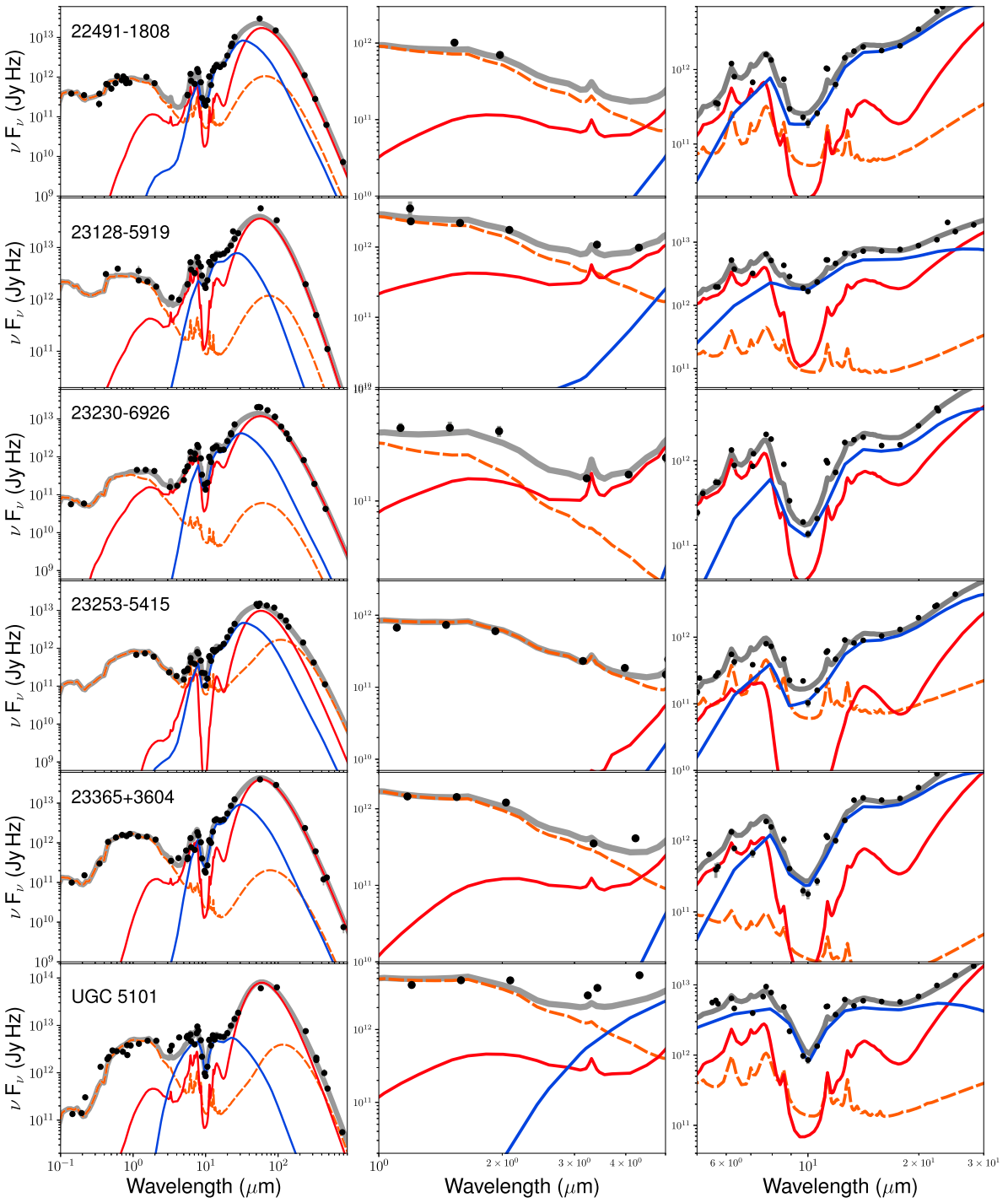

Figure A6. SED fit plots of all objects, using the CYGNUS models.

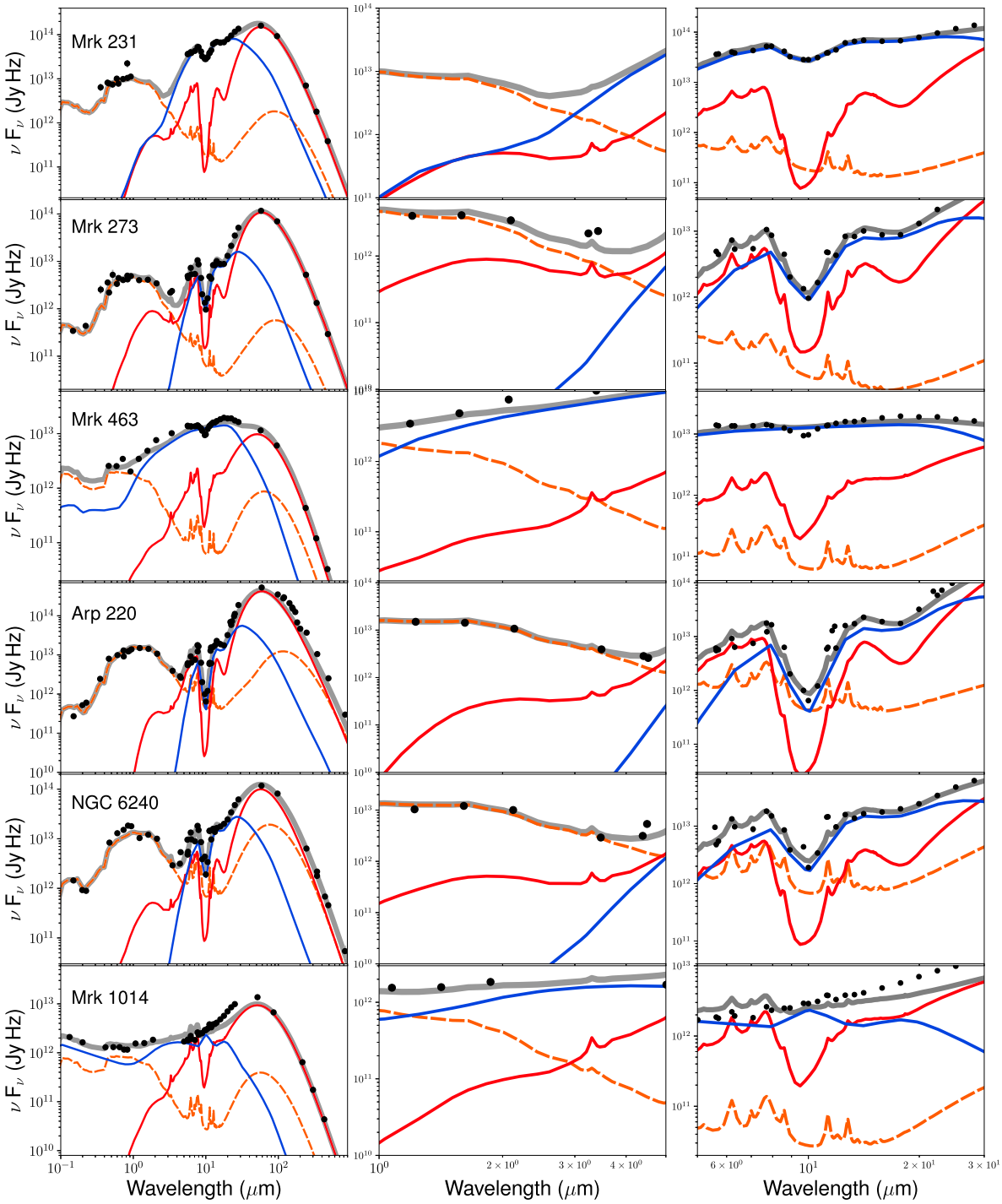

Figure A7. SED fit plots of all objects, using the CYGNUS models.

APPENDIX B: ANCILLARY DATA

The following tables present the full suite of luminosities together with luminosities from the literature. Where appropriate, the luminosities have been scaled to our adopted cosmology.

Table B1. Comparison of luminosities from the literature. Also, the AGN, starburst, spheroidal, and total bolometric luminosities, derived from the CYGNUS model fits. For the AGN and total luminosities, both the observed and anisotropy-corrected luminosities are given.

	Other luminosities				CYGNUS bolometric luminosities					
ID	$L_{\rm Tot}$ SM96	$L_{\rm Tot}$ K01	$L_{\rm AGN}$ N09	$L^{\rm Bol}_{\rm AGN}$ V09	$L^{\rm o}_{\rm AGN}$	$L^{\rm c}_{\rm AGN}$	$L_{\rm Sb}$	$L_{\rm host}$	$L^{\rm o}_{\rm Tot}$	$L^{\rm c}_{\rm Tot}$
	10^{12} L$_\odot$				10^{12} L$_\odot$			10^{11} L$_\odot$	10^{12} L$_\odot$	
1	2.95	—	0.79	1.11	$0.28^{+0.03}_{-0.05}$	$1.21^{+0.22}_{-0.27}$	$1.86^{+0.03}_{-0.02}$	$1.43^{+0.16}_{-0.27}$	$2.29^{+0.05}_{-0.06}$	$3.21^{+0.22}_{-0.29}$
2	9.33	—	5.08	3.92	$2.10^{+0.55}_{-0.31}$	$47.79^{+22.09}_{-10.94}$	$7.14^{+0.18}_{-0.35}$	$2.13^{+0.56}_{-0.60}$	$9.46^{+0.34}_{-0.25}$	$55.15^{+21.78}_{-10.77}$
3	1.78	—	0.80	1.26	$0.81^{+0.22}_{-0.09}$	$1.83^{+0.22}_{-0.25}$	$0.77^{+0.02}_{-0.12}$	$0.58^{+0.13}_{-0.08}$	$1.63^{+0.12}_{-0.08}$	$2.65^{+0.18}_{-0.27}$
4	3.55	2.85	1.92	−0.00	$1.39^{+0.18}_{-0.23}$	$7.62^{+1.08}_{-1.66}$	$2.63^{+0.10}_{-0.06}$	$0.97^{+0.11}_{-0.11}$	$4.11^{+0.13}_{-0.15}$	$10.34^{+1.02}_{-1.57}$
5	3.63	—	0.00	0.96	$0.26^{+0.04}_{-0.03}$	$1.31^{+0.33}_{-0.34}$	$2.16^{+0.03}_{-0.02}$	$0.22^{+0.04}_{-0.02}$	$2.44^{+0.03}_{-0.03}$	$3.49^{+0.31}_{-0.33}$
6	1.32	1.14	0.42	1.18	$0.55^{+0.08}_{-0.06}$	$4.71^{+0.60}_{-0.58}$	$0.77^{+0.07}_{-0.08}$	$1.00^{+0.34}_{-0.21}$	$1.42^{+0.07}_{-0.05}$	$5.58^{+0.58}_{-0.53}$
7	1.38	1.38	0.35	−0.00	$0.21^{+0.09}_{-0.03}$	$0.48^{+2.11}_{-0.10}$	$1.21^{+0.03}_{-0.09}$	$2.41^{+0.20}_{-0.96}$	$1.66^{+0.03}_{-0.10}$	$1.93^{+1.98}_{-0.10}$
8	1.70	1.38	0.09	−0.00	$0.17^{+0.02}_{-0.02}$	$0.54^{+0.13}_{-0.09}$	$1.18^{+0.01}_{-0.03}$	$1.52^{+0.30}_{-0.14}$	$1.51^{+0.02}_{-0.03}$	$1.88^{+0.12}_{-0.10}$
9	2.88	—	3.54	2.86	$3.72^{+0.33}_{-0.37}$	$1.96^{+0.21}_{-0.20}$	$2.19^{+0.01}_{-0.06}$	$0.05^{+0.04}_{-0.01}$	$5.92^{+0.33}_{-0.37}$	$4.16^{+0.21}_{-0.22}$
10	2.88	—	—	−0.00	$0.56^{+0.07}_{-0.08}$	$2.51^{+0.32}_{-0.30}$	$2.27^{+0.02}_{-0.06}$	$2.40^{+0.39}_{-0.21}$	$3.07^{+0.06}_{-0.09}$	$5.02^{+0.30}_{-0.28}$
11	1.45	—	1.26	1.19	$0.78^{+0.15}_{-0.11}$	$23.39^{+9.73}_{-4.27}$	$0.66^{+0.05}_{-0.09}$	$0.41^{+0.11}_{-0.03}$	$1.49^{+0.08}_{-0.05}$	$24.09^{+9.69}_{-4.24}$
12	1.74	—	0.15	−0.00	$0.26^{+0.03}_{-0.02}$	$3.80^{+0.68}_{-0.48}$	$1.42^{+0.01}_{-0.02}$	$0.74^{+0.11}_{-0.09}$	$1.75^{+0.03}_{-0.03}$	$5.29^{+0.68}_{-0.48}$
13	2.40	—	0.24	0.83	$0.83^{+0.12}_{-0.14}$	$20.04^{+13.56}_{-7.75}$	$0.81^{+0.12}_{-0.13}$	$1.27^{+0.49}_{-0.38}$	$1.77^{+0.04}_{-0.06}$	$20.98^{+13.47}_{-7.69}$
14	1.20	—	—	0.21	$0.09^{+0.02}_{-0.01}$	$0.22^{+0.05}_{-0.01}$	$0.93^{+0.02}_{-0.01}$	$1.21^{+0.16}_{-0.14}$	$1.14^{+0.02}_{-0.01}$	$1.27^{+0.05}_{-0.01}$
15	1.91	—	0.93	0.86	$0.94^{+0.12}_{-0.10}$	$29.55^{+14.51}_{-6.45}$	$0.59^{+0.07}_{-0.10}$	$0.38^{+0.07}_{-0.05}$	$1.57^{+0.03}_{-0.04}$	$30.18^{+14.42}_{-6.38}$
16	2.04	—	0.90	1.84	$0.84^{+0.18}_{-0.10}$	$3.34^{+1.53}_{-0.43}$	$1.19^{+0.06}_{-0.18}$	$2.12^{+0.58}_{-0.42}$	$2.25^{+0.06}_{-0.09}$	$4.74^{+1.42}_{-0.41}$
17	1.66	—	0.00	−0.00	$0.10^{+0.02}_{-0.01}$	$0.28^{+0.18}_{-0.05}$	$1.52^{+0.02}_{-0.02}$	$1.78^{+0.23}_{-0.33}$	$1.80^{+0.02}_{-0.02}$	$1.97^{+0.17}_{-0.06}$
18	2.09	—	1.15	1.31	$1.33^{+0.25}_{-0.22}$	$15.48^{+2.61}_{-2.60}$	$0.35^{+0.10}_{-0.12}$	$3.33^{+0.76}_{-0.74}$	$2.01^{+0.20}_{-0.19}$	$16.16^{+2.58}_{-2.57}$
19	2.14	1.62	0.08	0.46	$0.39^{+0.04}_{-0.14}$	$3.69^{+0.35}_{-1.77}$	$1.33^{+0.12}_{-0.01}$	$3.28^{+0.13}_{-0.73}$	$2.05^{+0.02}_{-0.09}$	$5.34^{+0.33}_{-1.72}$
20	1.38	1.03	0.01	−0.00	$0.14^{+0.01}_{-0.01}$	$0.81^{+0.16}_{-0.13}$	$0.95^{+0.01}_{-0.01}$	$0.63^{+0.14}_{-0.10}$	$1.15^{+0.02}_{-0.02}$	$1.83^{+0.16}_{-0.13}$
21	1.07	0.90	0.54	0.59	$0.37^{+0.04}_{-0.05}$	$4.62^{+0.90}_{-0.78}$	$0.66^{+0.03}_{-0.02}$	$0.59^{+0.05}_{-0.07}$	$1.09^{+0.04}_{-0.04}$	$5.34^{+0.87}_{-0.76}$
22	1.74	1.46	0.33	0.78	$0.25^{+0.05}_{-0.04}$	$0.30^{+0.06}_{-0.04}$	$0.96^{+0.09}_{-0.04}$	$0.74^{+0.79}_{-0.16}$	$1.29^{+0.13}_{-0.06}$	$1.34^{+0.14}_{-0.06}$
23	3.47	3.06	0.72	1.34	$0.26^{+0.07}_{-0.05}$	$0.87^{+0.30}_{-0.18}$	$2.69^{+0.09}_{-0.11}$	$1.03^{+0.27}_{-0.19}$	$3.06^{+0.06}_{-0.07}$	$3.67^{+0.21}_{-0.13}$
24	2.40	1.80	0.00	0.34	$0.06^{+0.02}_{-0.01}$	$0.16^{+0.10}_{-0.03}$	$2.10^{+0.01}_{-0.02}$	$0.85^{+0.33}_{-0.13}$	$2.24^{+0.03}_{-0.01}$	$2.34^{+0.10}_{-0.03}$
25	1.15	1.01	0.32	−0.00	$0.28^{+0.20}_{-0.04}$	$1.52^{+0.77}_{-0.25}$	$0.71^{+0.04}_{-0.14}$	$4.02^{+1.18}_{-0.69}$	$1.39^{+0.17}_{-0.05}$	$2.63^{+0.73}_{-0.26}$
26	2.40	—	0.03	−0.00	$0.34^{+0.17}_{-0.05}$	$4.24^{+13.24}_{-1.32}$	$1.96^{+0.07}_{-0.13}$	$2.61^{+0.85}_{-0.59}$	$2.57^{+0.09}_{-0.05}$	$6.46^{+13.13}_{-1.31}$
27	2.57	2.08	0.08	−0.00	$0.10^{+0.03}_{-0.03}$	$0.37^{+0.24}_{-0.18}$	$2.52^{+0.07}_{-0.02}$	$1.31^{+0.31}_{-0.75}$	$2.75^{+0.08}_{-0.06}$	$3.02^{+0.23}_{-0.17}$
28	4.27	3.07	0.64	−0.00	$0.52^{+0.08}_{-0.10}$	$2.51^{+0.52}_{-0.96}$	$2.63^{+0.06}_{-0.09}$	$1.18^{+0.37}_{-0.20}$	$3.26^{+0.10}_{-0.13}$	$5.25^{+0.53}_{-0.98}$
29	1.74	1.31	0.00	0.24	$0.15^{+0.03}_{-0.04}$	$1.49^{+0.51}_{-0.79}$	$1.25^{+0.02}_{-0.02}$	$0.85^{+0.38}_{-0.15}$	$1.48^{+0.03}_{-0.03}$	$2.82^{+0.50}_{-0.78}$
30	1.02	0.86	0.26	−0.00	$0.31^{+0.06}_{-0.03}$	$1.59^{+0.37}_{-0.18}$	$0.62^{+0.02}_{-0.03}$	$1.37^{+0.30}_{-0.27}$	$1.07^{+0.06}_{-0.03}$	$2.35^{+0.36}_{-0.18}$
31	1.51	1.11	0.00	0.32	$0.36^{+0.03}_{-0.06}$	$5.82^{+1.42}_{-1.71}$	$0.74^{+0.04}_{-0.02}$	$1.30^{+0.19}_{-0.28}$	$1.22^{+0.02}_{-0.04}$	$6.69^{+1.41}_{-1.71}$
32	1.15	0.90	0.03	−0.00	$0.13^{+0.01}_{-0.02}$	$0.37^{+0.04}_{-0.06}$	$0.56^{+0.01}_{-0.01}$	$1.04^{+0.13}_{-0.24}$	$0.80^{+0.03}_{-0.04}$	$1.04^{+0.05}_{-0.07}$
33	2.09	1.67	0.09	−0.00	$0.34^{+0.05}_{-0.04}$	$1.57^{+0.43}_{-0.14}$	$1.08^{+0.01}_{-0.03}$	$0.49^{+0.10}_{-0.09}$	$1.47^{+0.04}_{-0.04}$	$2.70^{+0.42}_{-0.13}$
34	1.82	—	0.15	−0.00	$0.57^{+0.12}_{-0.17}$	$6.40^{+3.64}_{-3.42}$	$1.12^{+0.14}_{-0.08}$	$4.22^{+0.88}_{-0.96}$	$2.12^{+0.10}_{-0.10}$	$7.94^{+3.62}_{-3.33}$
35	1.48	1.15	0.11	−0.00	$0.26^{+0.07}_{-0.03}$	$1.57^{+1.21}_{-0.42}$	$1.14^{+0.01}_{-0.04}$	$0.77^{+0.10}_{-0.06}$	$1.48^{+0.05}_{-0.03}$	$2.79^{+1.18}_{-0.41}$
36	1.02	—	0.14	0.39	$0.09^{+0.02}_{-0.01}$	$0.36^{+0.17}_{-0.11}$	$0.85^{+0.03}_{-0.01}$	$1.26^{+0.18}_{-0.12}$	$1.06^{+0.04}_{-0.02}$	$1.33^{+0.18}_{-0.11}$
37	3.09	2.86	1.18	2.82	$1.46^{+0.17}_{-0.13}$	$5.98^{+0.70}_{-0.50}$	$1.89^{+0.14}_{-0.12}$	$2.30^{+0.38}_{-0.27}$	$3.59^{+0.22}_{-0.13}$	$8.10^{+0.73}_{-0.52}$
38	1.35	1.16	0.10	0.80	$0.17^{+0.04}_{-0.03}$	$0.78^{+0.67}_{-0.32}$	$1.09^{+0.03}_{-0.02}$	$0.73^{+0.13}_{-0.08}$	$1.34^{+0.04}_{-0.03}$	$1.94^{+0.68}_{-0.31}$
39	0.59	0.56	—	−0.00	$0.52^{+0.07}_{-0.05}$	$0.52^{+0.10}_{-0.05}$	$0.23^{+0.02}_{-0.02}$	$0.96^{+0.23}_{-0.46}$	$0.84^{+0.07}_{-0.07}$	$0.84^{+0.10}_{-0.07}$
40	1.38	1.26	0.28	0.34	$0.12^{+0.08}_{-0.01}$	$0.97^{+1.49}_{-0.15}$	$0.90^{+0.01}_{-0.03}$	$0.83^{+0.17}_{-0.05}$	$1.10^{+0.07}_{-0.01}$	$1.95^{+1.48}_{-0.15}$
41	0.85	0.61	0.05	0.21	$0.12^{+0.02}_{-0.03}$	$0.47^{+0.06}_{-0.19}$	$0.42^{+0.04}_{-0.03}$	$1.78^{+0.49}_{-0.58}$	$0.72^{+0.03}_{-0.04}$	$1.07^{+0.06}_{-0.20}$
42	4.07	—	0.92	3.56	$1.29^{+0.20}_{-0.15}$	$0.57^{+0.10}_{-0.08}$	$2.44^{+0.07}_{-0.05}$	$4.55^{+1.04}_{-1.39}$	$4.18^{+0.18}_{-0.15}$	$3.46^{+0.10}_{-0.10}$

Table B2. Infrared and bolometric luminosities from the FR06 model fits.

ID	Infrared luminosities					Bolometric luminosities				
	$L_{\rm Sb}$	$L^{\rm o}_{\rm AGN}$ 10^{12} L$_\odot$	$L^{\rm c}_{\rm AGN}$	$L_{\rm host}$ 10^{11} L$_\odot$	$L^{\rm c}_{\rm Tot}$ 10^{12} L$_\odot$	$L_{\rm Sb}$	$L^{\rm o}_{\rm AGN}$ 10^{12} L$_\odot$	$L^{\rm c}_{\rm AGN}$	$L_{\rm host}$ 10^{11} L$_\odot$	$L^{\rm c}_{\rm Tot}$ 10^{12} L$_\odot$
1	$1.53^{+0.07}_{-0.03}$	$0.48^{+0.11}_{-0.09}$	$0.86^{+0.21}_{-0.14}$	$1.42^{+0.45}_{-0.34}$	$2.54^{+0.24}_{-0.14}$	$1.53^{+0.07}_{-0.03}$	$0.48^{+0.11}_{-0.09}$	$1.23^{+0.36}_{-0.21}$	$1.76^{+0.53}_{-0.37}$	$2.93^{+0.39}_{-0.18}$
2	$4.12^{+0.39}_{-0.28}$	$3.99^{+0.76}_{-0.79}$	$13.86^{+2.11}_{-2.60}$	$3.06^{+0.61}_{-0.84}$	$18.28^{+1.90}_{-2.29}$	$4.12^{+0.39}_{-0.28}$	$3.99^{+0.76}_{-0.79}$	$43.96^{+6.28}_{-7.96}$	$3.68^{+0.75}_{-0.92}$	$48.45^{+6.21}_{-7.67}$
3	$0.73^{+0.04}_{-0.03}$	$0.79^{+0.16}_{-0.19}$	$1.55^{+0.35}_{-0.38}$	$0.22^{+0.04}_{-0.05}$	$2.29^{+0.32}_{-0.35}$	$0.73^{+0.04}_{-0.03}$	$0.79^{+0.16}_{-0.19}$	$1.90^{+0.44}_{-0.47}$	$0.56^{+0.11}_{-0.13}$	$2.68^{+0.42}_{-0.45}$
4	$3.66^{+0.08}_{-0.01}$	$0.79^{+0.07}_{-0.11}$	$1.47^{+0.12}_{-0.19}$	$0.62^{+0.03}_{-0.16}$	$5.19^{+0.15}_{-0.18}$	$3.66^{+0.08}_{-0.01}$	$0.79^{+0.07}_{-0.11}$	$1.74^{+0.15}_{-0.22}$	$0.81^{+0.04}_{-0.17}$	$5.49^{+0.18}_{-0.21}$
5	$1.88^{+0.03}_{-0.02}$	$0.18^{+0.04}_{-0.05}$	$0.33^{+0.08}_{-0.09}$	$0.50^{+0.06}_{-0.18}$	$2.26^{+0.07}_{-0.08}$	$1.88^{+0.03}_{-0.02}$	$0.18^{+0.04}_{-0.05}$	$0.40^{+0.11}_{-0.11}$	$0.63^{+0.07}_{-0.20}$	$2.34^{+0.09}_{-0.10}$
6	$0.72^{+0.06}_{-0.00}$	$0.61^{+0.09}_{-0.07}$	$0.72^{+0.11}_{-0.09}$	$0.70^{+0.04}_{-0.39}$	$1.50^{+0.11}_{-0.09}$	$0.72^{+0.06}_{-0.00}$	$0.61^{+0.09}_{-0.07}$	$0.86^{+0.14}_{-0.10}$	$1.02^{+0.07}_{-0.41}$	$1.68^{+0.14}_{-0.10}$
7	$1.03^{+0.17}_{-0.03}$	$0.36^{+0.05}_{-0.06}$	$0.73^{+0.11}_{-0.13}$	$1.90^{+0.29}_{-1.06}$	$1.96^{+0.13}_{-0.08}$	$1.03^{+0.17}_{-0.03}$	$0.36^{+0.05}_{-0.06}$	$1.15^{+0.21}_{-0.23}$	$2.47^{+0.26}_{-0.95}$	$2.43^{+0.23}_{-0.20}$
8	$0.91^{+0.07}_{-0.02}$	$0.24^{+0.04}_{-0.07}$	$0.43^{+0.08}_{-0.11}$	$2.27^{+0.22}_{-0.66}$	$1.57^{+0.09}_{-0.10}$	$0.91^{+0.07}_{-0.02}$	$0.24^{+0.04}_{-0.07}$	$0.51^{+0.10}_{-0.12}$	$2.73^{+0.27}_{-0.73}$	$1.70^{+0.13}_{-0.12}$
9	$1.65^{+0.06}_{-0.05}$	$2.84^{+0.29}_{-0.38}$	$1.62^{+0.19}_{-0.19}$	$0.00^{+0.00}_{-0.00}$	$3.27^{+0.18}_{-0.20}$	$1.66^{+0.06}_{-0.05}$	$4.52^{+0.60}_{-0.89}$	$1.76^{+0.25}_{-0.35}$	$0.00^{+0.00}_{-0.00}$	$3.42^{+0.25}_{-0.36}$
10	$1.42^{+0.12}_{-0.14}$	$1.07^{+0.16}_{-0.15}$	$1.83^{+0.27}_{-0.29}$	$3.12^{+1.34}_{-1.38}$	$3.57^{+0.26}_{-0.30}$	$1.42^{+0.12}_{-0.14}$	$1.07^{+0.16}_{-0.15}$	$2.20^{+0.32}_{-0.34}$	$4.32^{+1.32}_{-1.59}$	$4.06^{+0.31}_{-0.36}$
11	$0.67^{+0.06}_{-0.13}$	$0.89^{+0.12}_{-0.09}$	$3.84^{+0.32}_{-0.52}$	$0.19^{+0.01}_{-0.03}$	$4.54^{+0.24}_{-0.50}$	$0.67^{+0.06}_{-0.13}$	$0.89^{+0.12}_{-0.09}$	$11.58^{+0.85}_{-1.92}$	$0.41^{+0.02}_{-0.06}$	$12.29^{+0.77}_{-1.92}$
12	$1.56^{+0.03}_{-0.02}$	$0.04^{+0.00}_{-0.01}$	$0.05^{+0.00}_{-0.01}$	$0.00^{+0.00}_{-0.00}$	$1.61^{+0.03}_{-0.02}$	$1.57^{+0.03}_{-0.02}$	$0.05^{+0.01}_{-0.01}$	$0.08^{+0.01}_{-0.01}$	$0.00^{+0.00}_{-0.00}$	$1.66^{+0.03}_{-0.02}$
13	$1.07^{+0.13}_{-0.03}$	$0.46^{+0.09}_{-0.09}$	$0.85^{+0.17}_{-0.17}$	$1.65^{+0.34}_{-0.88}$	$2.09^{+0.17}_{-0.16}$	$1.07^{+0.13}_{-0.03}$	$0.46^{+0.09}_{-0.09}$	$1.01^{+0.20}_{-0.20}$	$2.00^{+0.37}_{-0.87}$	$2.29^{+0.21}_{-0.19}$
14	$0.65^{+0.01}_{-0.02}$	$0.01^{+0.01}_{-0.00}$	$0.02^{+0.01}_{-0.00}$	$0.53^{+0.13}_{-0.07}$	$0.72^{+0.01}_{-0.01}$	$0.65^{+0.01}_{-0.02}$	$0.01^{+0.01}_{-0.00}$	$0.03^{+0.01}_{-0.00}$	$0.72^{+0.17}_{-0.08}$	$0.75^{+0.02}_{-0.01}$
15	$1.10^{+0.02}_{-0.02}$	$0.46^{+0.06}_{-0.07}$	$0.88^{+0.12}_{-0.13}$	$0.17^{+0.02}_{-0.04}$	$1.99^{+0.10}_{-0.11}$	$1.10^{+0.02}_{-0.02}$	$0.46^{+0.06}_{-0.07}$	$1.06^{+0.15}_{-0.16}$	$0.42^{+0.05}_{-0.10}$	$2.20^{+0.13}_{-0.14}$
16	$1.00^{+0.13}_{-0.11}$	$0.84^{+0.13}_{-0.22}$	$1.52^{+0.27}_{-0.31}$	$1.56^{+1.59}_{-1.10}$	$2.67^{+0.31}_{-0.27}$	$1.00^{+0.13}_{-0.11}$	$0.84^{+0.13}_{-0.22}$	$1.82^{+0.34}_{-0.35}$	$2.09^{+1.73}_{-1.12}$	$3.03^{+0.40}_{-0.32}$
17	$1.12^{+0.07}_{-0.04}$	$0.14^{+0.06}_{-0.05}$	$0.28^{+0.13}_{-0.12}$	$1.56^{+0.54}_{-0.95}$	$1.56^{+0.14}_{-0.14}$	$1.12^{+0.07}_{-0.04}$	$0.14^{+0.06}_{-0.05}$	$0.35^{+0.18}_{-0.16}$	$1.87^{+0.64}_{-1.07}$	$1.66^{+0.20}_{-0.18}$
18	$0.75^{+0.06}_{-0.06}$	$0.80^{+0.22}_{-0.21}$	$1.21^{+0.32}_{-0.32}$	$2.44^{+0.98}_{-0.50}$	$2.19^{+0.38}_{-0.29}$	$0.75^{+0.06}_{-0.06}$	$0.80^{+0.22}_{-0.22}$	$1.43^{+0.40}_{-0.37}$	$3.36^{+1.23}_{-0.64}$	$2.51^{+0.48}_{-0.36}$
19	$1.65^{+0.08}_{-0.02}$	$0.16^{+0.04}_{-0.10}$	$0.31^{+0.07}_{-0.23}$	$1.06^{+0.27}_{-0.19}$	$2.07^{+0.08}_{-0.17}$	$1.65^{+0.08}_{-0.02}$	$0.16^{+0.04}_{-0.10}$	$0.38^{+0.09}_{-0.27}$	$1.62^{+0.32}_{-0.27}$	$2.19^{+0.10}_{-0.22}$
20	$0.80^{+0.03}_{-0.02}$	$0.13^{+0.03}_{-0.04}$	$0.25^{+0.05}_{-0.07}$	$0.75^{+0.16}_{-0.34}$	$1.12^{+0.04}_{-0.06}$	$0.80^{+0.03}_{-0.02}$	$0.13^{+0.03}_{-0.04}$	$0.30^{+0.07}_{-0.07}$	$0.92^{+0.18}_{-0.35}$	$1.19^{+0.05}_{-0.07}$
21	$0.68^{+0.03}_{-0.01}$	$0.35^{+0.05}_{-0.05}$	$0.65^{+0.09}_{-0.08}$	$0.32^{+0.11}_{-0.10}$	$1.36^{+0.08}_{-0.07}$	$0.68^{+0.03}_{-0.01}$	$0.35^{+0.05}_{-0.05}$	$0.77^{+0.11}_{-0.10}$	$0.63^{+0.10}_{-0.11}$	$1.51^{+0.10}_{-0.08}$
22	$1.05^{+0.03}_{-0.04}$	$0.26^{+0.04}_{-0.04}$	$0.20^{+0.03}_{-0.03}$	$0.23^{+0.05}_{-0.04}$	$1.28^{+0.04}_{-0.06}$	$1.05^{+0.03}_{-0.04}$	$0.27^{+0.04}_{-0.04}$	$0.23^{+0.04}_{-0.04}$	$0.45^{+0.09}_{-0.08}$	$1.33^{+0.04}_{-0.06}$
23	$2.81^{+0.15}_{-0.17}$	$0.33^{+0.19}_{-0.09}$	$0.63^{+0.42}_{-0.17}$	$0.40^{+0.07}_{-0.09}$	$3.48^{+0.28}_{-0.09}$	$2.81^{+0.15}_{-0.17}$	$0.33^{+0.19}_{-0.09}$	$0.78^{+0.65}_{-0.21}$	$0.84^{+0.12}_{-0.20}$	$3.67^{+0.50}_{-0.12}$
24	$2.33^{+0.01}_{-0.01}$	$0.05^{+0.02}_{-0.01}$	$0.08^{+0.04}_{-0.02}$	$0.60^{+0.09}_{-0.15}$	$2.47^{+0.04}_{-0.02}$	$2.33^{+0.01}_{-0.01}$	$0.05^{+0.02}_{-0.01}$	$0.12^{+0.06}_{-0.04}$	$0.74^{+0.12}_{-0.15}$	$2.53^{+0.06}_{-0.03}$
25	$0.32^{+0.07}_{-0.11}$	$0.63^{+0.15}_{-0.11}$	$1.10^{+0.25}_{-0.17}$	$2.57^{+1.21}_{-0.80}$	$1.68^{+0.26}_{-0.16}$	$0.32^{+0.07}_{-0.11}$	$0.63^{+0.15}_{-0.11}$	$1.32^{+0.30}_{-0.20}$	$3.27^{+1.41}_{-0.91}$	$1.96^{+0.34}_{-0.20}$
26	$2.20^{+0.01}_{-0.01}$	$0.28^{+0.06}_{-0.04}$	$0.48^{+0.10}_{-0.07}$	$0.49^{+0.09}_{-0.10}$	$2.73^{+0.09}_{-0.07}$	$2.20^{+0.01}_{-0.01}$	$0.28^{+0.06}_{-0.04}$	$0.57^{+0.12}_{-0.09}$	$1.03^{+0.21}_{-0.26}$	$2.87^{+0.12}_{-0.09}$
27	$1.65^{+0.11}_{-0.08}$	$0.02^{+0.01}_{-0.00}$	$0.01^{+0.05}_{-0.00}$	$1.88^{+0.62}_{-0.52}$	$1.85^{+0.18}_{-0.10}$	$1.65^{+0.11}_{-0.08}$	$0.02^{+0.01}_{-0.00}$	$0.01^{+0.10}_{-0.00}$	$2.25^{+0.75}_{-0.58}$	$1.89^{+0.25}_{-0.10}$
28	$2.72^{+0.10}_{-0.08}$	$0.84^{+0.13}_{-0.17}$	$1.55^{+0.24}_{-0.30}$	$2.17^{+0.64}_{-0.49}$	$4.49^{+0.23}_{-0.23}$	$2.72^{+0.10}_{-0.08}$	$0.84^{+0.13}_{-0.17}$	$1.84^{+0.29}_{-0.35}$	$2.66^{+0.75}_{-0.47}$	$4.83^{+0.28}_{-0.28}$
29	$1.63^{+0.03}_{-0.02}$	$0.05^{+0.01}_{-0.02}$	$0.05^{+0.01}_{-0.01}$	$0.14^{+0.03}_{-0.02}$	$1.69^{+0.03}_{-0.02}$	$1.63^{+0.03}_{-0.02}$	$0.05^{+0.01}_{-0.02}$	$0.06^{+0.03}_{-0.02}$	$0.26^{+0.06}_{-0.04}$	$1.72^{+0.04}_{-0.02}$
30	$0.55^{+0.01}_{-0.03}$	$0.37^{+0.03}_{-0.05}$	$0.67^{+0.06}_{-0.08}$	$0.36^{+0.08}_{-0.03}$	$1.26^{+0.05}_{-0.09}$	$0.55^{+0.01}_{-0.03}$	$0.37^{+0.03}_{-0.05}$	$0.80^{+0.07}_{-0.10}$	$0.84^{+0.14}_{-0.08}$	$1.43^{+0.07}_{-0.11}$
31	$0.73^{+0.02}_{-0.01}$	$0.18^{+0.03}_{-0.04}$	$0.32^{+0.05}_{-0.06}$	$0.92^{+0.12}_{-0.27}$	$1.14^{+0.05}_{-0.06}$	$0.73^{+0.02}_{-0.01}$	$0.18^{+0.03}_{-0.04}$	$0.38^{+0.07}_{-0.07}$	$1.41^{+0.13}_{-0.32}$	$1.25^{+0.06}_{-0.07}$
32	$0.56^{+0.02}_{-0.04}$	$0.15^{+0.02}_{-0.04}$	$0.31^{+0.04}_{-0.06}$	$0.86^{+0.38}_{-0.16}$	$0.95^{+0.04}_{-0.06}$	$0.56^{+0.02}_{-0.04}$	$0.15^{+0.02}_{-0.04}$	$0.38^{+0.05}_{-0.08}$	$1.36^{+0.29}_{-0.19}$	$1.07^{+0.05}_{-0.08}$
33	$1.16^{+0.03}_{-0.02}$	$0.24^{+0.06}_{-0.04}$	$0.47^{+0.12}_{-0.07}$	$0.91^{+0.17}_{-0.29}$	$1.72^{+0.10}_{-0.06}$	$1.16^{+0.03}_{-0.02}$	$0.24^{+0.06}_{-0.04}$	$0.57^{+0.14}_{-0.08}$	$1.15^{+0.20}_{-0.32}$	$1.85^{+0.14}_{-0.07}$
34	$1.14^{+0.09}_{-0.07}$	$0.24^{+0.09}_{-0.10}$	$0.45^{+0.15}_{-0.20}$	$2.85^{+0.73}_{-1.29}$	$1.88^{+0.14}_{-0.25}$	$1.14^{+0.09}_{-0.07}$	$0.24^{+0.09}_{-0.10}$	$0.54^{+0.17}_{-0.24}$	$3.51^{+0.83}_{-1.40}$	$2.04^{+0.17}_{-0.31}$
35	$1.04^{+0.01}_{-0.03}$	$0.13^{+0.03}_{-0.03}$	$0.25^{+0.06}_{-0.06}$	$0.37^{+0.32}_{-0.04}$	$1.32^{+0.07}_{-0.05}$	$1.04^{+0.01}_{-0.03}$	$0.13^{+0.03}_{-0.03}$	$0.30^{+0.08}_{-0.07}$	$0.73^{+0.32}_{-0.08}$	$1.41^{+0.08}_{-0.06}$
36	$0.72^{+0.01}_{-0.01}$	$0.06^{+0.01}_{-0.01}$	$0.08^{+0.02}_{-0.01}$	$1.05^{+0.15}_{-0.08}$	$0.90^{+0.02}_{-0.01}$	$0.72^{+0.01}_{-0.01}$	$0.06^{+0.01}_{-0.01}$	$0.10^{+0.02}_{-0.01}$	$1.32^{+0.18}_{-0.10}$	$0.95^{+0.03}_{-0.01}$
37	$1.65^{+0.04}_{-0.03}$	$1.64^{+0.18}_{-0.16}$	$2.57^{+0.28}_{-0.25}$	$1.95^{+0.36}_{-0.19}$	$4.41^{+0.27}_{-0.23}$	$1.65^{+0.04}_{-0.03}$	$1.64^{+0.18}_{-0.16}$	$3.09^{+0.35}_{-0.28}$	$3.11^{+0.55}_{-0.31}$	$5.05^{+0.36}_{-0.27}$
38	$0.95^{+0.02}_{-0.04}$	$0.24^{+0.04}_{-0.03}$	$0.43^{+0.09}_{-0.06}$	$1.09^{+0.44}_{-0.14}$	$1.49^{+0.09}_{-0.06}$	$0.95^{+0.02}_{-0.04}$	$0.24^{+0.04}_{-0.03}$	$0.51^{+0.11}_{-0.07}$	$1.42^{+0.45}_{-0.16}$	$1.60^{+0.11}_{-0.07}$
39	$0.15^{+0.02}_{-0.03}$	$0.57^{+0.05}_{-0.05}$	$0.52^{+0.05}_{-0.04}$	$0.87^{+0.12}_{-0.14}$	$0.76^{+0.03}_{-0.04}$	$0.15^{+0.02}_{-0.03}$	$0.57^{+0.05}_{-0.05}$	$0.71^{+0.10}_{-0.07}$	$1.31^{+0.16}_{-0.16}$	$0.99^{+0.09}_{-0.07}$
40	$0.97^{+0.01}_{-0.00}$	$0.01^{+0.00}_{-0.00}$	$0.03^{+0.01}_{-0.00}$	$0.82^{+0.12}_{-0.06}$	$1.09^{+0.02}_{-0.00}$	$0.97^{+0.01}_{-0.00}$	$0.01^{+0.00}_{-0.00}$	$0.06^{+0.02}_{-0.01}$	$1.00^{+0.15}_{-0.08}$	$1.14^{+0.03}_{-0.01}$
41	$0.35^{+0.02}_{-0.02}$	$0.16^{+0.03}_{-0.03}$	$0.31^{+0.07}_{-0.05}$	$1.65^{+0.31}_{-0.25}$	$0.82^{+0.08}_{-0.05}$	$0.35^{+0.02}_{-0.02}$	$0.16^{+0.03}_{-0.03}$	$0.38^{+0.09}_{-0.06}$	$2.02^{+0.38}_{-0.29}$	$0.93^{+0.10}_{-0.07}$
42	$2.88^{+0.03}_{-0.05}$	$0.66^{+0.09}_{-0.05}$	$0.62^{+0.08}_{-0.05}$	$0.75^{+0.42}_{-0.40}$	$3.57^{+0.07}_{-0.06}$	$2.88^{+0.03}_{-0.05}$	$1.41^{+0.18}_{-0.13}$	$0.82^{+0.10}_{-0.08}$	$1.83^{+0.91}_{-0.98}$	$3.88^{+0.09}_{-0.09}$

Table B3. Infrared and bolometric luminosities from the SKIRTOR model fits.

ID	Infrared luminosities					Bolometric luminosities				
	$L_{\rm Sb}$	$L^{\rm o}_{\rm AGN}$ 10^{12} L$_\odot$	$L^{\rm c}_{\rm AGN}$	$L_{\rm host}$ 10^{11} L$_\odot$	$L^{\rm c}_{\rm Tot}$ 10^{12} L$_\odot$	$L_{\rm Sb}$	$L^{\rm o}_{\rm AGN}$ 10^{12} L$_\odot$	$L^{\rm c}_{\rm AGN}$	$L_{\rm host}$ 10^{11} L$_\odot$	$L^{\rm c}_{\rm Tot}$ 10^{12} L$_\odot$
1	$1.48^{+0.07}_{-0.03}$	$0.05^{+0.02}_{-0.03}$	$0.09^{+0.05}_{-0.04}$	$1.39^{+0.35}_{-0.28}$	$1.71^{+0.10}_{-0.05}$	$1.48^{+0.07}_{-0.03}$	$0.05^{+0.02}_{-0.03}$	$0.17^{+0.20}_{-0.08}$	$1.72^{+0.42}_{-0.32}$	$1.82^{+0.24}_{-0.09}$
2	$6.64^{+0.35}_{-0.26}$	$2.27^{+0.79}_{-0.43}$	$14.15^{+6.14}_{-3.30}$	$1.52^{+1.37}_{-0.58}$	$20.95^{+5.96}_{-3.01}$	$6.64^{+0.35}_{-0.26}$	$2.27^{+0.79}_{-0.43}$	$80.78^{+34.20}_{-19.33}$	$2.16^{+1.53}_{-0.66}$	$87.64^{+34.03}_{-19.04}$
3	$0.80^{+0.01}_{-0.00}$	$0.55^{+0.03}_{-0.07}$	$0.73^{+0.04}_{-0.09}$	$0.23^{+0.03}_{-0.03}$	$1.55^{+0.04}_{-0.09}$	$0.80^{+0.01}_{-0.00}$	$0.55^{+0.03}_{-0.07}$	$0.77^{+0.04}_{-0.10}$	$0.57^{+0.07}_{-0.08}$	$1.63^{+0.04}_{-0.10}$
4	$3.79^{+0.10}_{-0.04}$	$0.05^{+0.00}_{-0.01}$	$0.07^{+0.00}_{-0.01}$	$0.51^{+0.18}_{-0.09}$	$3.91^{+0.11}_{-0.05}$	$3.79^{+0.10}_{-0.04}$	$0.05^{+0.00}_{-0.01}$	$0.07^{+0.01}_{-0.01}$	$0.69^{+0.20}_{-0.10}$	$3.93^{+0.12}_{-0.05}$
5	$2.04^{+0.02}_{-0.02}$	$0.12^{+0.02}_{-0.04}$	$0.15^{+0.04}_{-0.05}$	$0.60^{+0.15}_{-0.13}$	$2.25^{+0.06}_{-0.05}$	$2.04^{+0.02}_{-0.02}$	$0.12^{+0.02}_{-0.04}$	$0.16^{+0.10}_{-0.06}$	$0.73^{+0.18}_{-0.14}$	$2.27^{+0.10}_{-0.06}$
6	$0.99^{+0.01}_{-0.03}$	$0.20^{+0.04}_{-0.02}$	$0.16^{+0.04}_{-0.01}$	$0.48^{+0.25}_{-0.07}$	$1.20^{+0.03}_{-0.02}$	$0.99^{+0.01}_{-0.03}$	$0.20^{+0.04}_{-0.02}$	$0.20^{+0.05}_{-0.02}$	$0.77^{+0.26}_{-0.08}$	$1.27^{+0.05}_{-0.03}$
7	$1.07^{+0.63}_{-0.12}$	$0.22^{+0.19}_{-0.21}$	$0.51^{+0.90}_{-0.49}$	$2.23^{+1.81}_{-2.23}$	$1.81^{+0.87}_{-0.44}$	$1.07^{+0.64}_{-0.12}$	$0.22^{+0.19}_{-0.21}$	$1.13^{+4.63}_{-1.10}$	$2.70^{+2.42}_{-2.70}$	$2.48^{+4.63}_{-1.01}$
8	$1.17^{+0.03}_{-0.02}$	$0.11^{+0.02}_{-0.01}$	$0.15^{+0.02}_{-0.02}$	$1.43^{+0.35}_{-0.38}$	$1.46^{+0.03}_{-0.02}$	$1.17^{+0.03}_{-0.02}$	$0.11^{+0.02}_{-0.01}$	$0.16^{+0.03}_{-0.02}$	$2.22^{+0.36}_{-0.54}$	$1.55^{+0.04}_{-0.05}$
9	$1.98^{+0.03}_{-0.09}$	$2.30^{+0.41}_{-0.19}$	$2.13^{+0.56}_{-0.20}$	$0.00^{+0.00}_{-0.00}$	$4.11^{+0.54}_{-0.26}$	$1.99^{+0.04}_{-0.09}$	$5.19^{+0.80}_{-0.37}$	$9.08^{+2.34}_{-2.25}$	$0.00^{+0.00}_{-0.00}$	$11.07^{+2.33}_{-2.29}$
10	$1.91^{+0.04}_{-0.02}$	$0.47^{+0.08}_{-0.08}$	$0.61^{+0.10}_{-0.10}$	$0.94^{+0.15}_{-0.23}$	$2.61^{+0.11}_{-0.10}$	$1.93^{+0.04}_{-0.02}$	$0.47^{+0.08}_{-0.08}$	$0.65^{+0.11}_{-0.11}$	$2.18^{+0.51}_{-0.62}$	$2.80^{+0.12}_{-0.12}$
11	$1.27^{+0.03}_{-0.02}$	$0.15^{+0.04}_{-0.03}$	$0.48^{+0.21}_{-0.12}$	$0.17^{+0.02}_{-0.02}$	$1.77^{+0.20}_{-0.11}$	$1.27^{+0.03}_{-0.02}$	$0.15^{+0.04}_{-0.03}$	$1.24^{+1.02}_{-0.40}$	$0.39^{+0.04}_{-0.04}$	$2.55^{+1.01}_{-0.39}$
12	$1.47^{+0.01}_{-0.02}$	$0.10^{+0.02}_{-0.01}$	$0.12^{+0.02}_{-0.01}$	$0.29^{+0.08}_{-0.05}$	$1.62^{+0.02}_{-0.02}$	$1.48^{+0.01}_{-0.02}$	$0.10^{+0.02}_{-0.01}$	$0.13^{+0.02}_{-0.01}$	$0.59^{+0.16}_{-0.10}$	$1.67^{+0.03}_{-0.02}$
13	$1.40^{+0.02}_{-0.01}$	$0.14^{+0.02}_{-0.03}$	$0.19^{+0.03}_{-0.04}$	$0.70^{+0.12}_{-0.15}$	$1.66^{+0.04}_{-0.04}$	$1.40^{+0.02}_{-0.01}$	$0.14^{+0.02}_{-0.03}$	$0.21^{+0.03}_{-0.04}$	$1.05^{+0.16}_{-0.20}$	$1.72^{+0.05}_{-0.04}$
14	$0.85^{+0.04}_{-0.01}$	$0.08^{+0.01}_{-0.02}$	$0.11^{+0.02}_{-0.02}$	$1.42^{+0.14}_{-0.21}$	$1.11^{+0.03}_{-0.02}$	$0.85^{+0.04}_{-0.01}$	$0.08^{+0.01}_{-0.02}$	$0.12^{+0.02}_{-0.02}$	$1.70^{+0.17}_{-0.24}$	$1.14^{+0.03}_{-0.03}$
15	$1.24^{+0.02}_{-0.03}$	$0.15^{+0.01}_{-0.02}$	$0.20^{+0.02}_{-0.02}$	$0.13^{+0.06}_{-0.03}$	$1.45^{+0.02}_{-0.03}$	$1.24^{+0.02}_{-0.03}$	$0.15^{+0.01}_{-0.02}$	$0.21^{+0.02}_{-0.03}$	$0.28^{+0.11}_{-0.06}$	$1.48^{+0.02}_{-0.03}$
16	$1.39^{+0.00}_{-0.01}$	$0.53^{+0.07}_{-0.06}$	$0.70^{+0.09}_{-0.08}$	$0.55^{+0.11}_{-0.06}$	$2.14^{+0.09}_{-0.09}$	$1.39^{+0.00}_{-0.01}$	$0.53^{+0.07}_{-0.06}$	$0.75^{+0.10}_{-0.09}$	$1.14^{+0.23}_{-0.11}$	$2.25^{+0.10}_{-0.09}$
17	$1.56^{+0.03}_{-0.03}$	$0.06^{+0.01}_{-0.01}$	$0.09^{+0.02}_{-0.01}$	$1.49^{+0.35}_{-0.33}$	$1.80^{+0.03}_{-0.01}$	$1.56^{+0.03}_{-0.03}$	$0.06^{+0.01}_{-0.01}$	$0.09^{+0.02}_{-0.01}$	$1.77^{+0.42}_{-0.37}$	$1.83^{+0.03}_{-0.02}$
18	$0.71^{+0.02}_{-0.04}$	$0.64^{+0.21}_{-0.10}$	$0.84^{+0.27}_{-0.13}$	$2.57^{+0.93}_{-0.49}$	$1.81^{+0.32}_{-0.17}$	$0.71^{+0.02}_{-0.04}$	$0.64^{+0.21}_{-0.10}$	$0.90^{+0.29}_{-0.14}$	$3.60^{+1.18}_{-0.68}$	$1.97^{+0.37}_{-0.20}$
19	$1.81^{+0.05}_{-0.03}$	$0.08^{+0.01}_{-0.01}$	$0.11^{+0.01}_{-0.01}$	$0.89^{+0.51}_{-0.17}$	$2.01^{+0.04}_{-0.02}$	$1.81^{+0.05}_{-0.03}$	$0.08^{+0.01}_{-0.01}$	$0.12^{+0.01}_{-0.02}$	$1.46^{+0.54}_{-0.21}$	$2.08^{+0.05}_{-0.02}$
20	$0.96^{+0.03}_{-0.04}$	$0.06^{+0.01}_{-0.01}$	$0.08^{+0.01}_{-0.01}$	$0.74^{+0.39}_{-0.27}$	$1.12^{+0.01}_{-0.01}$	$0.96^{+0.03}_{-0.04}$	$0.06^{+0.01}_{-0.01}$	$0.09^{+0.01}_{-0.01}$	$0.98^{+0.39}_{-0.23}$	$1.15^{+0.03}_{-0.01}$
21	$0.88^{+0.02}_{-0.01}$	$0.06^{+0.01}_{-0.01}$	$0.08^{+0.02}_{-0.01}$	$0.22^{+0.03}_{-0.02}$	$0.99^{+0.02}_{-0.01}$	$0.88^{+0.02}_{-0.01}$	$0.06^{+0.01}_{-0.01}$	$0.09^{+0.02}_{-0.01}$	$0.52^{+0.07}_{-0.05}$	$1.03^{+0.03}_{-0.01}$
22	$1.11^{+0.02}_{-0.01}$	$0.15^{+0.03}_{-0.02}$	$0.12^{+0.03}_{-0.01}$	$0.22^{+0.05}_{-0.04}$	$1.25^{+0.03}_{-0.01}$	$1.11^{+0.02}_{-0.01}$	$0.15^{+0.03}_{-0.02}$	$0.13^{+0.04}_{-0.02}$	$0.44^{+0.09}_{-0.07}$	$1.29^{+0.04}_{-0.02}$
23	$2.74^{+0.04}_{-0.04}$	$0.10^{+0.03}_{-0.02}$	$0.13^{+0.04}_{-0.03}$	$0.38^{+0.08}_{-0.04}$	$2.91^{+0.04}_{-0.04}$	$2.75^{+0.04}_{-0.04}$	$0.10^{+0.03}_{-0.02}$	$0.14^{+0.05}_{-0.03}$	$0.93^{+0.19}_{-0.11}$	$2.98^{+0.06}_{-0.04}$
24	$2.10^{+0.01}_{-0.02}$	$0.04^{+0.01}_{-0.01}$	$0.05^{+0.01}_{-0.02}$	$0.93^{+0.12}_{-0.15}$	$2.25^{+0.01}_{-0.03}$	$2.11^{+0.01}_{-0.02}$	$0.04^{+0.01}_{-0.01}$	$0.06^{+0.01}_{-0.02}$	$1.12^{+0.15}_{-0.16}$	$2.28^{+0.01}_{-0.04}$
25	$0.77^{+0.04}_{-0.05}$	$0.17^{+0.04}_{-0.07}$	$0.24^{+0.05}_{-0.12}$	$1.58^{+0.45}_{-0.52}$	$1.17^{+0.05}_{-0.13}$	$0.77^{+0.04}_{-0.05}$	$0.17^{+0.04}_{-0.07}$	$0.28^{+0.06}_{-0.14}$	$2.28^{+0.56}_{-0.73}$	$1.29^{+0.08}_{-0.16}$
26	$2.23^{+0.04}_{-0.02}$	$0.12^{+0.02}_{-0.02}$	$0.16^{+0.02}_{-0.03}$	$0.52^{+0.12}_{-0.09}$	$2.44^{+0.06}_{-0.03}$	$2.23^{+0.04}_{-0.02}$	$0.12^{+0.02}_{-0.02}$	$0.17^{+0.03}_{-0.03}$	$1.20^{+0.39}_{-0.23}$	$2.52^{+0.08}_{-0.04}$
27	$1.64^{+0.09}_{-0.14}$	$0.02^{+0.01}_{-0.00}$	$0.02^{+0.01}_{-0.00}$	$2.01^{+0.69}_{-0.87}$	$1.86^{+0.15}_{-0.19}$	$1.64^{+0.09}_{-0.14}$	$0.02^{+0.01}_{-0.00}$	$0.02^{+0.02}_{-0.00}$	$2.40^{+0.82}_{-1.04}$	$1.91^{+0.16}_{-0.21}$
28	$2.97^{+0.02}_{-0.01}$	$0.30^{+0.03}_{-0.03}$	$0.66^{+0.08}_{-0.06}$	$1.37^{+0.13}_{-0.30}$	$3.77^{+0.08}_{-0.07}$	$2.97^{+0.02}_{-0.01}$	$0.30^{+0.03}_{-0.03}$	$1.20^{+0.17}_{-0.11}$	$1.88^{+0.17}_{-0.37}$	$4.35^{+0.17}_{-0.12}$
29	$1.45^{+0.01}_{-0.00}$	$0.06^{+0.01}_{-0.01}$	$0.07^{+0.02}_{-0.01}$	$0.30^{+0.06}_{-0.12}$	$1.55^{+0.02}_{-0.02}$	$1.45^{+0.01}_{-0.00}$	$0.06^{+0.01}_{-0.01}$	$0.08^{+0.02}_{-0.01}$	$0.50^{+0.07}_{-0.14}$	$1.58^{+0.02}_{-0.02}$
30	$0.66^{+0.01}_{-0.02}$	$0.01^{+0.00}_{-0.00}$	$0.02^{+0.00}_{-0.00}$	$0.53^{+0.12}_{-0.09}$	$0.74^{+0.01}_{-0.02}$	$0.66^{+0.01}_{-0.02}$	$0.01^{+0.00}_{-0.00}$	$0.04^{+0.01}_{-0.01}$	$0.97^{+0.16}_{-0.13}$	$0.80^{+0.02}_{-0.03}$
31	$0.87^{+0.00}_{-0.00}$	$0.08^{+0.01}_{-0.01}$	$0.11^{+0.01}_{-0.01}$	$0.36^{+0.04}_{-0.03}$	$1.01^{+0.02}_{-0.01}$	$0.87^{+0.00}_{-0.00}$	$0.08^{+0.01}_{-0.01}$	$0.11^{+0.02}_{-0.01}$	$0.85^{+0.10}_{-0.08}$	$1.07^{+0.02}_{-0.02}$
32	$0.71^{+0.01}_{-0.02}$	$0.11^{+0.02}_{-0.01}$	$0.14^{+0.03}_{-0.02}$	$0.99^{+0.25}_{-0.22}$	$0.95^{+0.03}_{-0.04}$	$0.71^{+0.01}_{-0.02}$	$0.11^{+0.02}_{-0.01}$	$0.15^{+0.03}_{-0.02}$	$1.44^{+0.26}_{-0.20}$	$1.01^{+0.04}_{-0.04}$
33	$1.13^{+0.04}_{-0.04}$	$0.09^{+0.02}_{-0.03}$	$0.12^{+0.02}_{-0.03}$	$0.13^{+0.06}_{-0.04}$	$1.26^{+0.03}_{-0.05}$	$1.13^{+0.04}_{-0.04}$	$0.09^{+0.02}_{-0.03}$	$0.12^{+0.02}_{-0.04}$	$0.28^{+0.09}_{-0.08}$	$1.28^{+0.03}_{-0.05}$
34	$1.43^{+0.05}_{-0.08}$	$0.10^{+0.02}_{-0.03}$	$0.14^{+0.03}_{-0.05}$	$2.28^{+0.44}_{-0.83}$	$1.80^{+0.05}_{-0.11}$	$1.43^{+0.05}_{-0.08}$	$0.10^{+0.02}_{-0.03}$	$0.15^{+0.04}_{-0.05}$	$3.01^{+0.40}_{-1.20}$	$1.88^{+0.04}_{-0.15}$
35	$1.19^{+0.01}_{-0.01}$	$0.06^{+0.01}_{-0.01}$	$0.08^{+0.01}_{-0.01}$	$0.41^{+0.24}_{-0.05}$	$1.31^{+0.02}_{-0.01}$	$1.19^{+0.01}_{-0.01}$	$0.06^{+0.01}_{-0.01}$	$0.08^{+0.01}_{-0.01}$	$0.77^{+0.26}_{-0.05}$	$1.35^{+0.02}_{-0.01}$
36	$0.71^{+0.02}_{-0.08}$	$0.03^{+0.03}_{-0.00}$	$0.03^{+0.16}_{-0.00}$	$0.99^{+0.45}_{-0.25}$	$0.84^{+0.07}_{-0.02}$	$0.71^{+0.02}_{-0.09}$	$0.03^{+0.03}_{-0.00}$	$0.04^{+0.68}_{-0.01}$	$1.27^{+0.51}_{-0.31}$	$0.88^{+0.57}_{-0.03}$
37	$2.43^{+0.03}_{-0.12}$	$0.72^{+0.13}_{-0.10}$	$0.68^{+0.12}_{-0.08}$	$1.01^{+0.12}_{-0.15}$	$3.20^{+0.11}_{-0.11}$	$2.43^{+0.03}_{-0.12}$	$0.72^{+0.13}_{-0.10}$	$0.79^{+0.14}_{-0.11}$	$2.20^{+0.30}_{-0.34}$	$3.45^{+0.13}_{-0.15}$
38	$1.27^{+0.02}_{-0.06}$	$0.09^{+0.04}_{-0.01}$	$0.12^{+0.13}_{-0.01}$	$0.39^{+0.16}_{-0.06}$	$1.43^{+0.08}_{-0.03}$	$1.27^{+0.02}_{-0.06}$	$0.09^{+0.04}_{-0.01}$	$0.13^{+0.28}_{-0.02}$	$0.76^{+0.16}_{-0.09}$	$1.48^{+0.24}_{-0.03}$
39	$0.21^{+0.01}_{-0.02}$	$0.56^{+0.07}_{-0.07}$	$0.70^{+0.09}_{-0.09}$	$0.43^{+0.15}_{-0.07}$	$0.95^{+0.09}_{-0.08}$	$0.21^{+0.01}_{-0.02}$	$0.56^{+0.07}_{-0.07}$	$1.60^{+0.19}_{-0.23}$	$0.90^{+0.30}_{-0.20}$	$1.90^{+0.19}_{-0.21}$
40	$1.08^{+0.01}_{-0.00}$	$0.01^{+0.00}_{-0.00}$	$0.03^{+0.01}_{-0.00}$	$0.21^{+0.03}_{-0.01}$	$1.13^{+0.01}_{-0.00}$	$1.08^{+0.01}_{-0.00}$	$0.01^{+0.00}_{-0.00}$	$0.04^{+0.03}_{-0.00}$	$0.42^{+0.06}_{-0.03}$	$1.17^{+0.03}_{-0.00}$
41	$0.43^{+0.01}_{-0.01}$	$0.02^{+0.00}_{-0.00}$	$0.02^{+0.00}_{-0.00}$	$0.96^{+0.14}_{-0.13}$	$0.55^{+0.01}_{-0.01}$	$0.43^{+0.01}_{-0.01}$	$0.02^{+0.00}_{-0.00}$	$0.02^{+0.00}_{-0.00}$	$1.30^{+0.15}_{-0.16}$	$0.59^{+0.01}_{-0.01}$
42	$2.75^{+0.05}_{-0.03}$	$0.71^{+0.08}_{-0.11}$	$0.62^{+0.07}_{-0.09}$	$1.47^{+0.36}_{-0.62}$	$3.52^{+0.07}_{-0.12}$	$2.75^{+0.05}_{-0.03}$	$1.69^{+0.21}_{-0.22}$	$2.16^{+0.52}_{-0.26}$	$2.19^{+0.31}_{-0.79}$	$5.13^{+0.52}_{-0.27}$

Table B4. Infrared and bolometric luminosities from the Siebenmorgen15 model fits.

ID	Infrared luminosities					Bolometric luminosities				
	$L_{\rm Sb}$	$L^{\rm o}_{\rm AGN}$ 10^{12} L$_\odot$	$L^{\rm c}_{\rm AGN}$	$L_{\rm host}$ 10^{11} L$_\odot$	$L^{\rm c}_{\rm Tot}$ 10^{12} L$_\odot$	$L_{\rm Sb}$	$L^{\rm o}_{\rm AGN}$ 10^{12} L$_\odot$	$L^{\rm c}_{\rm AGN}$	$L_{\rm host}$ 10^{11} L$_\odot$	$L^{\rm c}_{\rm Tot}$ 10^{12} L$_\odot$
1	$1.72^{+0.07}_{-0.06}$	$0.27^{+0.10}_{-0.09}$	$0.21^{+0.07}_{-0.06}$	$0.74^{+0.33}_{-0.29}$	$2.00^{+0.10}_{-0.07}$	$1.72^{+0.07}_{-0.06}$	$0.27^{+0.10}_{-0.09}$	$0.21^{+0.07}_{-0.06}$	$1.04^{+0.39}_{-0.31}$	$2.03^{+0.11}_{-0.07}$
2	$10.01^{+0.22}_{-0.13}$	$0.62^{+0.07}_{-0.13}$	$0.53^{+0.06}_{-0.12}$	$0.55^{+0.66}_{-0.21}$	$10.60^{+0.16}_{-0.14}$	$10.01^{+0.22}_{-0.13}$	$0.65^{+0.07}_{-0.12}$	$0.81^{+0.08}_{-0.19}$	$0.99^{+0.64}_{-0.36}$	$10.92^{+0.14}_{-0.17}$
3	$1.07^{+0.06}_{-0.04}$	$0.71^{+0.09}_{-0.09}$	$0.91^{+0.12}_{-0.13}$	$0.03^{+0.03}_{-0.03}$	$1.99^{+0.09}_{-0.11}$	$1.07^{+0.06}_{-0.04}$	$0.76^{+0.10}_{-0.09}$	$1.12^{+0.15}_{-0.14}$	$0.08^{+0.08}_{-0.07}$	$2.20^{+0.11}_{-0.13}$
4	$2.72^{+0.19}_{-0.11}$	$1.35^{+0.13}_{-0.25}$	$1.29^{+0.12}_{-0.29}$	$0.00^{+0.00}_{-0.00}$	$4.01^{+0.06}_{-0.17}$	$2.73^{+0.18}_{-0.11}$	$1.35^{+0.13}_{-0.25}$	$1.29^{+0.12}_{-0.29}$	$0.00^{+0.00}_{-0.00}$	$4.02^{+0.06}_{-0.18}$
5	$2.02^{+0.02}_{-0.03}$	$0.40^{+0.05}_{-0.04}$	$0.50^{+0.06}_{-0.05}$	$0.15^{+0.02}_{-0.02}$	$2.53^{+0.04}_{-0.04}$	$2.02^{+0.02}_{-0.03}$	$0.40^{+0.05}_{-0.04}$	$0.51^{+0.06}_{-0.05}$	$0.26^{+0.02}_{-0.03}$	$2.56^{+0.04}_{-0.04}$
6	$0.80^{+0.17}_{-0.04}$	$0.61^{+0.06}_{-0.20}$	$0.43^{+0.05}_{-0.14}$	$0.31^{+0.05}_{-0.04}$	$1.26^{+0.08}_{-0.03}$	$0.80^{+0.17}_{-0.04}$	$0.61^{+0.06}_{-0.20}$	$0.43^{+0.05}_{-0.14}$	$0.60^{+0.07}_{-0.09}$	$1.29^{+0.08}_{-0.03}$
7	$1.46^{+0.04}_{-0.03}$	$0.05^{+0.01}_{-0.01}$	$0.04^{+0.00}_{-0.01}$	$0.16^{+0.13}_{-0.13}$	$1.52^{+0.02}_{-0.01}$	$1.46^{+0.04}_{-0.03}$	$0.11^{+0.07}_{-0.03}$	$0.13^{+0.04}_{-0.03}$	$0.22^{+0.18}_{-0.18}$	$1.61^{+0.06}_{-0.03}$
8	$1.05^{+0.03}_{-0.02}$	$0.22^{+0.03}_{-0.03}$	$0.21^{+0.03}_{-0.04}$	$2.02^{+0.23}_{-0.30}$	$1.46^{+0.03}_{-0.04}$	$1.05^{+0.03}_{-0.02}$	$0.22^{+0.03}_{-0.03}$	$0.21^{+0.03}_{-0.04}$	$2.68^{+0.32}_{-0.44}$	$1.53^{+0.04}_{-0.06}$
9	$0.40^{+0.42}_{-0.16}$	$3.14^{+0.77}_{-0.37}$	$2.71^{+0.66}_{-0.33}$	$9.10^{+1.64}_{-4.71}$	$4.03^{+0.64}_{-0.36}$	$0.40^{+0.42}_{-0.16}$	$3.31^{+0.82}_{-0.39}$	$4.14^{+1.01}_{-0.52}$	$12.92^{+2.25}_{-6.79}$	$5.83^{+0.92}_{-0.72}$
10	$2.24^{+0.08}_{-0.08}$	$0.53^{+0.03}_{-0.14}$	$0.75^{+0.07}_{-0.28}$	$0.84^{+0.29}_{-0.24}$	$3.08^{+0.06}_{-0.24}$	$2.26^{+0.08}_{-0.09}$	$0.54^{+0.03}_{-0.13}$	$1.00^{+0.14}_{-0.40}$	$1.80^{+0.72}_{-0.61}$	$3.44^{+0.13}_{-0.37}$
11	$1.23^{+0.07}_{-0.07}$	$0.30^{+0.09}_{-0.07}$	$0.25^{+0.07}_{-0.07}$	$0.18^{+0.01}_{-0.02}$	$1.50^{+0.02}_{-0.02}$	$1.23^{+0.07}_{-0.07}$	$0.30^{+0.09}_{-0.07}$	$0.25^{+0.07}_{-0.07}$	$0.41^{+0.03}_{-0.03}$	$1.53^{+0.02}_{-0.02}$
12	$1.55^{+0.08}_{-0.01}$	$0.06^{+0.01}_{-0.04}$	$0.04^{+0.00}_{-0.02}$	$0.03^{+0.05}_{-0.03}$	$1.59^{+0.07}_{-0.01}$	$1.56^{+0.08}_{-0.01}$	$0.07^{+0.01}_{-0.04}$	$0.04^{+0.01}_{-0.02}$	$0.05^{+0.09}_{-0.05}$	$1.60^{+0.07}_{-0.01}$
13	$1.22^{+0.08}_{-0.05}$	$0.49^{+0.07}_{-0.11}$	$0.44^{+0.07}_{-0.11}$	$0.62^{+0.50}_{-0.15}$	$1.72^{+0.05}_{-0.06}$	$1.22^{+0.08}_{-0.05}$	$0.49^{+0.07}_{-0.11}$	$0.44^{+0.07}_{-0.11}$	$0.97^{+0.55}_{-0.20}$	$1.76^{+0.06}_{-0.06}$
14	$0.75^{+0.05}_{-0.02}$	$0.11^{+0.05}_{-0.02}$	$0.40^{+0.31}_{-0.07}$	$0.74^{+0.31}_{-0.25}$	$1.23^{+0.34}_{-0.09}$	$0.76^{+0.05}_{-0.02}$	$0.11^{+0.05}_{-0.02}$	$0.72^{+0.50}_{-0.12}$	$0.99^{+0.38}_{-0.29}$	$1.58^{+0.54}_{-0.14}$
15	$1.20^{+0.12}_{-0.02}$	$0.39^{+0.05}_{-0.39}$	$0.48^{+0.07}_{-0.48}$	$0.16^{+0.05}_{-0.02}$	$1.70^{+0.07}_{-0.37}$	$1.20^{+0.12}_{-0.02}$	$0.39^{+0.05}_{-0.39}$	$0.49^{+0.07}_{-0.48}$	$0.35^{+0.10}_{-0.05}$	$1.72^{+0.07}_{-0.37}$
16	$1.10^{+0.10}_{-0.11}$	$1.10^{+0.14}_{-0.17}$	$0.88^{+0.11}_{-0.13}$	$0.54^{+0.09}_{-0.07}$	$2.03^{+0.02}_{-0.07}$	$1.10^{+0.10}_{-0.11}$	$1.10^{+0.14}_{-0.17}$	$0.88^{+0.11}_{-0.13}$	$1.02^{+0.17}_{-0.14}$	$2.08^{+0.05}_{-0.07}$
17	$1.50^{+0.03}_{-0.03}$	$0.16^{+0.04}_{-0.03}$	$0.14^{+0.03}_{-0.02}$	$1.38^{+0.23}_{-0.24}$	$1.78^{+0.04}_{-0.02}$	$1.50^{+0.04}_{-0.03}$	$0.16^{+0.04}_{-0.03}$	$0.14^{+0.03}_{-0.02}$	$1.78^{+0.30}_{-0.28}$	$1.82^{+0.04}_{-0.03}$
18	$0.62^{+0.09}_{-0.12}$	$1.20^{+0.38}_{-0.18}$	$0.98^{+0.33}_{-0.13}$	$2.47^{+0.92}_{-0.35}$	$1.84^{+0.35}_{-0.08}$	$0.62^{+0.09}_{-0.12}$	$1.20^{+0.38}_{-0.18}$	$1.07^{+0.38}_{-0.14}$	$3.40^{+1.23}_{-0.47}$	$2.03^{+0.43}_{-0.11}$
19	$1.59^{+0.04}_{-0.02}$	$0.23^{+0.04}_{-0.04}$	$0.26^{+0.05}_{-0.05}$	$1.57^{+0.23}_{-0.34}$	$2.01^{+0.05}_{-0.05}$	$1.60^{+0.04}_{-0.02}$	$0.23^{+0.04}_{-0.04}$	$0.26^{+0.05}_{-0.05}$	$2.14^{+0.29}_{-0.40}$	$2.07^{+0.06}_{-0.05}$
20	$0.92^{+0.02}_{-0.01}$	$0.17^{+0.03}_{-0.03}$	$0.40^{+0.10}_{-0.08}$	$0.54^{+0.10}_{-0.18}$	$1.38^{+0.08}_{-0.07}$	$0.92^{+0.02}_{-0.01}$	$0.17^{+0.03}_{-0.03}$	$0.45^{+0.12}_{-0.09}$	$0.81^{+0.16}_{-0.23}$	$1.45^{+0.10}_{-0.08}$
21	$0.80^{+0.03}_{-0.03}$	$0.32^{+0.04}_{-0.04}$	$0.41^{+0.04}_{-0.05}$	$0.47^{+0.07}_{-0.15}$	$1.26^{+0.03}_{-0.04}$	$0.80^{+0.03}_{-0.03}$	$0.32^{+0.04}_{-0.04}$	$0.41^{+0.04}_{-0.05}$	$0.78^{+0.08}_{-0.15}$	$1.29^{+0.03}_{-0.04}$
22	$1.03^{+0.05}_{-0.05}$	$0.45^{+0.06}_{-0.04}$	$0.39^{+0.05}_{-0.04}$	$0.23^{+0.05}_{-0.04}$	$1.44^{+0.07}_{-0.05}$	$1.03^{+0.05}_{-0.05}$	$0.47^{+0.06}_{-0.04}$	$0.43^{+0.06}_{-0.05}$	$0.51^{+0.13}_{-0.09}$	$1.51^{+0.08}_{-0.06}$
23	$2.86^{+0.05}_{-0.04}$	$0.06^{+0.02}_{-0.02}$	$0.07^{+0.02}_{-0.02}$	$0.00^{+0.00}_{-0.00}$	$2.93^{+0.05}_{-0.04}$	$2.86^{+0.05}_{-0.04}$	$0.14^{+0.02}_{-0.03}$	$0.18^{+0.02}_{-0.04}$	$0.00^{+0.00}_{-0.00}$	$3.04^{+0.04}_{-0.05}$
24	$2.25^{+0.05}_{-0.02}$	$0.08^{+0.02}_{-0.03}$	$0.06^{+0.01}_{-0.02}$	$0.45^{+0.13}_{-0.13}$	$2.36^{+0.04}_{-0.01}$	$2.25^{+0.05}_{-0.02}$	$0.08^{+0.02}_{-0.03}$	$0.06^{+0.01}_{-0.02}$	$0.61^{+0.16}_{-0.14}$	$2.38^{+0.04}_{-0.01}$
25	$0.80^{+0.02}_{-0.05}$	$0.23^{+0.06}_{-0.03}$	$0.35^{+0.12}_{-0.05}$	$1.72^{+0.25}_{-0.26}$	$1.32^{+0.10}_{-0.05}$	$0.80^{+0.02}_{-0.05}$	$0.23^{+0.06}_{-0.03}$	$0.38^{+0.19}_{-0.05}$	$2.49^{+0.39}_{-0.42}$	$1.43^{+0.17}_{-0.08}$
26	$2.05^{+0.12}_{-0.08}$	$0.27^{+0.07}_{-0.07}$	$0.23^{+0.13}_{-0.05}$	$1.65^{+0.84}_{-0.71}$	$2.45^{+0.13}_{-0.04}$	$2.05^{+0.12}_{-0.08}$	$0.27^{+0.07}_{-0.07}$	$0.23^{+0.13}_{-0.05}$	$2.30^{+0.93}_{-0.73}$	$2.52^{+0.14}_{-0.03}$
27	$2.21^{+0.03}_{-0.06}$	$0.02^{+0.03}_{-0.01}$	$0.01^{+0.02}_{-0.01}$	$1.32^{+0.38}_{-1.08}$	$2.36^{+0.06}_{-0.16}$	$2.22^{+0.03}_{-0.07}$	$0.02^{+0.02}_{-0.01}$	$0.02^{+0.03}_{-0.01}$	$1.70^{+0.48}_{-1.18}$	$2.41^{+0.07}_{-0.16}$
28	$2.89^{+0.07}_{-0.05}$	$0.47^{+0.09}_{-0.10}$	$0.60^{+0.11}_{-0.13}$	$0.42^{+0.07}_{-0.05}$	$3.53^{+0.11}_{-0.08}$	$2.89^{+0.07}_{-0.05}$	$0.47^{+0.09}_{-0.10}$	$0.63^{+0.11}_{-0.13}$	$0.91^{+0.15}_{-0.11}$	$3.61^{+0.11}_{-0.09}$
29	$1.45^{+0.00}_{-0.01}$	$0.07^{+0.02}_{-0.01}$	$0.08^{+0.02}_{-0.01}$	$0.41^{+0.13}_{-0.04}$	$1.57^{+0.02}_{-0.01}$	$1.45^{+0.00}_{-0.01}$	$0.07^{+0.02}_{-0.01}$	$0.08^{+0.02}_{-0.01}$	$0.61^{+0.13}_{-0.05}$	$1.59^{+0.02}_{-0.01}$
30	$0.68^{+0.03}_{-0.03}$	$0.29^{+0.05}_{-0.05}$	$0.27^{+0.05}_{-0.04}$	$0.86^{+0.16}_{-0.13}$	$1.04^{+0.04}_{-0.03}$	$0.68^{+0.03}_{-0.03}$	$0.29^{+0.05}_{-0.05}$	$0.27^{+0.05}_{-0.04}$	$1.36^{+0.19}_{-0.17}$	$1.09^{+0.05}_{-0.04}$
31	$0.32^{+0.07}_{-0.04}$	$0.96^{+0.03}_{-0.05}$	$1.24^{+0.15}_{-0.05}$	$0.76^{+0.30}_{-0.22}$	$1.64^{+0.15}_{-0.02}$	$0.33^{+0.07}_{-0.04}$	$0.96^{+0.03}_{-0.05}$	$1.24^{+0.15}_{-0.05}$	$1.22^{+0.34}_{-0.24}$	$1.69^{+0.16}_{-0.02}$
32	$0.56^{+0.05}_{-0.02}$	$0.19^{+0.04}_{-0.04}$	$0.18^{+0.04}_{-0.05}$	$0.90^{+0.16}_{-0.34}$	$0.83^{+0.03}_{-0.03}$	$0.56^{+0.05}_{-0.02}$	$0.19^{+0.04}_{-0.04}$	$0.18^{+0.04}_{-0.05}$	$1.43^{+0.14}_{-0.30}$	$0.89^{+0.03}_{-0.03}$
33	$1.29^{+0.02}_{-0.02}$	$0.29^{+0.03}_{-0.06}$	$0.36^{+0.03}_{-0.08}$	$0.27^{+0.05}_{-0.05}$	$1.68^{+0.02}_{-0.07}$	$1.29^{+0.02}_{-0.02}$	$0.29^{+0.03}_{-0.06}$	$0.36^{+0.03}_{-0.08}$	$0.57^{+0.11}_{-0.10}$	$1.71^{+0.02}_{-0.07}$
34	$1.21^{+0.12}_{-0.08}$	$0.56^{+0.08}_{-0.14}$	$1.38^{+0.20}_{-0.31}$	$3.13^{+0.60}_{-0.82}$	$2.90^{+0.18}_{-0.25}$	$1.21^{+0.12}_{-0.08}$	$0.56^{+0.08}_{-0.14}$	$1.50^{+0.25}_{-0.35}$	$4.11^{+0.71}_{-1.01}$	$3.12^{+0.23}_{-0.30}$
35	$1.05^{+0.05}_{-0.04}$	$0.45^{+0.07}_{-0.06}$	$0.97^{+0.16}_{-0.20}$	$0.38^{+0.07}_{-0.05}$	$2.06^{+0.13}_{-0.17}$	$1.06^{+0.05}_{-0.04}$	$0.45^{+0.07}_{-0.06}$	$1.03^{+0.18}_{-0.22}$	$0.74^{+0.11}_{-0.08}$	$2.16^{+0.15}_{-0.19}$
36	$0.67^{+0.01}_{-0.01}$	$0.00^{+0.00}_{-0.00}$	$0.00^{+0.00}_{-0.00}$	$0.75^{+0.09}_{-0.12}$	$0.74^{+0.01}_{-0.02}$	$0.67^{+0.01}_{-0.01}$	$0.00^{+0.00}_{-0.00}$	$0.01^{+0.00}_{-0.00}$	$1.00^{+0.12}_{-0.16}$	$0.78^{+0.01}_{-0.02}$
37	$2.17^{+0.08}_{-0.09}$	$1.46^{+0.16}_{-0.21}$	$2.17^{+0.20}_{-0.35}$	$1.03^{+0.20}_{-0.10}$	$4.45^{+0.18}_{-0.28}$	$2.17^{+0.08}_{-0.09}$	$1.49^{+0.15}_{-0.22}$	$3.31^{+0.23}_{-0.55}$	$2.42^{+0.59}_{-0.19}$	$5.73^{+0.26}_{-0.49}$
38	$1.01^{+0.03}_{-0.03}$	$0.17^{+0.09}_{-0.03}$	$0.38^{+0.20}_{-0.16}$	$0.34^{+0.12}_{-0.03}$	$1.42^{+0.19}_{-0.14}$	$1.01^{+0.03}_{-0.03}$	$0.17^{+0.09}_{-0.03}$	$0.42^{+0.31}_{-0.19}$	$0.69^{+0.15}_{-0.06}$	$1.50^{+0.31}_{-0.17}$
39	$0.00^{+0.01}_{-0.00}$	$0.76^{+0.04}_{-0.04}$	$1.09^{+0.05}_{-0.05}$	$0.73^{+0.18}_{-0.19}$	$1.16^{+0.03}_{-0.04}$	$0.00^{+0.01}_{-0.00}$	$0.77^{+0.05}_{-0.04}$	$1.88^{+0.08}_{-0.09}$	$1.15^{+0.26}_{-0.23}$	$1.99^{+0.08}_{-0.08}$
40	$0.59^{+0.11}_{-0.01}$	$0.45^{+0.02}_{-0.13}$	$0.53^{+0.02}_{-0.12}$	$0.60^{+0.07}_{-0.10}$	$1.18^{+0.04}_{-0.04}$	$0.59^{+0.11}_{-0.01}$	$0.45^{+0.02}_{-0.13}$	$0.53^{+0.02}_{-0.12}$	$0.80^{+0.10}_{-0.11}$	$1.20^{+0.04}_{-0.04}$
41	$0.44^{+0.04}_{-0.03}$	$0.12^{+0.03}_{-0.02}$	$0.16^{+0.05}_{-0.03}$	$1.07^{+0.37}_{-0.49}$	$0.70^{+0.05}_{-0.03}$	$0.44^{+0.04}_{-0.03}$	$0.12^{+0.03}_{-0.02}$	$0.16^{+0.05}_{-0.03}$	$1.45^{+0.41}_{-0.52}$	$0.74^{+0.05}_{-0.04}$
42	$2.42^{+0.08}_{-0.22}$	$1.67^{+0.17}_{-0.20}$	$1.35^{+0.14}_{-0.15}$	$2.78^{+0.88}_{-0.43}$	$4.05^{+0.15}_{-0.23}$	$2.42^{+0.08}_{-0.22}$	$2.03^{+0.19}_{-0.28}$	$1.36^{+0.15}_{-0.17}$	$6.96^{+1.43}_{-1.16}$	$4.48^{+0.20}_{-0.29}$

This paper has been typeset from a TEX/LATEX file prepared by the author.